

**INFLUENCE OF METAL (Ni) AND METAL OXIDE (IRON OXIDE)
NANOPARTICLES ON THE ELECTROCHEMICAL
CAPACITANCE OF rGO-MnO_x NANOCOMPOSITE**

by

MD. AKTER HOSSAIN REAZ

**A THESIS SUBMITTED IN PARTIAL FULFILLMENT OF THE
REQUIREMENT FOR THE DEGREE**

OF

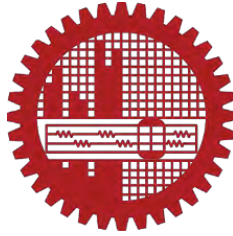
MASTER OF SCIENCE IN CHEMISTRY



Department of Chemistry

**BANGLADESH UNIVERSITY OF ENGINEERING AND TECHNOLOGY
(BUET), DHAKA-1000**

January 2020



CANDIDATE'S DECLARATION

It is hereby declared that this thesis or any part of it has not been submitted elsewhere for the award of any degree or diploma.

A small rectangular box containing a handwritten signature in black ink that reads "Akter H. Reaz".

.....
(Md. Akter Hossain Reaz)

Signature of the Candidate

Bangladesh University of Engineering and Technology (BUET), Dhaka-1000
Department of Chemistry



Certification of Thesis

A thesis on

**INFLUENCE OF METAL (Ni) AND METAL OXIDE (IRON OXIDE)
NANOPARTICLES ON THE ELECTROCHEMICAL CAPACITANCE OF rGO-
MnO_x NANOCOMPOSITE**

by

Md. Akter Hossain Reaz

Roll No.: 1017032708, Session: October-2017, has been accepted as satisfactory in partial fulfillment of the requirements for the degree of Master of Science (M.Sc.) in Chemistry and certify that the student has demonstrated a satisfactory knowledge of the field covered by this thesis in an oral examination held on January 18, 2020.


Board of Examiners

1. Dr. Md. Shakhawat Hossain Firoz
Professor
Department of Chemistry
BUET, Dhaka-1000.


19-01-2020

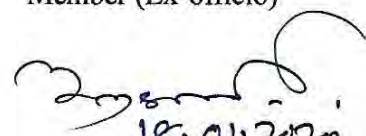
Supervisor & Chairman

2. Dr. Md. Shakhawat Hossain Firoz
Head
Department of Chemistry
BUET, Dhaka-1000


18-01-2020

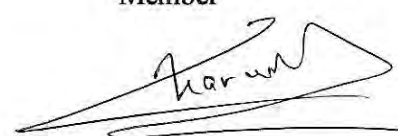
Member (Ex-officio)

3. Dr. Al-Nakib Chowdhury
Professor
Department of Chemistry
BUET, Dhaka-1000


18.01.2020


Member

4. Dr. Chanchal Kumar Roy
Assistant Professor
Department of Chemistry
BUET, Dhaka-1000



Member

5. Dr. Md. Mominul Islam
Associate Professor
Department of Chemistry
University of Dhaka, Dhaka -1000



Member (External)

DEDICATED TO

MY FAMILY MEMBERS

AND

REVERENT TEACHERS

Acknowledgement

At first, I would like to praise the name of the Almighty Allah, for giving me physical and mental ability, patience and courage from the starting of this program till now to carry out the research work presented in this dissertation.

I would like to express my earnest gratitude and sincere appreciation to my honorable supervisor, **Dr. Md. Shakhawat Hossain Firoz**, Professor & head, Department of Chemistry, BUET, for his kind supervision, indispensable guidance, enlightened suggestions and relentless inspiration through the whole research period. I am greatly in debt to him for giving me the opportunity to work on the interesting field of graphene-based charge storage materials along with availing the scope of working with different research groups and hence I feel myself enormously lucky to be a member of his **nanoChem** research group.

I am also momentarily gratified to **Dr. Chanchal Kumar Roy**, Assistant Professor, Department of Chemistry, BUET, for suggesting informative course materials and introducing me to the exciting field of electrochemistry and offering me the chance to work with his group at Advanced Research Laboratory, Department of Chemistry, BUET. I am truly grateful to him for his kind facilitation of the electrochemical characterization of the synthesized materials, patient guidance in the relevant studies and best advices during the analysis of the results.

I would like to convey my deepest gratitude to all teachers including Dr. **Al-Nakib Chowdhury**, **Dr. Ayesha Sharmin**, **Dr. Abu Bin Imran** and **Dr. Md. Shafiul Azam**, **Dr. Md. Abdul Goni**, Department of Chemistry, BUET, for their valuable suggestions and guidance during the course and research period

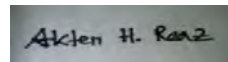
I owe a heartfelt gratitude to **Mohammad Mozammel Hosen**, Scientific Officer, Chemistry Division. Atomic Energy Commission, for his directions during my research work and **Md. Abu Bakar Siddique**, Scientific officer, Bangladesh Commission of Scientific and Industrial Research (BCSIR), for his crucial support and directions during my research work.

An immense thanks belongs to every member of our research group (nanoChem) at nanoChemistry Research Laboratory, BUET, for their supports and patronages during my whole work. I am also gratified to all members of **Advanced Research Group**, Department of Chemistry, BUET, for their succor during the electrochemical measurement of synthesized of the materials. I am also highly grateful to all members of his group at Materials chemistry Research Laboratory, University of Dhaka, for the amicable environment they provided during some of my electrochemical measurements.

I would be indebted a heartfelt gratitude to Department of Glass and Ceramics, BUET, for their continuous support in the XRD and FESEM analysis of the synthesized samples I thank CASR, BUET for funding this project.

Finally, I would like to express my sincerest thanks to my family members for their continuous inspirations, moral supports and immeasurable sacrifices during this project.

January 18, 2020



.....
(Md. Akter Hossain Reaz)

Abstract

Electrochemical capacitors- known as supercapacitors- have attracted phenomenal attention in energy sector as sustainable and affordable energy storage systems for their advantageous characteristics over batteries and conventional capacitors. Herein, we have demonstrated a chemical route for the modification of rGO-MnO₂ by Ni and Fe₃O₄ nanoparticles for the synthesis of porous and hollow crumpled (--)@rGO-MnO₂, core-shell Ni@rGO-MnO₂, core-shell Fe₃O₄@rGO-MnO₂ nanocomposite with a very high electrochemical capacitance as compared to MnO₂ on flat reduced graphene sheet (rGO-MnO₂). Core-shell Ni@rGO-MnO₂, Fe₃O₄@rGO-MnO₂ nanocomposites were successfully synthesized through the *in-situ* chemical redox reaction between KMnO₄ and benzyl alcohol on Ni@rGO and Fe₃O₄@rGO, respectively. Porous and hollow crumpled (--)@rGO-MnO₂ was obtained from core-shell Ni@rGO-MnO₂, Fe₃O₄@rGO-MnO₂ by chemical etching of Ni and Fe₃O₄ from Ni@rGO and Fe₃O₄@rGO core separately using HCl. The chemical analysis, morphology and structure were demonstrated using FTIR, EDX, FESEM, and XRD, respectively. The electrochemical energy storage performance was evaluated in a three-electrode system in 0.5 M Na₂SO₄ solution through cyclic voltammetry (CV) and galvanostatic charge-discharge techniques (GCD) within -0.1 to 0.8 V for Ni-based nanoparticles and -0.15 to 0.75 V for iron oxide-based nanocomposite and electrochemical impedance spectroscopy (EIS) of synthesized nanocomposites were studied. Core-shell Ni@rGO-MnO₂ and hollow and porous (--)@rGO-MnO₂ nanocomposite exhibited an enhanced specific capacitance (C_{sp}) of 327 F/g and 688 F/g respectively, whereas that for rGO-MnO₂ was only 189 F/g at 0.1 A/g current density within potential range -0.1 to 0.8 V. Core-shell Fe₃O₄@rGO-MnO₂ and hollow crumple (--)@rGO-MnO₂ nanocomposite showed C_{sp} 625 F/g and 1086 F/g respectively, whereas that for rGO-MnO₂ was only 252 F/g at 0.1 A/g current density within potential range -0.15 to 0.75 V. As (--)@rGO-MnO₂ exhibited low charge transfer resistance as compared to rGO-MnO₂, with extended double-layer capacitance, which is due to the combination of hollow and porous crumpled reduced graphene and embedded needle and rod-like nanostructure of manganese dioxide, are responsible for high specific capacitance with good performance in cycle stability for each case and presented the highly promising application for supercapacitors.

KEYWORDS: Supercapacitor, reduced graphene oxide, manganese oxide, core-shell nanocomposite.

Table of Contents

1	Introduction.....	1
1.1	Introduction.....	1
1.2	Objectives of the present work	4
1.3	Outline of the work.....	5
1.4	References.....	6
2	Background.....	9
2.1	Introduction of Supercapacitors.....	9
2.2	Principles of energy storage mechanism	11
2.2.1	Electrochemical Double-Layer Capacitance (EDLC)	12
2.2.2	Pseudo-Capacitance	14
2.3	Electrode materials of supercapacitors	16
2.3.1	Carbon-based EDLC materials- Graphene	17
2.4	Graphene in supercapacitors.....	19
2.5	Metal oxide-based supercapacitors	20
2.6	Metal oxide/graphene composites	22
2.7	Nano-structuring of nanomaterials for supercapacitors.....	24
2.8	References.....	26
3	Characterization Techniques	35
3.1	Fourier Transform Infrared Spectrometry	35
3.2	X-Ray Diffraction Spectroscopy (XRD)	36
3.3	Field Emission Scanning Electron Microscope (FESEM)	37
3.4	Energy Dispersive X-ray Spectroscopy (EDX).....	38
3.5	Investigation of electrochemical capacitive behavior.....	39
3.5.1	Cyclic voltammetry (CV)	39
3.5.2	Galvanostatic Charge Discharge (GCD)	41
3.5.3	Electrochemical Impedance Spectroscopy(EIS).....	42

3.5.4 Determination of energy density and power density	43
3.6 References.....	45
4 Experimental.....	47
4.1 Materials and instruments.....	47
4.2 Synthesis of materials	48
4.2.1 Synthesis of graphene oxide (GO) and reduced graphene oxide(rGO).....	48
4.2.2 Synthesis of rGO-MnO _x nanocomposite	49
4.2.3 Synthesis of Ni nanoparticles	49
4.2.4 Synthesis of core-shell Ni@rGO nanostructure and coreless (--)@rGO hollow spheres	50
4.2.5 Synthesis of core-shell Ni@rGO-MnO _x nanocomposite and coreless porous and hollow crumpled (--)@rGO-MnO _x nanosphere.....	51
4.2.6 Synthesis of Iron oxide (Fe ₃ O ₄) nanoparticles.....	51
4.2.7 Synthesis of Fe ₃ O ₄ @rGO core-shell nanostructure and coreless (--)@rGO spheres	52
4.2.8 Synthesis of Fe ₃ O ₄ @rGO-MnO _x composite and (--)@rGO-MnO _x composite	52
4.3 Structural Characterization by X-Ray Diffraction (XRD).....	53
4.4 Surface morphology by Field Emission Scanning Electron Microscope (FESEM)	53
4.5 Chemical Characterization.....	54
4.5.1 Fourier Transform Infrared spectroscopy (FTIR).....	54
4.5.2 Elemental analysis by Energy Dispersive X-Ray (EDX) spectroscopy	54
4.6 Investigation of electrochemical capacitive behavior.....	55
4.6.1 Experimental setup	55
4.6.2 Electrochemical analysis	56
4.7 References:	57
5 Results and Discussion	58

5.1 Synthesis of Materials: Steps of Reactions.....	58
5.1.1 Synthesis of Graphene Oxide (GO) and Reduced Graphene Oxide (rGO).....	58
5.1.2 Synthesis of Ni nanoparticles, Ni@rGO-MnO ₂ and porous crumpled (--@rGO-MnO ₂	59
5.1.3 Synthesis of Fe ₃ O ₄ , core-shell Fe ₃ O ₄ @rGO-MnO ₂ nanocomposite, and hollow crumpled (--@rGO-MnO ₂ composite.....	60
5.2 Characterization.....	61
5.2.1 Structural Characterization by X-Ray Diffraction (XRD) analysis.....	61
5.2.2 Chemical Characterization -Elemental analysis by EDX.....	66
5.2.3 Chemical characterization by FTIR analysis:.....	72
5.2.4 Morphology study by FESEM Analysis.....	77
5.3 Investigation of electrochemical performance of Ni-based nanocomposite.....	81
5.3.1 CV & GCD of rGO, Ni@rGO, and hollow (--@rGO	81
5.3.2 CV and GCD of rGO-MnO ₂ nanocomposite.....	85
5.3.3 CV and GCD of Ni@rGO-MnO ₂ nanocomposite	86
5.3.4 CV and GCD of hollow and porous (--@rGO-MnO ₂ nanocomposite.....	88
5.4 Comparative studies on electrochemical performances of Ni-based nanomaterials	90
5.4.1 CV and GCD analysis.....	90
5.4.2 Determination of energy density and power density	92
5.4.3 EIS analysis	94
5.4.4 Cycle stability of (--@rGO-MnO ₂ from Ni@rGO-MnO ₂	96
5.5 Investigation of electrochemical performance of iron oxide-based nanocomposite	98
5.5.1 CV and GCD of rGO, Fe ₃ O ₄ @rGO and hollow crumpled (--@rGO.....	98
5.5.2 CV and GCD of rGO-MnO ₂ nanocomposite.....	101
5.5.3 CV and GCD of Fe ₃ O ₄ @rGO-MnO ₂ nanocomposite.....	102
5.5.4 CV and GCD of hollow crumpled (--@rGO-MnO ₂ nanocomposite.....	104

5.6 Comparative investigation for iron oxide-based nanomaterials on electrochemical performances.....	106
5.6.1 CV and GCD analysis.....	106
5.6.2 Determination of energy density and power density	108
5.6.3 EIS Analysis	110
5.6.4 Cycle stability analysis of (-)-@rGO-MnO ₂ from Fe ₃ O ₄ @rGO-MnO ₂	112
5.7 References.....	115
6 Conclusions.....	122

List of Figures

Figure 1.1: SDG 7 th goal and other six goals related to 7 th goal by UN.....	1
Figure 1.2: Illustrative formation of the composite.....	2
Figure 2.1: A simplified Ragone plot of specific power versus specific energy for various energy storage devices [9,10].	11
Figure 2.2: Schematic representation of electrical double layer structures according to (a) the Helmholtz model, (b) the Gouy-Chapman model, and (c) the GouyChapman-Stern model. The double-layer distance in the Helmholtz model and the Stern layer thickness are denoted by H while ψ_s are the potential at the electrode surface	13
Figure 2.3: Schematic representation of a porous carbon EDLC in a charged (left) and discharged state (right)	14
Figure 2.4: Different types of reversible redox mechanisms that give rise to pseudocapacitance: (a) underpotential deposition, (b) redox pseudocapacitance, and (c) intercalation pseudocapacitance[20].....	15
Figure 2.5: (a) Schematic of free-standing graphene, (b) Graphene: Mother of all graphitic forms: Buckyballs (Fullerene-0D); carbon nanotube (1D); graphite (3D)[42].	18
Figure 2.6: Schematic sp^2 hybridized C-C bond structure of graphene containing in-plane σ -bonds and perpendicular π -bonds.....	19
Figure 2.7: (a) Graphene molecule showing sp^2 bonds, (b) Graphene molecule showing pi orbitals and (c) Graphene molecule showing sp^2 and pi orbitals.....	19
Figure 2.8: Crystal structures of manganese oxides with various oxidation states	21
Figure 3.1: A digital image of Shimadzu-FTIR-8400 FTIR machine	35
Figure 3.2 PANALYTICAL EMPYREAN X-ray Diffractometer.....	37
Figure 3.3 A photo of SEM JSM-7600F.....	38
Figure 3.4 (a) Current excitation and (b) potential response in GCD	41
Figure 3.5 Potential response of an ideal electrochemical capacitor in GCD.....	41
Figure 3.6 An R.L.C series circuit	42
Figure 3.7(a) A typical Nyquist plot and (b) its equivalent circuit.....	43
Figure 4.1: Schematic flowchart for the synthesis of Ni NPs.....	50
Figure 4.2: A flowchart shows all pathway of Ni-based materials synthesis.....	51
Figure 4.3: A flowchart shows all pathway of Fe_3O_4 based materials synthesis	53
Figure 4.4: Electrochemical cell of three electrode system.....	55

Figure 5.1: XRD patterns of (a) (--)rGO (b)rGO-MnO ₂ (c) Ni@rGO-MnO ₂ (d) (--)@rGO-MnO ₂	62
Figure 5.2: XRD patterns of (a) (--)rGO (b)rGO-MnO ₂ (c) Fe ₃ O ₄ @rGO-MnO ₂ (d) (--)@rGO-MnO ₂	64
Figure 5.3: EDX spectra at three locations (01, 02 and 03) of (--)@rGO from Ni@rGO.	66
Figure 5.4: EDX spectra at three locations (01, 02 and 03) of rGO-MnO ₂	67
Figure 5.5: EDX spectra at three locations (01, 02 and 03) of Ni@rGO-MnO ₂	68
Figure 5.6: EDX spectra at three locations (01, 02 and 03) of (--)@rGO-MnO ₂	69
Figure 5.7: EDX spectra at three locations (01, 02 and 03) of (--)@rGO from Fe ₃ O ₄ @rGO	70
Figure 5.8: EDX spectra at three locations ((1, 2 and 3) of Fe ₃ O ₄ @rGO-MnO ₂ core-shell.	71
Figure 5.9: EDX spectra at three locations (1, 2 and 3) of core-shell Fe ₃ O ₄ @rGO-MnO ₂	72
Figure 5.10: FTIR spectrum of GO, rGO sheet, Ni@rGO, and hollow (--)@rGO nanosphere.	73
Figure 5.11: FTIR spectrums of rGO-MnO ₂ , core-shell Ni@rGO-MnO ₂ , and hollow crumpled (--)@rGO-MnO ₂ nanocomposite.....	74
Figure 5.12: FTIR spectrum of GO, rGO sheet, Fe ₃ O ₄ @rGO, and hollow porous (--)@rGO	75
Figure 5.13: FTIR spectrums of rGO-MnO ₂ , Fe ₃ O ₄ @rGO-MnO ₂ , and hollow crumpled (--)@rGO-MnO ₂ nanocomposite.....	76
Figure 5.14: FESEM images of (a) rGO (b) (--)@rGO from Ni@rGO (c) Ni@rGO-MnO ₂ and (d) (--)@rGO-MnO ₂ from Ni@rGO-MnO ₂	78
Figure 5.15: FESEM image of (a) rGO sheet (b) (--) @rGO from Fe ₃ O ₄ @rGO (c) Fe ₃ O ₄ @rGO-MnO ₂ and (d) (--) @rGO-MnO ₂ from Fe ₃ O ₄ @rGO-MnO ₂	80
Figure 5.16: CV curves of (a-c) within potential window -0.1 to 0.8 V at different scan rates (2, 5, 10, 20, and 50 mV/s) and GCD curves (d-f) at different current densities (0.1, 0.15, 0.2, 0.25, 0.5, 0.7, and 0.9 A/g) of rGO, Ni@rGO, (--)@rGO respectively.....	82
Figure 5.17: C _{sp} (F/g) of (a-c) at different current densities (0.1, 0.15, 0.2, 0.25, 0.5, 0.7 and 0.9 A/g) of rGO, Ni@rGO, (--)@rGO within potential window -0.1 to 0.8 V, respectively.....	84

Figure 5.18: (a) CV at different scan rates (2, 5, 10, 20 and 50 mV/s) (b) GCD at different current densities (0.1, 0.15, 0.2, 0.25, 0.5, 0.7 and 0.9 A/g) (c) C_{sp} (F/g) at different current densities within potential window -0.1 to 0.8 V of rGO-MnO ₂ .	85
Figure 5.19: (a) Cyclic voltammetry curves at different scan rates (2, 5, 10, 20 & 50 mV/s) (b) GCD curves at different current densities (0.1, 0.15, 0.2, 0.25, 0.5, 0.7, and 0.9 A/g) (c) Specific capacitance(F/g) at different current densities within potential window -0.1 V to 0.8 V of Ni@rGO-MnO ₂	87
Figure 5.20: (a) CV curves at different scan rates (2, 5, 10, 20 and 50 mV/s) (b) GCD curves at different current densities (0.1, 0.15, 0.2, 0.25, 0.5, 0.7, and 0.9 A/g) (c) C_{sp} (F/g) at different current densities within potential window -0.1 to 0.8 V of hollow (--)@rGO-MnO ₂ .	89
Figure 5.21: (a) CV curve at scan (5 mV s ⁻¹) (b) GCD curve at current density (0.1 A/g) (c) and (d) C_{sp} (F/g) at current density (0.1 A/g) within -0.1 V to 0.8 V of Ni-based nanomaterials	91
Figure 5.22: Ragone plot for energy density and power density of Ni-based nanomaterials	93
Figure 5.23. Nyquist plots of the pure rGO-MnO ₂ , Ni@ rGO-MnO ₂ , and (--)@rGO-MnO ₂ electrodes.	95
Figure 5.24: Randles circuit representing the equivalent circuit for the nanocomposites under experiment.	96
Figure 5.25: The GCD curve of (--)@rGO-MnO ₂ (a) first 5 cycles (left) and (b) last (right) 5 cycles for 1000 and (c) capacitance retention profile of the rGO-MnO ₂ , Ni@rGO-MnO ₂ and (--)@rGO-MnO ₂ within -0.1 – 0.8 V at 5 A/g for (d) (--)@rGO-MnO ₂ within -0.1 to 0.8 V at 5 A/g for 1000 cycles.	97
Figure 5.26: CV curves (a,c,e) within potential window -0.15 to 0.75V at different scan rates (2, 5, 10, 20, and 50 mV/s) and GCD curves (b,d,f) at different current densities (0.1, 0.15, 0.2, 0.25, 0.5, 0.7 and 0.9 A/g) of rGO, Fe ₃ O ₄ @rGO, (--)@rGO, respectively.	99
Figure 5.27: C_{sp} (F/g) of (a-c) at different current densities (0.1, 0.15, 0.2, 0.25, 0.5, 0.7 and 0.9 A/g) of , core-shell Fe ₃ O ₄ @rGO, and (--)@rGO within potential window -0.15 to 0.75 V, respectively.	100
Figure 5.28: (a) CV curves at different scan rates (2, 5, 10, 20 and 50 mV/s) (b) GCD curves at different current densities (0.1, 0.15, 0.2, 0.25, 0.5, 0.70, and 0.9 A/g) (c) C_{sp} (F/g) at different current densities of rGO-MnO ₂ within -0.15 to 0.75 V.	101

Figure 5.29: (a) CV curves at different scan rates (2, 5, 10, 20 and 50 mV/s) (b) GCD curves at different current densities (0.1, 0.15, 0.2, 0.25, 0.5, 0.7 and 0.9 A/g) (c) C_{sp} (F/g) at different current densities within potential window -0.15 to 0.75 V of $\text{Fe}_3\text{O}_4@\text{rGO-MnO}_2$ 103

Figure 5.30: (a) Cyclic voltammetry curves of $(-\text{-})@\text{rGO-MnO}_2$ various scan rates within -0.15 V to 0.75 V (b) Galvanostatic charge-discharge curves at different current densities (0.10, 0.15, 0.20, 0.25, 0.50, 0.70, and 0.90 A/g) and (c) specific capacitance as a function of current density for $(-\text{-})@\text{rGO-MnO}_2$ 105

Figure 5.31: Comparative (a) CV (b) GCD curves and (c & d) specific capacitances with current densities of rGO-MnO_2 , $\text{Fe}_3\text{O}_4@\text{rGO-MnO}_2$, and $(-\text{-})@\text{rGO-MnO}_2$ nanocomposite. 107

Figure 5.32: Nyquist plots of the(a) rGO-MnO_2 (b) $\text{Fe}_3\text{O}_4@\text{rGO-MnO}_2$ (c) $(-\text{-})@\text{rGO-MnO}_2$ 110

Figure 5.33: Randles circuit representing the equivalent circuit for the nanocomposites under experiment 111

Figure 5.34: The GCD Curve of $(-\text{-})@\text{rGO-MnO}_2$ a) first 5 cycles (left) and b) last (right) 5 cycles for 1000 cycles (c) Capacitance retention profile of the $(-\text{-})@\text{rGO-MnO}_2$ within -0.15 to 0.75 V at 5 A/g for 1000 cycles. 112

List and flowcharts

Flow chart 2-1: Classification of supercapacitors..... 12

Flow chart 4-1: Synthesis process for obtaining of MnO_x nanoparticles on the surface of rGO nanosheets.....49

List of Tables

Table 5-1: The crystal plane with $2\theta(^{\circ})$ of synthesized nanoparticles	63
Table 5-2: The crystal plane with $2\theta(^{\circ})$ of synthesized nanoparticles	65
Table 5-3: Elemental composition of $(-)\text{@rGO}$	66
Table 5-4: Elemental composition of rGO-MnO_2	67
Table 5-5: Elemental composition of Ni@rGO-MnO_2	68
Table 5-6: Elemental composition of $(-)\text{@rGO-MnO}_2$	69
Table 5-7: Elemental composition of rGO	70
Table 5-8: Elemental composition of $\text{Fe}_3\text{O}_4\text{@rGO-MnO}_2$	71
Table 5-9: Elemental composition of $(-)\text{@rGO-MnO}_2$	72
Table 5-10: FTIR bands of Ni NPs based nanomaterials	73
Table 5-11: FTIR bands for Ni NPs based nanomaterials	74
Table 5-12: FTIR band of iron oxide-based nanomaterials	75
Table 5-13: FTIR bands for iron oxide-based nanomaterials	76
Table 5-14: Calculated specific capacitance for of rGO , Ni@rGO and hollow $(-)\text{@rGO}$	83
Table 5.15: The obtained values of R_s , C_{dl} , C_p , R_{ct} for Ni-based nanomaterials.....	95
Table 5-16: The obtained values of R_s , C_{dl} , C_p , R_{ct} for iron oxide-based nanomaterials	111

Chapter-1

Introduction

1 Introduction

1.1 Introduction

The progress of science and technological designs with enormous industrialization and civilization is marked by the emergence of new, progressively amazing high-tech facilities along with various natural or environmental crises and civic life limitations [1]. To resolve these apprehensions, the scientific community have devoted their efforts to find a appropriate solution through the effective utilization of the limited resources by developing innovative materials, technologies for exessing the ultimate future that we dream of today. Nowadays most of our daily life gadgets e.g. smartphone, tablet PC, watch, laptop, car etc is dependent on energy i.e battery. The dream of energy efficient power systems or the environmentally benign electric vehicle of the future is also largely dependent on the development of high capacity charge storage materials [2]. Although most of these devices largely depend on batteries for prolonged power supply, if supercapacitors provide support for different power loads thereby reducing stress on the battery.

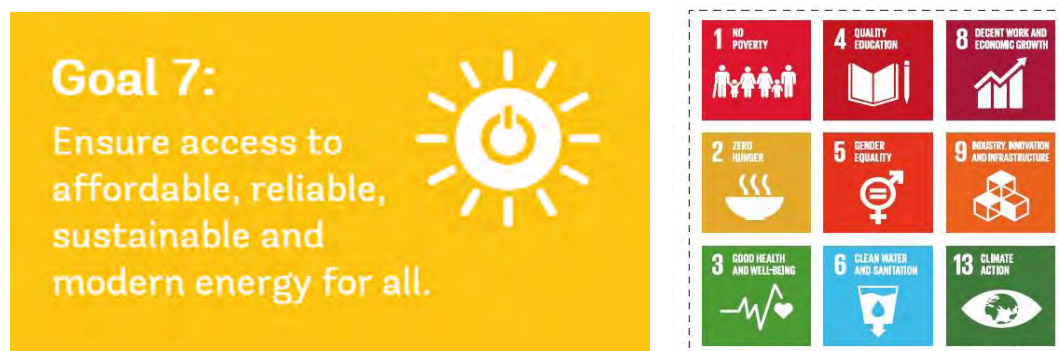


Figure 1.1: SDG 7th goal and other six goals related to 7th goal by UN

Electrical double-layer capacitors (EDLC) (also known as electrochemical or supercapacitors) is a new innovative resolve of energy sector for their advantageous characteristics over batteries and conventional capacitors which explore their suitability in the areas of applications of interest to ensure affordable and clean energy

goal no. 7 among the goals for SDG, 2030 set up by United Nations (UN) [3,4]. It fills the gap between batteries and conventional capacitors because they have higher energy density than conventional dielectric capacitors and have higher power density and a long cycling life than batteries due to the involvement of no or negligibly small chemical charge transfer reactions [5].

Many research efforts have been focused towards the combination of pseudocapacitive (metal oxide and polymer-based) and carbon-based EDLC materials to capture high capacitance values of the former without any cycle life penalty typically associated with their use [6,7] which is strongly depends on the intrinsic properties of their constituent materials and their eventual architectural design [8]. Graphene, developed only in 2004 by A. Geim and K. Novoselov [9,10], is a new materials also known ‘super carbon’ [11] with a one-atom-thick 2D sheet of carbon atoms fashioned in a honeycomb lattice as the future revolutionary material [12]. It has many unique properties including reactivity from both sides [13], large theoretical surface area ($2630 \text{ m}^2/\text{g}$) [14], high electron mobility ($200000 \text{ cm}^2/\text{Vs}$) [14], high Youngs modulus ($\sim 1 \text{ TPa}$) [14], good optical transparency ($\sim 90\%$) [14] etc. However, it suffers from a serious drawback that the pure graphene sheet tends to undergo stacking [15].

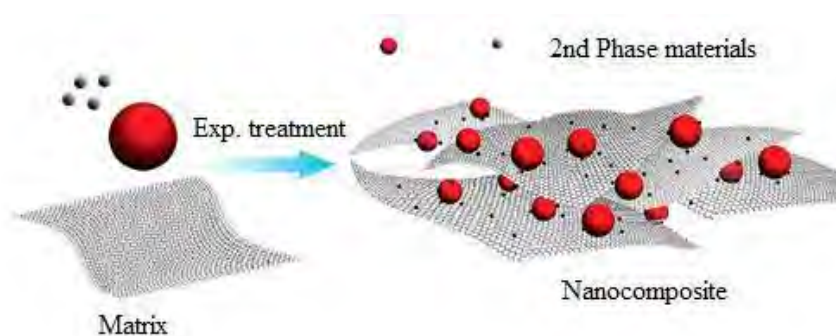


Figure 1.2: Illustrative formation of the composite.

Graphene-based metal oxide nanocomposites are recent addition among the class of nanocomposites to overcome the horizontal lameller stacking of graphene[16]. Due to their low cost, environmental benignity and easy synthesis [17,18], they have drawn much attention from researchers and have been applied as electrochemical charge storage material. e.g. Qian *et al.* synthesized graphene/ MnO_2 composite by a polymer-assisted chemical reduction method in 2011 revealed a high specific capacitance of 324 F/g in $1 \text{ M Na}_2\text{SO}_4$ electrolyte with excellent long-term cycle stability [18]. Yang *et al.*

synthesized reduced graphene nanosheet/urchin-like manganese dioxide (GNS/MnO₂) composite exhibited a maximum specific capacitance of 263 F/g with a capacity retention of about 99% after 500 cycles. Zaid et.al. reported G/Ni nanocomposite with high specific capacitance 275 F/g at 2 A/g current density synthesized via ball mill process [19]. Zhang. Li. reported graphene/manganese dioxide (MnO₂) composite papers (GMCP) with the specific capacitance of the GMCP was 256 F/g at a current density of 0.5 A/g in 2011 [20]. Peng et al. reported a facile method of hybrid nanostructure of quasi-2D ultrathin MnO₂/graphene nanosheets with high specific capacitances of 267 F/g at current density of 0.2 A/g and exhibits excellent rate capability and cycling stability with capacitance retention of 92% after 7000 cycles [21]. Ye *et al.* reported a facile method to prepare MnO₂/reduced graphene oxide (rGO) composites in 2013 as electrodes in flexible solid-state supercapacitors [22]. Huang *et al.* reported in 2015 MnO₂/graphene nanocomposite synthesis technique through a water-reflux condenser system with the specific capacitance as high as 350 F/g at 1A/g [23]. Wen *et al.* developed a facile method to prepare the MnO₂-graphene composite in 2015 with a sandwich structure retained a capacity of 752 mAh/g at a current density of 100 mA/g after 65 cycles [23]. Sun et al. reported in 2015 a green and low-cost approach for the synthesis of 3D porous MnO₂/rGO/Ni composite foam via a solution chemical method with higher capacitance of 479.0 F/g at 1.0 A/g and the capacitance retention of 83.5% of its initial value after 1000 cycles [24]. Zhou et al. reported in 2016 a method of MnO₂/GNS hybrid synthesis by one-pot electrochemical co-deposition with boosts the capacitive behaviors and cycle stability of MnO₂, in particular, the MnO₂/GNS hybrid shows a high specific capacitance of 413.1 F/g [25]. Sadak et al. reported in 2019 reported a green cost-effective method to produce free-standing, flexible, and highly conductive electrochemically exfoliated graphene paper (GrP) deposited nanoflower like manganese dioxide (MnO₂) electrochemically and exhibited a high specific capacitance of 385.2 F/g at 1 mV/s in 0.1 M Na₂SO₄ electrolyte and outstanding capacitance retention after 5000 consecutive cycles [26].

Owing to the high surface area of 2D materials offer a unique opportunity to surpass the current limitations of electrode materials. Even though 2D materials like graphene, has the great advantage of using for supercapacitor electrode materials its high conductivity and large surface area but they are composited with conducting polymer or transition metal oxides to improve the energy density of pristine graphene-based

devices with improving high thermal stability and mechanical strength with minimum restacking of 2D layers. However, these 2D layers undergo stacking to accomplish a considerable volume poses a major challenge and affect the performance of electrode materials. As the crumpled and furrowed graphene balls or hollow structure have a larger surface area and better-defined voids for electron and ion transport compared to free at or wrinkled sheets [27]. Qin et al reported in 2013 graphene hollow sphere with excellent electrochemical performance (C_{sp} 273 F/g) than flat graphene [28] but the energy density of this materials is not adequate for application. Modified crumple or hollow spherical conductive materials as a templates or templates with an active materials core having a controlled pore size distribution compare to flat conductive materials, and depositing pseudocapacitive materials like metal oxide with different shape may significantly improve the scalability of graphene-metal oxide-based electrode materials to construct high performing supercapacitor electrodes. However, by the acknowledgment of the existing state of research, the influence of Ni and iron oxide NPs as the active core or modifier of rGO-MnO₂ composite and extend crumple or hollow spherical rGO-MnO₂ material was not studied yet. On focusing on this gap of rGO-MnO₂ based electrode materials in the present study, an attempt will be made to study the influence of metal nanoparticles and metal oxides on the electrochemical capacitance of rGO-MnO_x nanoparticle. For this study, we will attempt to synthesize rGO-MnO_x, Ni@rGO@MnO_x core-shell nanocomposite, Fe₃O₄@rGO-MnO_x core-shell nanocomposite and crumple hollow (--)@rGO-MnO_x nanosphere. It is expected that the combination of these nanomaterials leads to a new generation of supercapacitors electrodes with high energy and power densities in the near future.

1.2 Objectives of the present work

The main objectives of this present work are to

1. fabricate Ni@rGO-MnO_x, Fe₃O₄@rGO-MnO_x, nanocomposite by incorporation of Ni and iron oxides (Fe₃O₄) nanoparticles in the core and (--)@rGO-MnO_x by the removal of the core (Ni, Fe₃O₄).
2. comprehend the composition and morphology-dependent chemical and physical properties of the synthesized nanocomposite.
3. rationalize the specific capacitance and cyclic stability of Ni@rGO-MnO_x, Fe₃O₄@rGO-MnO_x, and (--)@rGO-MnO_x nanocomposites.

1.3 Outline of the work

Graphene oxide (GO) was synthesized from graphite powder following a modified Hummers method as the starting material for rGO. Ni NPs was synthesized from NiCl₂ and hydrazine hydrate and NaOH. The iron oxide was synthesized by the co-precipitation method using precursor mixture FeSO₄ and FeCl₃.6H₂O with a ratio 1:2 at 60°C for 3h vigorous stirring. Ni@rGO and Fe₃O₄@GO was prepared from GO and Ni NPs, GO and iron oxides respectively by the sonochemical process. rGO, Ni@rGO, Fe₂O₃@rGO, and Fe₃O₄@rGO was prepared by reduction using hydrazine hydrate and NH₄OH. The incorporation of MnO_x on Ni@rGO and Fe₃O₄@rGO was achieved by the reaction of benzyl alcohol and KMnO₄ for the synthesis of the ternary composite Ni@rGO-MnO_x, Fe₃O₄@rGO-MnO_x, respectively. (--)@rGO and (--)@rGO-MnO_x was prepared by etching the nickel and iron oxide NPs using HCl solution from Ni@rGO and Ni@rGO-MnO_x, Fe₂O₃@rGO-MnO_x, Fe₃O₄@rGO-MnO_x, respectively. The surface morphology of the synthesized samples was analyzed by FESEM (Field Emission Scanning Electron Microscope), structures was determined from XRD (X-Ray Diffraction) and chemical characterization of the nanocomposite was carried out by EDX and FTIR. The electrochemical capacitance, cycle stability, and electrical impedance was measured by cyclic voltammetry, galvanostatic charge-discharge technique, and electrochemical impedance spectroscopic method, respectively. In these techniques, the modified graphite electrode was used as a working electrode in a three-electrode system by using benign Na₂SO₄ electrolyte.

1.4 References

- [1] Dobrzański, L. A., “Significance of materials science for the future development of societies”, *J. Mater. Process. Technol.*, vol. 175(1–3), pp. 133–148, 2006.
- [2] Xing, S., Zhou, Z., Ma, Z., and Wu, Y., “Facile synthesis and electrochemical properties of Mn₃O₄ nanoparticles with a large surface area”, *Mater. Lett.*, vol. 65(3), pp. 517–519, 2011.
- [3] Gare, A., “Narratives and the ethics and politics of environmentalism: The transformative power of stories”, *Theory Sci.*, vol. 2(1), pp. 5–7, 2001.
- [4] Moran, D. D., Wackernagel, M., Kitzes, J. A., Goldfinger, S. H., and Boutaud, A., “Measuring sustainable development - Nation by nation”, *Ecol. Econ.*, vol. 64(3), pp. 470–474, 2008.
- [5] Sharma, K., Arora, A., and Tripathi, S. K., “Review of supercapacitors : materials and devices”, *J. Energy Storage*, vol. 21, pp. 801–825, 2019.
- [6] Aboutalebi, S. H., Chidembo, A.T., Salari, M., Konstantinov, K., Wexler, D., Liu, H. K., and Dou, S. X., “Comparison of GO, GO/MWCNTs composite and MWCNTs as potential electrode materials for supercapacitors”, *J. Energy and Environ. Sci.*, vol. 4(5), pp. 1855–1865, 2011.
- [7] Chen, S., Zhu, J., Wu, X., Han, Q., and Wang, X., “Graphene Oxide- MnO₂ supercapacitors”, *ACS Nano.*, vol. 4(5), pp. 2822–2830, 2010.
- [8] Chidembo, A., Aboutalebi, S. A., Konstantinov, K., Salari, M., Yamini, S.A., Nevirkovets, I. P., Winton, B., and Liu, H. K., “Globular reduced graphene oxide-metal oxide structures for energy storage applications”, *Energy Environ. Sci.*, vol. 5(1), pp. 5236–5240, 2012.
- [9] Novoselov, K. S., Geim, A. K., Morozov, S V., Jiang, D., Zhang, Y., Dubonos, S. V., Grigorieva, I.V, Firsov, A. A., “Electric field effect in atomically thin carbon films”, *Science.*, vol. 5(1), pp. 1–12, 2004.
- [10] Novoselov, K S., Jiang, D., Schedin, F., Booth, T. J., Khotkevich, V. V., Morozov, S., Geim, A K., “Two dimensional atomic crystals”, *Proceedings of the National Academy of Sciences of the United States of America.*, vol. 102(30), pp. 10451–10453, 2005.
- [11] Peplow, M., “Graphene: The quest for super carbon”, *Nature*, vol.503(7476), pp. 4–5, 2013.

- [12] Singh, V., Joung, D., Zhai, L., Das, S., Khondaker, S. I., and Seal, S., “Graphene based materials: Past, present and future”, *Prog. Mater. Sci.*, vol. 56(8), pp. 1178–1271, 2011.
- [13] Sharma, R., Baik, J. H., Perera, C. J., and Strano, M. S., “Anomalously large reactivity of single graphene layers and edges toward electron transfer chemistries”, *Nano Lett.*, vol. 10(2), pp. 398–405, 2010.
- [14] Majeed, A., Ullah, W., Anwar, A. W., Nasreen, F., Sharif, A., Mustafa, G., and Khan, A., “Graphene-metal oxides/hydroxide nanocomposite materials: Fabrication advancements and supercapacitive performance”, *J. Alloys Compd.*, vol. 671, pp. 1-10, 2016.
- [15] Chen, K., Wang, Q., Niu, Z., and Chen, J., “Graphene-based materials for flexible energy storage devices”, *J. Energy Chem.*, vol. 27(1), pp. 12–24, 2018.
- [16] Wang, B., Wang, Y., Park, J., Ahn, H., and Wang, G., “*In-situ* synthesis of Co₃O₄/graphene nanocomposite material for lithium-ion batteries and supercapacitors with high capacity and supercapacitance”, *J. Alloys Compd.*, vol. 509(29), pp. 7778–7783, 2011.
- [17] Amini, M., Najafpour, M. M., Nayeri, S., Pashaei, B., and Bagherzadeh, M., “Nano-layered manganese oxides as low-cost, easily synthesized, environmentally friendly and efficient catalysts for epoxidation of olefins”, *RSC Adv.*, vol. 2(9), pp. 3654–3657, 2012.
- [18] Qian, Y., Lu, S., and Gao, F., “Preparation of MnO₂/graphene composite as electrode material for supercapacitors”, *J. Mater. Sci.*, vol. 46(10), pp. 3517–3522, 2011.
- [19] Akmal, N., Zaid, M., and Idris, N. H., “Enhanced capacitance of hybrid layered graphene / nickel nanocomposite for supercapacitors”, *Nat. Scientific Reports.*, vol. 6, pp. 1–8, 2016.
- [20] Zhang, Y., Su, M., Ge, L., Ge, S., Yu, J., and Song, X., “Synthesis and characterization of graphene nanosheets attached to spiky MnO₂ nanospheres and its application in ultrasensitive immunoassay”, *Carbon .*, vol. 57, pp. 22–33, 2013.
- [21] Peng, L., Peng, X., Liu, B., Wu, C., Xie, Y., and Yu, G., “Ultrathin two-dimensional MnO₂/graphene hybrid nanostructures for high-performance, flexible planar supercapacitors”, *Nano Lett.*, vol. 13,(5), pp. 2151–2157, 2013.

- [22] Ye, K. H., Liu, Z. Q., Xu, C. W., Li, N., Chen, Y. B., and Su, Y. Z., “MnO₂/reduced graphene oxide composite as high-performance electrode for flexible supercapacitors”, *Inorg. Chem. Commun.*, vol. 30, pp. 1–4, 2013.
- [23] Wen, K., Chen, G., Jiang, F., Zhou, X., and Yang, J., “A facile approach for preparing MnO₂-graphene composite as anode material for lithium-ion batteries”, *Int. J. Electrochem. Sci.*, vol. 10(5), pp. 3859–3866, 2014.
- [24] Sun, Y., Zhang, W., Li, D., Gao, L., Hou, C., and Zhang, Y., “Facile synthesis of MnO₂ / rGO / Ni composite foam with excellent pseudocapacitive behavior for supercapacitors”, *J. Alloys Compd.*, vol. 649, pp. 579–584, 2015.
- [25] Zhou, H., and Zhai, H. J., “Rapid preparation of the hybrid of MnO₂ dispersed on graphene nanosheets with enhanced supercapacitive performance”, *Electrochim. Acta.*, vol. 215, pp. 339–345, 2016.
- [26] Sadak, O., Wang, W., Guan, J., Sundramoorthy, A. K., and Gunasekaran, S., “MnO₂ nanoflowers deposited on graphene paper as electrode materials for supercapacitors”, *ACS Appl. Nano Mater.*, vol. 2(7), pp. 4386–4394 2019.
- [27] Luo, J., Jang, H. D., and Huang, J., “Effect of sheet morphology on the scalability of graphene-based ultracapacitors”, *ACS Nano.*, vol. 7(2), pp. 1464–1471, 2013.
- [28] Shao, Q., Tang, J., Lin, Y., Zhang, F., Yuan, J., Zhang, H., Shinya, N., Qin, L.C., “Synthesis and characterization of graphene hollow spheres for application in supercapacitors”, *J. Mater. Chem. A.*, vol. 1 pp. 15423–15428, 2013.

Chapter-2

Background

2 Background

2.1 Introduction of Supercapacitors

Supercapacitors are a type of energy storage devices with high energy density, power density and cycle life that employ the electrical double layer storage charge mechanism on the electrode-electrolyte interface and pseudocapacitive mechanism on the surface and near-surface fast and reversible redox process which bridges the gap between electrolytic capacitors and rechargeable batteries. It is also known as electrochemical capacitors ultracapacitors or gold capacitors. Owing to using of materials with high surface area and high porous and excellent conductive substances, supercapacitors are able to charge and discharge quickly resulting in a high-power delivery over a short space of time hence their increased use in portable electronics, automobiles, buses, trains, cranes and elevators due to short charge-discharge time that means required high power density. Supercapacitors satisfy the discrepancy of batteries can store more energy (high energy density), the rate at which they dispense this energy is very slow and a traditional electric capacitor less energy which they can deliver very quickly i.e. high-power density [1-3].

At this time supercapacitors along with batteries, fuel cells are being cast-off for a wide range of applications. As they are only differing in their mechanisms of charge storage, which consequently determine their energy storage capabilities. While supercapacitors and batteries are closed systems where charge is stored in the electrode material, fuel cells are open systems which rely on the supply of fuel (hydrogen or methanol) and an oxidant (oxygen or air) to operate [1-4] As long as a continuous supply of fuel (hydrogen, methanol or oxygen depending on the type of fuel cell) is maintained, the life cycle of a fuel cell is much longer than that of a battery. Due to their high energy storage capability, fuel cells are more attractive than batteries and find their use in interplanetary applications, are still more expensive to manufacture. Due to the modest pathway of energy generation concept based on chemical reactions at the anode and cathode resulting in high energy density, although the rate of energy delivery is not very

outstanding, the extent of application of batteries in day to day enchanting more attractive future markets. Due to a large amount of energy per unit weight or volume Lithium-ion batteries (LiBs), are getting a lot of devotion in both the portable electronic markets and transportation applications. Due to the chemical reactions that occur on the electrode/electrolyte interphase in the battery have short cycle life, despite the tremendous achievements reported on the Li-ion batteries, they still face major challenges in terms of cycle life and maintaining thermodynamic stability. For repressing these challenges, researchers are now focusing on optimizing the electrode material for effective Li-ion intercalation and improving the power density at the same time maintaining the energy storage capacity [5].

By means of functionality of batteries the long cycle life and fast charging depends on chemical energy stored mechanisms in the bulk of the electrode material which is a limiting factor for enhancing the power of batteries, supercapacitors store energy by charge separation which possesses high power and can be charged or discharged in seconds while owning a long cycle life. Supercapacitors are classified mainly by the charge storage mechanism that depends on electrode materials used in the manufacture and the fabrication process. Two class of supercapacitors eminent, namely: Electrical double-layer capacitors (EDLCs) and pseudocapacitors. The former makes use of the electrical double layer on the electrode/electrolyte interface for charge storage while the latter relies on the surface or near surfaces faradaic reactions on the electrode-electrolyte interface [6]. Owing to the differences in their charge storage mechanisms, supercapacitors possess high power density but still offer low energy density when compared to batteries and fuel cells [7]. To overawed this challenge, therefore, it needs to find a single energy storage device with both high energy and power densities or alternatively to improve the energy density of ECs to match those of lithium-ion batteries or coupling of both devices to produce hybrid energy storage devices to ensure longevity in power supply. At present most of the research, therefore, is focused on increasing the energy storage capabilities of supercapacitors with little or no penalty in the power capabilities by developing functional materials for electrode manufacture [8].

Fig. 2.1 shows a typical Ragone plot showing the performance of different energy storage devices where batteries and fuel cells can store more energy and the delivery time of this energy is longer than a capacitor which stores less energy but has the ability

to quickly discharge and rapidly release large amounts of power resulting in a high-power density. This is due to the interfacial nature of its charge storage mechanism while batteries rely on the use of deep-lying pores and chemical reactions situated within the electrode. Supercapacitors, serve as intermediate systems that bridge the power & energy gap between traditional capacitors (high power) and batteries (high energy) [7].

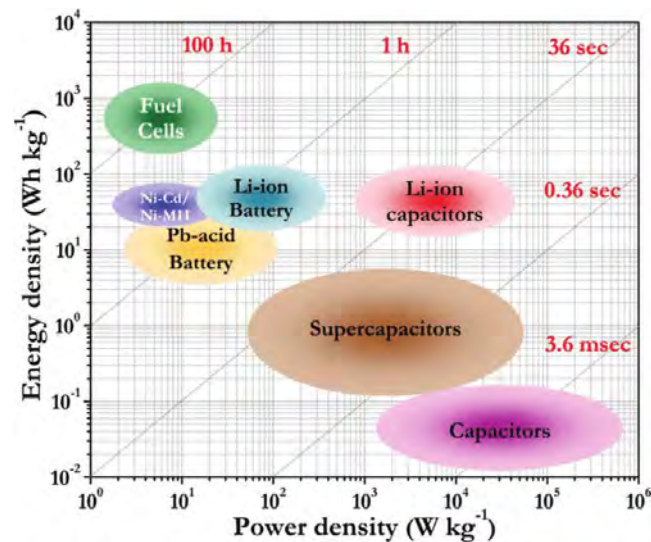
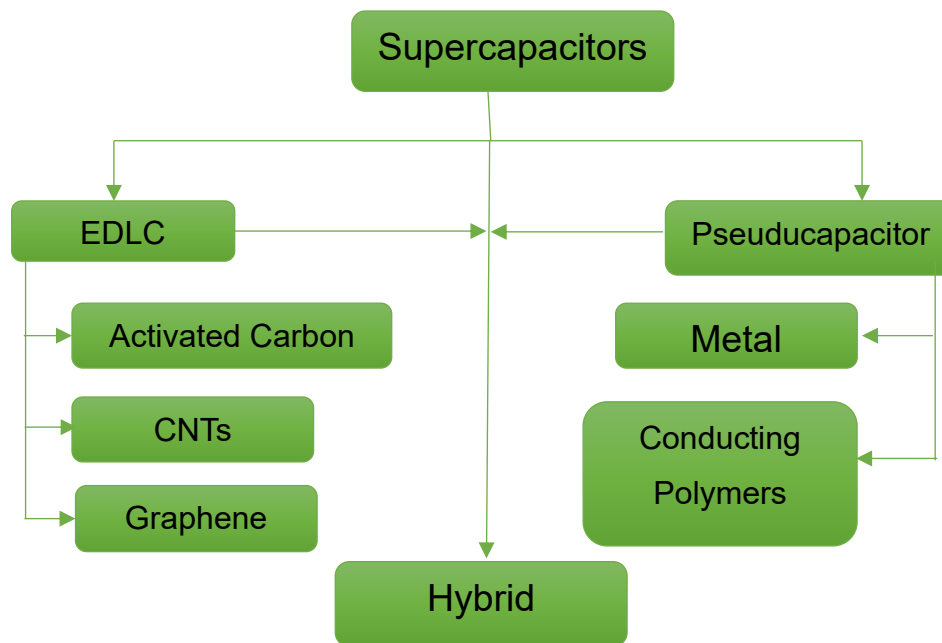


Figure 2.1: A simplified Ragone plot of specific power versus specific energy for various energy storage devices [9,10].

2.2 Principles of energy storage mechanism

The energy storage mechanisms of supercapacitors can be assembled into two categories so-called electrochemical double-layer mechanism due to electrostatic attraction as in electrical double-layer capacitors in which non-faradaic reactions occur and pseudocapacitive behavior which arises due to faradaic reactions similar to the processes proceeding in accumulators and hybrid type electrode with a combination [11].



Flow chart 2-1: Classification of supercapacitors

2.2.1 Electrochemical Double-Layer Capacitance (EDLC)

The electrical energy is stored by formation of the electrical double layer in an EDLC (known as Helmholtz double layer) at the electrode/electrolyte interface as physically via the reversible ion adsorption from the electrolyte onto the active materials of the electrodes with electrochemical stabilities and high specific surface area[7]. When an electrode is immersed in an electrolyte, the ions penetrate the porous electrode while charges on the electrode surface spontaneously rearrange themselves in a particular order and are accumulated in the double layer mainly by electrostatic forces without phase transformation in the electrode materials. The maximal charge density is accumulated at the distance of the outer Helmholtz plane, i.e. at the center of the electrostatically attracted solvated ions [5].

For the advantage of EDL mechanism, supercapacitors based on EDL can store much more energy because of the large interfacial area and the atomic range of charge separation distances but conventional capacitors store little by way of energy due to the limited charge storage areas and geometric constraints of the separation distance between the two charged plates [12-13]. According to Helmholtz [14], two layers of opposite charge form at the electrode/electrolyte interface and are separated by an atomic distance and ions at the electrode/electrolyte interface are displaced and

diffuse between the electrodes through the electrolyte. This results in the formation of an electrical double layer (about 5-10Å thick) [7] which consists of one layer on the electrode surface and the other layer in the electrolyte, shown in Fig. 2.2. The Helmholtz model was further developed in 1910 by Gouy [15] to introduce random thermal motion, which led him to consider a spatial distribution of the ionic charge in the electrolyte to account for the voltage dependence of the capacitance which is known now as diffused layer. In 1913, Chapman [16] mathematically modeled the diffused layer to explain the distribution of ions in the electrolyte.

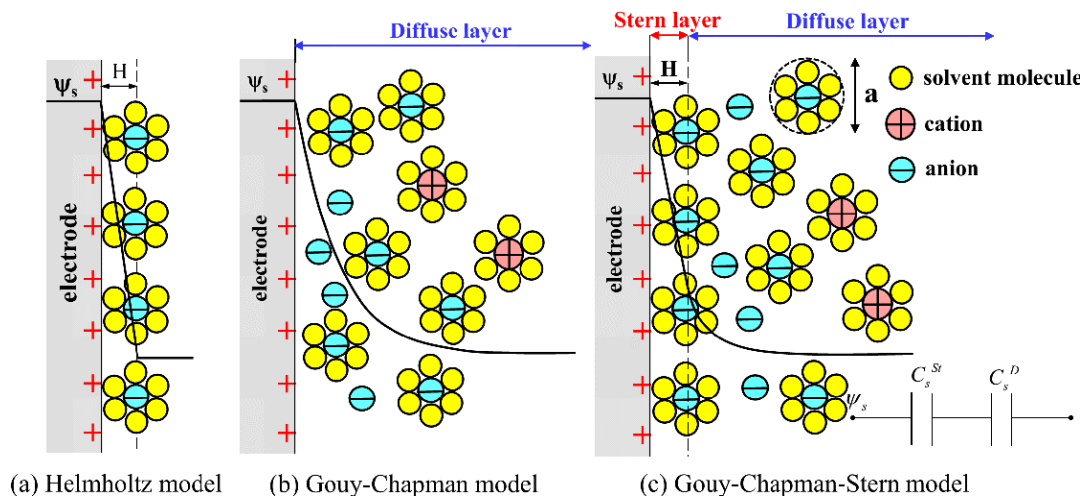


Figure 2.2: Schematic representation of electrical double layer structures according to (a) the Helmholtz model, (b) the Gouy-Chapman model, and (c) the Gouy-Chapman-Stern model. The double-layer distance in the Helmholtz model and the Stern layer thickness are denoted by H while ψ_s are the potential at the electrode surface [17].

Gouy had assumed earlier that the ions were point charges, hence a very large capacitance value would arise in the case of point charge ions close to the electrode surface. However, this same assumption led to the failure of the Gouy-Chapman model as it resulted in an overestimation of the overall capacitance of the electrodes due to an incorrect potential profile [17]. A combined model of the Helmholtz and Gouy-Chapman model was explained by Stern in 1924 to explicitly recognize two regions of ion distribution - the inner region called the compact layer or the Stern layer and the diffuse layer (as shown in Fig.2.2). In the compact layer, ions (very often hydrated) are strongly adsorbed by the electrode. In addition, the compact layer consists of specifically adsorbed ions (in most cases they are anions irrespective of the charged nature of the electrode) and non-specifically adsorbed counterions.

The inner Helmholtz plane (IHP) and outer Helmholtz plane (OHP) are used to distinguishing the two types of adsorbed ions. The diffuse layer region is what the Gouy–Chapman model defines [17]. The capacitance in the EDL (C_{dl}) can be treated as a combination of the capacitances from two regions, the Stern type of compact double layer capacitance (C_H) and the diffusion region capacitance (C_{diff}). Thus, C_{dl} can be expressed by the following Eq. 2.1

$$\frac{1}{C_{dl}} = \frac{1}{C_H} + \frac{1}{C_{diff}} \dots\dots\dots 2.1$$

Based on the charge storage mechanism, only the electrostatic surface charge plays an important role in storing the energy without any faradic reactions involved in EDLCs which ensure the facility of fast energy uptake and delivery to achieve a better power performance. As the supercapacitor electrodes can theoretically survive millions of cycles compared to a few thousand cycles compared to batteries which are due to the electrostatic charge storage mechanism (as shown in Fig. 2.3) eliminating volume expansion associated with charge-discharge processes in batteries and leading to more durable service life.

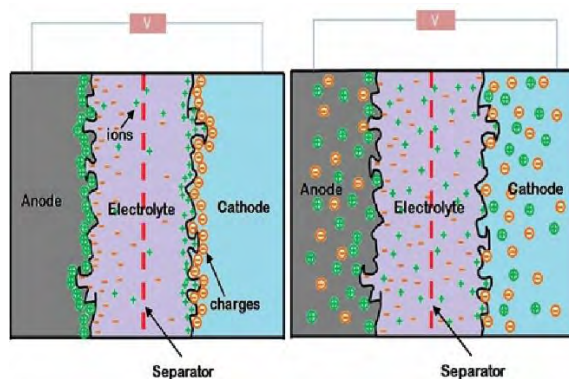


Figure 2.3: Schematic representation of a porous carbon EDLC in a charged (left) and discharged state (right) [18].

2.2.2 Pseudo-Capacitance

Electrode materials with pseudocapacitive behavior differ from the EDLC because redox reactions occurs at the surface or near the surface of electrode materials to accumulate specific capacitance which is similar to the behavior of batteries. Pseudocapacitance is accompanied by an electron charge-transfer between electrolyte

and electrode which involve one electron per charge unit. The term ‘pseudo’ originates from quick faradaic charge transfer reactions and not only from electrostatic charging. Conway identified several faradaic mechanisms that can result in capacitive electrochemical features: (1) underpotential deposition, (2) redox pseudocapacitance, and (3) intercalation pseudocapacitance [19]. These processes are illustrated in Fig. 2.4.

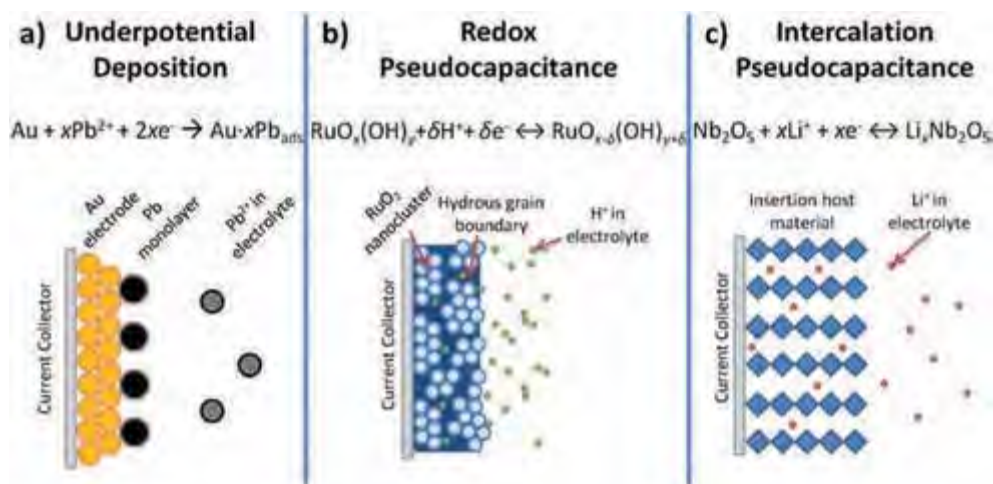


Figure 2.4: Different types of reversible redox mechanisms that give rise to pseudocapacitance: (a) underpotential deposition, (b) redox pseudocapacitance, and (c) intercalation pseudocapacitance[20].

Underpotential deposition occurs when metal ions form an adsorbed monolayer at a different metal's surface well above their redox potential. Redox pseudocapacitance occurs when ions are electrochemically adsorbed onto the surface or near the surface of a material with a concomitant faradaic charge-transfer. Intercalation pseudocapacitance occurs when ions intercalate into the tunnels or layers of a redox-active material accompanied by a faradaic charge-transfer with no crystallographic phase change [21-22]. Pseudocapacitance effects (electron sorption of H or metal atoms, redox reactions of electroactive species) strongly depend on the chemical affinity of carbon materials to the ion's sorbet on the electrode surface [19, 23]. Electrodes with pseudocapacitance are less dependent on the surface area and often deliver higher specific capacitance than regular carbon-based materials using a EDL charge storage mechanism. Although surface reactions offer higher capacitance and better electrochemical performance, they also cause the failure of electrode

stability during cycling. Ruthenium oxide (RuO_2) has been the focus of research attention for the past few decades as it has three distinct oxidation states below 1.2 V with high specific capacitance in acidic solutions by pseudocapacitive behavior [24] but till now more expensive. MnO_2 , Mn_3O_4 , Co_3O_4 , Fe_2O_3 , and NiO , have been investigated as replacements for RuO_2 for less expensiveness and benign properties but they never reach as high specific capacitance as RuO_2 does. Metal hydroxides [25-26] nitrides [27-30] and sulfides [31-34] are also pseudocapacitive materials, which deliver pseudocapacitance by surface redox reactions. Conducting polymers have also been tested as good supercapacitor electrode materials with pseudocapacitive behaviors, and they store charge by bulk processes through doping and undoping rapidly to high charge densities [35].

2.3 Electrode materials of supercapacitors

Based on the electric storage mechanisms and the nature of the electrode materials are three main categories of electro-active materials used in research to fabricate supercapacitors electrodes.

- ✓ carbon-based EDLC materials
- ✓ metal oxides / hydroxides / nitrides / sulfides
- ✓ conducting polymers.

The performance, cost and overall stability of the device is the key feature for the assortment of supercapacitors electrodes. Among the carbon-based materials, carbon nanotubes (CNTs) and graphene-based structures, which store charges based on non-Faradaic processes relying on their conducting nature and high specific surface area, have been extensively investigated [36-38]. By manipulating their structure and dimensions, their remarkable properties can be exploited for hydrogen storage, fuel cells, batteries and supercapacitors applications [39]. Expectedly, a wide variety of carbons have been investigated for possible applications in supercapacitor's technology. However, in this work, we will focus on graphene with 2D/3D architecture only.

2.3.1 Carbon-based EDLC materials- Graphene

2.3.1.1 What is graphene?

The term “graphene” was recommended by the relevant IUPAC commission to replace the older term “graphite layers” that was unsuitable in the research of a single carbon layer structure because a three-dimensionally (3D) stacking structure is identified as “graphite”. The recent definition of graphene can be given as a two-dimensional monolayer of carbon atoms, which is the basic building block of graphitic materials (i.e. fullerene, nanotube, graphite) [40]. Graphene, named by “graphite + ene”, is one of the allotropes (carbon nanotube, fullerene, diamond) of elemental carbon consisting of a one atomic thick planar monolayer sheet of sp^2 -bonded carbon atoms arranged in a two-dimensional (2D) honeycomb crystal lattice structure (Fig.2.5(a)). The thickness of graphene is only 0.34nm. Graphene is called the mother of all graphitic forms (Fig. 2.5 (b)) [30], can be used as building blocks for three-dimensional graphite (3D), one-dimensional (1D) carbon nanotube, until zero-dimensional (0D) fullerene [41].

In the excited state, the 2s, $2p_x$ and $2p_y$ orbitals of each carbon atom of graphene are hybridized together to form three degenerated sp^2 hybrid orbitals of equal energy and shape which forms three σ -bonds with three nearest neighbor sp^2 hybrid orbitals of carbon atoms in the basal plane of graphene by head-to-head overlap. The remaining unhybridized $2p_z$ orbital of each carbon of graphene which is oriented perpendicularly to the sp^2 hybrid orbital and contains the fourth valence electron overlap sidewise with the neighboring $2p_z$ orbital of another carbon of graphene to form delocalized π -bond, which is responsible for the electrical conductivity of graphene [42].

In brief, the pi orbital of one carbon atom in graphene molecules merges with adjacent pi orbitals of another carbon atom creating a huge orbital that allows an easy movement of electrons across the plane of the molecule. This is what gives graphene its remarkable electrical conductivity.

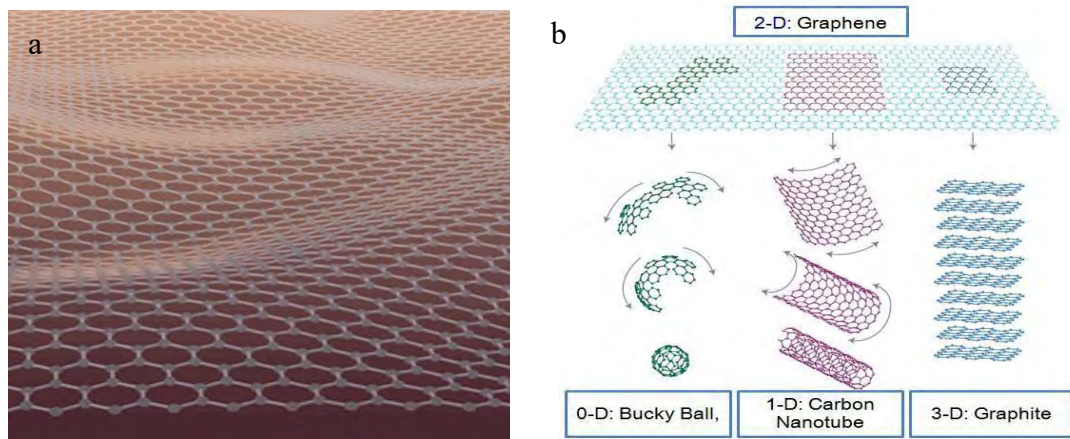


Figure 2.5: (a) Schematic of free-standing graphene, (b) Graphene: Mother of all graphitic forms: Buckyballs (Fullerene-0D); carbon nanotube (1D); graphite (3D)[42].

For the diversity of its allotropes and mass storage in nature, carbon becomes a fascinating candidate. Pioneer work starts from top-down processing method, trying to make the graphite thinner and thinner mechanically or chemically [43-44] Finally, in 2004, Andre Geim and Konstantin Novoselov at Manchester University isolated single-layer graphene successfully, by an unbelievable easy mechanical exfoliation method just using scotch tape[45] and received the Nobel Prize in Physics for their groundbreaking research on graphene: a two-dimensional material found in pencil [46].

It is really a milestone for graphene society, since then, researches on graphene spread out all over the world. Graphene has attracted interests from researchers who majored in physics, electrical engineer, material scientist, chemistry and even biology. The discovery of this allotrope has quickly overshadowed carbon nanotubes and activated carbons as electrode materials of choice for supercapacitors due to its exceptional thermal conductivity, outstanding mechanical strength, anomalous quantum Hall effect, and high specific surface area.

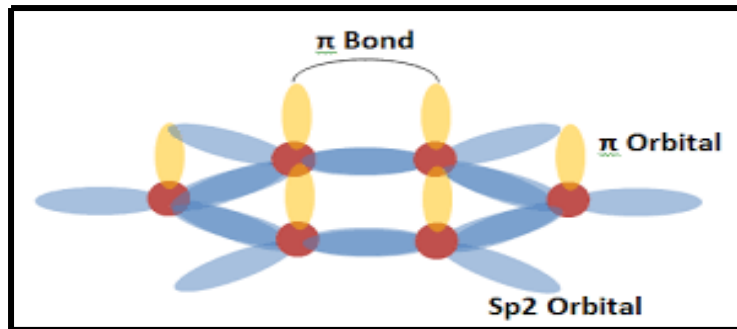


Figure 2.6: Schematic sp^2 hybridized C-C bond structure of graphene containing in-plane σ -bonds and perpendicular π -bonds.

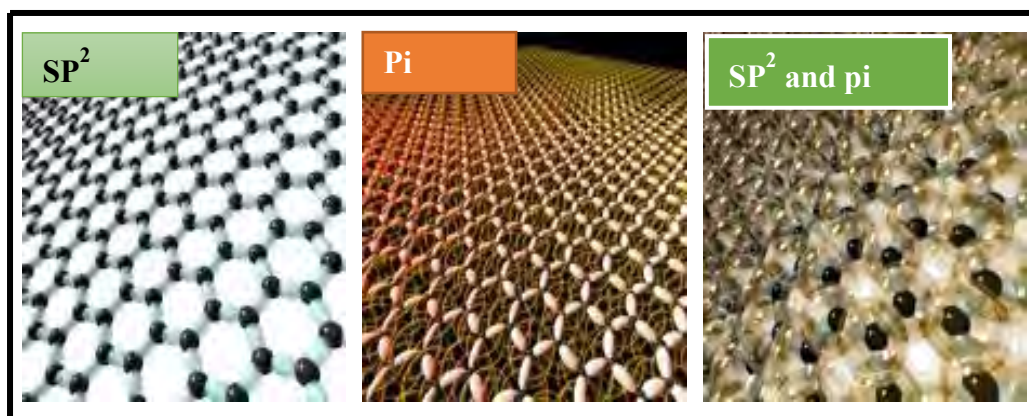


Figure 2.7: (a) Graphene molecule showing sp^2 bonds, (b) Graphene molecule showing pi orbitals and (c) Graphene molecule showing sp^2 and pi orbitals.

2.4 Graphene in supercapacitors

Graphene, a wonder materials-based electrode offers great potential for double-layer capacitors due to its exceptional physical and chemical properties such as the high conductivity of graphene makes it a material of choice with chemical and mechanical stability. Since it is a single layer, foldable material with a theoretical surface area of $2630 \text{ m}^2/\text{g}$, this makes it ideal for solar cell fabrication and energy storage devices, compared to the surface area of SWCNTs and graphite ($\sim 1315 \text{ m}^2/\text{g}$ and $10 \text{ m}^2/\text{g}$ respectively),[47-48] The use of graphene as an electrode material in storage devices is widely reported in fuel cell, lithium-ion battery, and supercapacitors(SCs) technologies. GO has been reported to possess a specific capacitance of $10\text{-}40 \text{ F/g}$ whilst rGO is more capacitive reaching as high as 205 F/g due to the increased conductivity of the rGO [49].

In separate work, Ruoff's group reported a chemically modified graphene produced with less functional groups from GO initially obtained from graphite. This was then modified using Hummer's method to obtain agglomerated chemically modified graphene which was then used to fabricate supercapacitors electrodes. Although the material was found to have a modest BET surface area of 705 m²/g, it still exhibited high capacitance values of 130 and 100 F/g in aqueous KOH and organic electrolytes respectively. These values were attributed to the large accessible surface area for electrical double layer charging [50]. Some other publication reported as modified GO with KOH activation of microwave exfoliated GO (MEGO) and thermally exfoliated GO (TEGO) to achieve higher specific surface area (up to 3100 m²/g) with a remarkable specific capacitance of 200 F/g in a two-electrode setup and the organic electrolyte was achieved for MEGO [36].

2.5 Metal oxide-based supercapacitors

Metal oxides with variable oxidation states in the preferred potential window and having a structural form of lattice that allows for protons to intercalate freely acts as pseudocapacitive electrode materials through faradaic reactions. RuO₂ is the prominent candidate of SCs which has the maximum theoretical capacitance 1450 F/g with a 1.0 V potential range, which is much larger than that of carbon materials[51-52]. At the Initial stage of metal oxide-based supercapacitors, hydrous ruthenium oxide (RuO_xH_y or RuO₂-xH₂O) with a specific capacitance as high as 720 F/g stands out as the best performer [51-56]. High operating potential window, variable oxidation states, highly reversible redox reactions, high proton conductivity, good thermal stability, long cycle life, metallic-type conductivity, and high rate capability is encouraged to the large-scale production of RuO₂ based SCs but the scarcity and high cost of ruthenium (Ru) limit us. However, boundless efforts have been dedicated to developing alternative cost-effective, environmentally friendly, multivalent states and earth-abundant transitions metal (Ni, Co, Mn, Fe, Mo, W, V, and Ti,) based electroactive as the form of hydroxides, oxides, sulfides, selenides and phosphide with various morphologies ranging from nanowhiskers, urchin-like, nanorods, crater-like microspheres and three-dimensional (3D) oval-shaped microparticles [57-61]. This nanomaterials was synthesized by collective techniques such as sonochemical and solvothermal [57], chemical precipitation[58], sol-gel processes [59], electrodeposition [60],

hydrothermal synthesis [61] and. Metal oxide with nanoscale dimensions has been widely favored for the increase of the surface area of the electrode from a range of 20 to 150 m^2/g while decreasing the transport/diffusion path lengths of ions [62] which are different from bulk. Due to high theoretical capacity (for MnO_2 about 1300 F/g) and natural abundance, low toxicity, variety of morphologies, environmental safety [63-65] of manganese oxides (MnO_x) with variable oxidation states of the manganese metal as the transitions between Mn (III)/Mn (II), Mn (IV)/Mn (III), and Mn (VI)/Mn (IV) within the electrode potential window are widely used as SCs materials instead of ruthenium oxide [66-75].

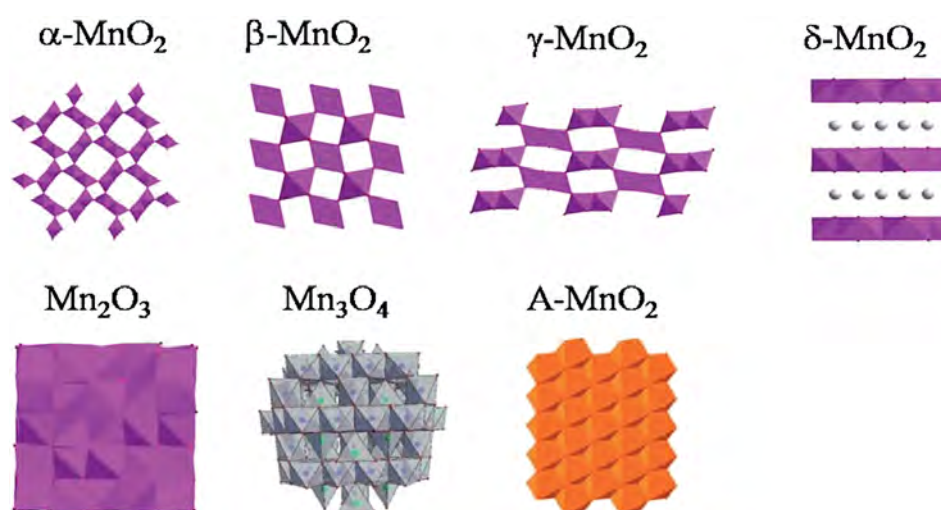


Figure 2.8: Crystal structures of manganese oxides with various oxidation states

MnO_x with several morphologies resulting from different synthesis methods have been reported such as nanowires[67], Nano rods[68], Nano belts[69-70], flower-like microspheres [71-72], and urchin-like Nano whiskers[73-74] as SCs . Depending on the morphology, the obtained material's specific surface area and electrochemical performance are considerably affected. As the charge storage process is conveyed by intercalation/de-intercalation of protons and alkali cations, only the structures with sufficient spaces for the diffusion of these ions are useful for SCs applications such as $\alpha\text{-MnO}_2$ has a large tunnel size (a. 0.46 nm) and birnessite-type $\delta\text{-MnO}_2$ has a large interlayer space (a. 0.7 nm), they exhibit great potential for SCs[68,75]. The crystal structures of manganese oxides [75] with various oxidation states are shown in Fig. 2.8.

Moreover, since only the surface thin layer of Mn-based materials can store charges, their charge storage ability is limited. To solve these problems, the nanostructured current collector was constructed to enhance the loading of the material. For example, Xu et al. prepared a vertically aligned Ni nanowire arrays matrix for MnO₂ with enlarged surface area significantly that improves the ohmic conductance of the matrix greatly compared with the conventional Ni foam substrate[76]. Also, Wang et. al. reported a solution-based approach to synthesize Mn₃O₄-graphene nanocomposites with a maximum capacitance of 236 F/g in 2 M NaOH [77]. Iron (Fe) oxides/oxyhydroxides are also reported as anode materials for SCs with the merits of high theoretical capacity, wide voltage window, material abundance, and low cost. Note that this type of material normally shows a surface pseudo-capacitance only in a relatively narrow voltage range of 0~-0.8 V vs Ag/AgCl and a battery behavior when the voltage window is broadened to the range of 0~-1.2 V vs Ag/AgCl or even lower voltage position. Nevertheless, most Fe based materials show poor rate stability and low cycle lifetime. This is probably due to the hydrogen evolution reaction occurring during the electrochemical process and fierce structure distortion which deteriorates the intrinsically fragile material structure [78]. Liu et al reported a technique of synthesize Fe₂O₃ nanodots which were well dispersed on N-doped graphene sheets. The small size of Fe₂O₃ and high electric conductivity of nitrogen-doped graphene benefit the full utilization of Fe₂O₃, leading to a high specific capacitance of 274 F/g at 1 A/g, excellent rate capability of 140 F/g at 50 A/g, and super long cycling stability of 100000 cycles with 75.3% capacitance retention [79].

2.6 Metal oxide/graphene composites

The hybrid and composite materials were studied to develop as SCs with high power density, energy density, long cycle life and good rate, capability by different research groups. From this point of views the highly pseudocapacitive metal oxides is fused with EDLC based carbon nanostructures with excellent stability and conductivity [8] with high surface area and favorable pore distribution, the pseudocapacitive material enhances the capacitance through faradaic reactions on the surface of the electrode [80]. Qian et al. synthesized graphene/MnO₂ composite by a polymer-assisted chemical reduction method in 2011 with high specific capacitance of 324 F/g and cycle stability in 1 M Na₂SO₄ electrolyte [81]. Yang et al. reported reduced graphene

nanosheet/urchin-like manganese dioxide (GNS/MnO₂) composite exhibits a maximum specific capacitance of 263 F/g with a capacity retention of about 99% after 500 cycles. Zaid et al. reported G/Ni nanocomposite with high specific capacitance 275 F/g at 2 A/g current density synthesized via ball mill process [82]. Zhang et al. reported in 2011 synthesized graphene/manganese dioxide (MnO₂) composite papers (GMCP) with the specific capacitance 256 F/g at a current density of 0.5 A/g with good cycle stability [83]. Peng et al. reported a facile method of hybrid nanostructure of quasi-2D ultrathin MnO₂/graphene nanosheets, showing high specific capacitances of 267 F/g at current density of 0.2 A/g and 208 F/g at 10 A/g with excellent rate capability with capacitance retention of 92% after 7000 charge/discharge cycles [84]. Ye et al. reported a facile method to prepare MnO₂/reduced graphene oxide (rGO) composites in 2013 as flexible solid-state SCs [85]. Huang et al. reported in 2015 MnO₂/graphene nanocomposite synthesized through a water-reflux condenser system that showed the specific capacitance as high as 350 F/g at 1A/g with ~ 93% specific capacitance retained after 5000 cycle [86]. Wen et al. a facile method to prepare the MnO₂-graphene composite in 2015 with a sandwich structure retained a capacity of 752 mAh/g at a current density of 100 mA/g after 65 cycles [86]. Sun et al. reported a green low-cost approach for the synthesis of 3D porous MnO₂/rGO/Ni composite foam via a solution chemical method in 2015 with higher capacitance of 479.0 F/g at 1.0 A/g with the capacitance retention of 83.5% after 1000 cycles [87]. Zhou et al. reported a method of MnO₂/GNS hybrid synthesis by one-pot electrochemical co-deposition in 2016 with a high specific capacitance of 413.1 F/g at A/g [88]. Sadak et al. reported a simple and cost-effective green method to produce free-standing, flexible, and highly conductive electrochemically exfoliated graphene paper (GrP) deposited nanoflower like manganese dioxide (MnO₂) electrochemically on GrP with an excellent capacitive performance with a high specific capacitance of 385.2 F/g at 1 mV/s and outstanding capacitance retention after 5000 cycles [89].

2.7 Nano-structuring of nanomaterials for supercapacitors

The nano-structuring of electrode materials influence surface area, electronic and ionic conductivity, and stability which is key criteria for designing a high-performance SCs electrode with high specific capacitance, large rate capability (related with capacitance retention at high scan rate or current density), and high cycle stability (related with Phase change, dissolution, and side reaction of active materials are the major reasons for causing cycle instability). Typically, nanomaterials with zero-dimensional (0D) i.e. more or less spherical in shape like fullerenes, quantum dots, nano- onions, nanoparticles, one dimensional (1D) i.e. nanotubes, nanofibers, nanowires, nanopillars, nanoribbons, and nanobelts., two dimensional (2D) i.e Graphene and many other layered Vander Waals solids like MoS_2 , CaGe_2 and CaSi_2 and three dimensional (3D) i.e. Mesoporous carbon and graphene aerogel & graphene spheres act as electrode materials for supercapacitors with excellent electrochemical properties[90-93]. Solid nanoparticles (nanospheres) are intensely investigated for designing supercapacitor electrodes. Carbon materials (e.g. activated carbon, carbon nanospheres and mesoporous carbon) [94] and transition metal oxides (e.g. MnO_2 , NiO , Fe_3O_4 , etc.) [94], have been widely fabricated into solid nanoparticles for electrode materials. Chen et al. was fabricated nanoporous metal/oxide (Au/MnO_2) hybrid supercapacitors electrodes and found a high specific capacitance of ~ 1145 F/g at 50 mV/s, which can be attributed to nanoporous gold that allows easy and efficient access to both electrons and ions [94]. Hollow 0D nanostructures have been recognized as promising candidates for electrode design due to their peculiar properties as low density, high surface-to-volume ratio and shortened pathways for transporting both mass and charges [95-96]. Yang et al. reported the synthesis of hollow carbon nanospheres by carbonizing its hollow nanosphere precursor obtained through a silica sphere-assisted hard templating method with a high surface area (1704 m^2/g), large bimodal mesopores (6.4 and 3.1 nm), and large pore volumes (1.6 cm^3/g) and was achieved specific capacitance of 251 F/g at 50 mV/s for the hollow carbon nanospheres [95]. Hollow 0D structures based on other electrode materials such as hollow double-shelled NiO , 612.5 F/g [97], etc. have been investigated as well.

The expedition for higher energy for SCs devices without any interpretation of power has led to a major effort in developing advanced electrode materials to complement or compete with batteries. Although 2D materials like graphene has great advantage of using for supercapacitor electrode materials its high conductivity and large surface area but they are composited with conducting polymer or transition metal oxides to improve the energy density of pristine graphene-based devices with improving high thermal stability and mechanical strength with minimum restacking of 2D layers, a considerable volume poses a major challenge. On the hands, hollow crumple conductive materials as templates and depositing pseudocapacitive materials like conductive polymers and metal oxide with a controlled pore size distribution is very attractive electrode materials to construct high performing supercapacitor electrodes. For boost up performance utilizing assemble of prefabricated nanostructures into 3D structures is another very important direction to obtain highly efficient supercapacitor electrodes. With the above motivation, graphene-based manganese oxide nanocomposite materials having a porous and crumple structure will intensively be studied in this present work. It is expected that the combination of these nanomaterials leads to a new generation of SCs electrodes with high energy and power densities in the near future. Compare to flat conductive materials as a template, crumpled ball or hollow conductive materials as a template or template with an active materials core with a controlled pore size distribution and depositing pseudocapacitive materials like metal oxide may significantly improve the scalability and performance of graphene-metal oxide-based electrode materials to construct high performing supercapacitor electrodes with high energy density

2.8 References

- [1] Poonam, Sharma, K., Arora, A. and S. K. Tripathi, “Review of supercapacitors: materials and devices” *Journal of Energy Storage.*, vol. 21, pp. 801–825, 2019.
- [2] Raza, W., Ali, F., Raza, N., Luo, Y., Kim, K. H., Yang, J., Kumar, S., Mehmood, A., Kwon, E., “Recent advancements in supercapacitor technology”, *Nano Energy.*, vol. 52, pp. 441–473, 2018.
- [3] Iro, Z. S., Subramani, C., and Dash, S. S., “A brief review on electrode materials for supercapacitor” , *Int. J. Electrochemical. Sc.*, vol. 11, pp. 10628–10643, 2016.
- [4] Wong, S. I., Sunarso, J., Wong, B. T., Lin, H., Yu, A., and Jia, B., “Towards enhanced energy density of graphene-based supercapacitors: Current status, approaches, and future directions” , *Journal of Power Sources.*, vol. 396, pp. 182–206, 2018.
- [5] Winter, M., and Brodd, R. J., “What are batteries, fuel cells, and supercapacitors?” , *Chem. Rev.*, vol. 104(10), pp. 4245–4269, 2004.
- [6] Frackowiak, E., and Béguin, F., “Carbon materials for the electrochemical storage of energy in capacitors,” *Carbon.*, Vol. 39(6), pp. 937-950, 2001.
- [7] Kötz, R., and Carlen, M., “Principles and applications of electrochemical capacitors”, *Electrochim. Acta.*, 2000.
- [8] Zhi, M., Xiang, C., Li , J., Li, M., and Wu, N., “Nanostructured carbon-metal oxide composite electrodes for supercapacitors: A review”, *Nanoscale.*, Vol. 5(1), pp. 72-88, 2013.
- [9] Li, B., Zheng, J., Zhang, H., Jin, L., Yang, D., Lv, H., Zhang, C., “Electrode materials, electrolytes, and challenges in nonaqueous lithium-ion capacitors”, *Advanced Materials.*, vol. 30(17), pp.1705670, 2018.
- [10] Choudhury, N. A., Sampath, S., and Shukla, A. K., “Hydrogel-polymer electrolytes for electrochemical capacitors: An overview”, *J. Chem. Sci.*, Vol. 121(5), pp. 727–734, 2009.
- [11] Muzaffar, A., Ahamed, M. B., Deshmukh, K., and Thirumalai, J., “A review on recent advances in hybrid supercapacitors: Design, fabrication and applications”, *Renew. Sustain. Energy Rev.*, vol. 101, pp. 123–145, 2019.
- [12] Borenstein, A., Hanna, O., Attias, R., Luski, S., Brousse, T., and Aurbach, D., “Carbon-based composite materials for supercapacitor electrodes: A review” , *J. Mater. Chem. A.*, vol. 5(25), pp. 12653–12672, 2017.

- [13] Ramachandran, R., Chen, S. M., and Gnana kumar, G., “An overview of electrochemical energy storage devices of various electrodes and morphological studies of supercapacitors” , *Int. J. Electrochem. Sci.*, vol. 10(12) , pp. 10355–10388, 2015.
- [14] Helmholtz, H., “Studien über electrische grenzsichten”, *Ann. Phys.*, vol. 243(7), pp. 337–382, 1879.
- [15] Gouy, M., “Sur la constitution de la charge électrique à la surface d’un électrolyte”, *J. Phys. Théorique Appliquée.*, vol. 9(1), pp. 457–468, 1910.
- [16] Stern, O., “Zur Theorie der Elektrolytischen Doppelschicht”, *Zeitschrift für Elektrochemie.*, vol. 30, pp. 508–516, 1924.
- [17] Pilon, L., Wang, H., and A. D’Entremont, “Recent advances in continuum modeling of interfacial and transport phenomena in electric double layer capacitors,” *Journal of the Electrochemical Society.*, vol. 162,(5). pp. A5158-5178, 2015.
- [18] Wu, X. L., and Xu, A. W., “Carbonaceous hydrogels and aerogels for supercapacitors”, *J. Mater. Chem. A.*, vol. 2(14), pp. 4852–4864, 2014.
- [19] Conway, B. E., “Electrochemical Supercapacitors: Scientific, Fundamentals and Technological Applications”, *Springer-Verlag New York Inc.*, United States, 1999.
- [20] Augustyn, V., Simon, P., and Dunn, B., “Pseudocapacitive oxide materials for high-rate electrochemical energy storage” , *Energy Environ. Sci.*, vol. 7, pp. 1597-1614, 2014.
- [21] Herrero, E., Buller, L. J., and Abruña, H. D., “Underpotential deposition at single crystal surfaces of Au, Pt, Ag and other materials”, *Chemical Reviews*, vol. 101(7). pp. 1897–1930, 2001.
- [22] Conway, B. E., “Two-dimensional and quasi-two-dimensional isotherms for Li intercalation and upd processes at surfaces”, *Electrochim. Acta*, vol. 38(9), pp. 1249–1258, 1993.
- [23] Conway, B. E., “Transition from ‘Supercapacitor’ to ‘Battery’ behavior in electrochemical energy storage,” *J. Electrochem. Soc.*, vol. 138(6), pp. 1539–1548, 1991.
- [24] Conway, B. E., “Electrochemical Supercapacitors: Scientific, Fundamentals and Technological Applications”. *Springer-Verlag New York Inc.*, United States, 1999.

- [25] Gupta, V., Kusahara, T., Toyama, H., Gupta, S., and Miura, N. "Potentiostatically deposited nanostructured α -Co(OH)₂: A high performance electrode material for redox-capacitors", *Electrochem. commun.*, vol. 9(9), pp. 2315–2319, 2007.
- [26] Zhao, D. D., Bao, S. J., Zhou, S. J., and Li, H. L., "Preparation of hexagonal nanoporous nickel hydroxide film and its application for electrochemical capacitor", *Electrochem. commun.*, vol. 9(5), pp. 869–874, 2007.
- [27] Choi, D., Blomgren, G. E., and Kumta, P. N., "Fast and reversible surface redox reaction in nanocrystalline vanadium nitride supercapacitors", *Adv. Mater.*, vol. 18(9), pp. 1178–1182, 2006.
- [28] Zhou, X., Chen, H., Shu, D., He, C., and Nan, J., "Study on the electrochemical behavior of vanadium nitride as a promising supercapacitor material", *J. Phys. Chem. Solids.*, vol. 70(2), pp. 495–500, 2009.
- [29] Perera, S. D., Rudolph, M., Mariano, R. G., Nijem, N., Ferraris, J. P., Chabal, Y. J., and Balkus, K. J., "Manganese oxide nanorod-graphene/vanadium oxide nanowire-graphene binder-free paper electrodes for metal oxide hybrid supercapacitors", *Nano Energy.*, vol. 2(5), pp. 966–975, 2013.
- [30] Hanumantha, P. J., Datta, M. K., Hong, K. S., Chung D. H., Tam. S. J., Poston, M. C., James A. Manivannan, A., and Kumta, P. N., "A simple low temperature synthesis of nanostructured vanadium nitride for supercapacitor applications", *J. Electrochem. Soc.*, vol. 160(11), 2013.
- [31] Yang, Z., Chen, C. Y., and Chang, H. T., "Supercapacitors incorporating hollow cobalt sulfide hexagonal nanosheets", *J. Power Sources.*, vol. 196(18), pp. 7874–7877, 2011.
- [32] Yang, Z., Chen, C. Y., and Chang, H. T., "Preparation of highly electroactive cobalt sulfide coreshell nanosheets as counter electrodes for CdZnSSe nanostructure-sensitized solar cells", *Sol. Energy Mater. Sol. Cells.*, vol. 95(10), pp. 2867–2873, 2011.
- [33] Yuan, C. B., Gao, L., Su, L., Chen., and Zhang, X., "Electrochemically induced phase transformation and charge-storage mechanism of amorphous Co Sx nanoparticles prepared by interface-hydrothermal method," *J. Electrochem. Soc.*, vol. 156(3), 2009.

-
- [34] Bao, S. J., Li, C. M., Guo, C. X., and Qiao, Y., “Biomolecule-assisted synthesis of cobalt sulfide nanowires for application in supercapacitors”, *J. Power Sources.*, vol. 180(1), pp. 676–681, 2008.
- [35] Rudge, Davey A. J., Raistrick, I., Gottesfeld, S., and Ferraris, J. P., “Conducting polymers as active materials in electrochemical capacitors” *J. Power Sources.*, vol. 47(1–2), pp. 89–107, 1994.
- [36] Zhu, Y., Murali, S., Stoller, M. D., Ganesh, K. J., Cai, W., Ferreira, P. J., and Ruoff, R. S., “Carbon-based supercapacitors produced by activation of Graphene”, *Science.*, vol. 332(6037), pp. 1537–1541, 2011.
- [37] Chidembo, A. T., Ozoemena, K. I., Agboola, B. O., Gupta, V., Wildgoose, G. G., and Compton, R. G., “Nickel(ii) tetra-aminophthalocyanine modified MWCNTs as potential nanocomposite materials for the development of supercapacitors”, *Energy Environ. Sci.*, vol. 3(2), pp. 228–236, 2010.
- [38] El-Kady, M. F., Strong, V., Dubin, S., and Kaner, R. B., “Laser scribing of high-performance and flexible graphene-based electrochemical capacitors”, *Science.*, vol. 335(6074), pp. 1326–1330, 2012.
- [39] Reddy, A. L. M., Gowda, S. R., Shaijumon, M. M., and Ajayan, P. M., “Hybrid nanostructures for energy storage applications”, *Advanced Materials.*, vol. 24(37). pp. 5045–5064, 2012.
- [40] Singh, V., Joung, D., Zhai, L., Das, S., Khondaker, S. I., and Seal, S., “Graphene based materials: past, present and future”, *Prog. Mater. Sci.*, vol. 56(8), pp. 1178–1271, 2011.
- [41] Geim, A. K., and Novoselov, K. S., “The rise of graphene”, *Nat. Mater.*, vol. 6(3), pp. 183–191, 2007.
- [42] Allen, M. J., Tung, V. C., and Kaner, R. B., “Honeycomb carbon: A review of graphene”, *Chem. Rev.*, vol. 110(1), pp. 132–145, 2010.
- [43] Zhang, Y., Small, J. P., Pontius, W. V., and Kim, P., “Fabrication and electric-field-dependent transport measurements of mesoscopic graphite devices”, *Appl. Phys. Lett.*, vol. 86(7), pp. 1–3, 2005.
- [44] Viculis, L. H., Mack, J. J., and Kaner, R. B., “A chemical route to carbon nanoscrolls”. *Science.*, vol. 299(5611), pp. 1361, 2003.
- [45] Elmlund, H., Ercius, P., Yuk, J.M., Limmer, D.T., Chen, Q., Kim, K., Han, S.H., Weitz, D.A., Zettl, A.,, “Electric field effect in atomically thin carbon films supplementary”, *Science.*, vol. 5(1), pp. 1–12, 2004.
-

- [46] Eigler, S., and Hirsch, A., “Chemistry with graphene and graphene oxide - challenges for synthetic chemists”. *Angewandte Chemie – Int. Edition.*, vol. 53, pp. 7720-7738, 2014.
- [47] Pumera, M. “Graphene-based nanomaterials and their electrochemistry”. *Chemical Soc.*, vol. 39(11), pp. 4146–4157. 2010.
- [48] Dreyer, D. R., Park, S., Bielawski, C. W. and Ruoff, R. S. “The chemistry of graphene oxide”, *Chemical Soc.*, vol. 39, pp. 228–240, 2010.
- [49] Ratha, S., and Rout, C. S., “Supercapacitor electrodes based on layered tungsten disulfide-reduced graphene oxide hybrids synthesized by a facile hydrothermal method”, *ACS Applied Materials and Interfaces.*, vol. 5, pp.11427–11433, 2013.
- [50] Stoller, M. D., Park, S., Yanwu, Z., An, J., and Ruoff, R. S. “Graphene-Based ultracapacitors”, *Nano Letters.*, vol. 8, pp. 3498–3502, 2008.
- [51] Ramani, M., Haran, B. S., White, R. E., and Popov, B. N., “Synthesis and characterization of hydrous ruthenium oxide-carbon supercapacitors”, *J. Electrochem. Soc.*, vol. 148(4), pp. A374, 2001.
- [52] Wu, Z.S., Wang, D.W., Ren, W., Zhao, J., Zhou, G., Li, F., and Cheng, H.M., “Anchoring hydrous RuO₂ on graphene sheets for high-performance electrochemical capacitors”, *Advanced Functional Materials.*, vol. 20, pp. 3595–3602, 2010.
- [53] Min, M., MacHida, K., Jang, J. H., and Naoi, K., “Hydrous RuO₂/carbon black nanocomposites with 3D porous structure by novel incipient wetness method for supercapacitors”, *J. Electrochem. Soc.*, vol. 153(2), pp. A334, 2006.
- [54] Ozolinš, V., Zhou, F., and Asta, M., “Ruthenia-based electrochemical supercapacitors: Insights from first-principles calculations”, *Acc. Chem. Res.*, vol. 46, pp. 1084–1093, 2013.
- [55] Soudan, P., Gaudet, J., Guay, D., Bélanger, D., and Schulz, R., “Electrochemical properties of ruthenium-based nanocrystalline materials as electrodes for supercapacitors”, *Chem. Mater.*, vol. 14, pp. 1210–1215, 2002.
- [56] Patake, V. D., Pawar, S. M., V. R. Shinde, T. P. Gujar, and C. D. Lokhande, “The growth mechanism and supercapacitor study of anodically deposited amorphous ruthenium oxide films”, *Curr. Appl. Phys.*, vol. 10, pp. 99–103, 2010.

- [57] Prabakaran, S. R. S., Nathan, T., and Cloke, M., “Electrode properties of Mn_2O_3 nanospheres synthesized by combined sonochemical/solvothermal method for use in electrochemical capacitors”, *J. Nanomater.*, vol. 2008, pp.7-15 2008.
- [58] Toupin, M., Brousse, T., and Bélanger, D., “Influence of microstructure on the charge storage properties of chemically synthesized manganese dioxide”, *Chem. Mater.*, vol. 14 (9), pp. 3946–52, 2002.
- [59] Reddy, R. N., and Reddy, R. G., “Sol-gel MnO_2 as an electrode material for electrochemical capacitors”, *J. Power Sources.*, vol. 124 (1) pp. 330–37, 2003.
- [60] Chen, Y. C., Hsu, Y. K., Lin, Y. G., Lin, Y. K., Horng, Y. Y., Chen, L. C., and Chen, K. H., “Highly flexible supercapacitors with manganese oxide nanosheet/carbon cloth electrode”, *Electrochim. Acta.*, vol. 56(20), pp. 7124–7130, 2011.
- [61] Yang, S., Liu, L., Wang, G., Li, D., Deng, and Qu, L., “One-pot synthesis of Mn_3O_4 nanoparticles decorated with nitrogen-doped reduced graphene oxide for sensitive nonenzymatic glucose sensing”, *J. Electroanal. Chem.*, vol. 755, pp. 15–21, 2015.
- [62] Zhu, T., Chen, J. S., and Lou, X. W., “Shape-controlled synthesis of porous Co_3O_4 nanostructures for application in supercapacitors”, *J. Mater. Chem.*, vol. 20(33), pp. 7015–7020, 2010.
- [63] Sawangphruk, M., Srimuk, P., Chiochan, P., Krittayavathananon, A., Luanwuthi, S., and Limtrakul, J., “High-performance supercapacitor of manganese oxide/reduced graphene oxide nanocomposite coated on flexible carbon fiber paper”, *Carbon.*, vol. 60, pp.109–116, 2013.
- [64] Kim, M., Hwang, Y., and Kim, J., “Graphene/ MnO_2 -based composites reduced via different chemical agents for supercapacitors”, *J. Power Sources.*, vol. 239, pp. 225–233, 2013.
- [65] Zhang, J., Jiang, J., and Zhao, X. S., “Synthesis and capacitive properties of manganese oxide nanosheets dispersed on functionalized graphene sheets”, *J. Phys. Chem. C.*, vol. 115(14), pp. 6448–6454, 2011.
- [66] Taguchi, S. A., Inoue, Akamaru, S., Hara, M., Watanabe, K., and Abe, T., “Phase transition and electrochemical capacitance of mechanically treated manganese oxides”, *J. Alloys Compd.*, 2006.

- [67] Wu, Z. S., Ren, W., Wang, D. W., Li, F., Liu, B., and Cheng, H. M., “High-energy MnO₂ nanowire/graphene and graphene asymmetric electrochemical capacitors”, *ACS Nano.*, vol. 4, pp. 5835, 2010.
- [68] Wang, G., Zhang, L., and Zhang, J., “A review of electrode materials for electrochemical supercapacitors”, *Chemical Soc. Rev.* vol., 41, pp.797-828, 2012.
- [69] Tang, X., Li, H., Liu, Z. H., Yang, Z., and Wang, Z., “Preparation and capacitive property of manganese oxide nanobelt bundles with birnessite-type structure”, *J. Power Sources.*, vol. 196(2), pp. 855–859, 2011.
- [70] Kang, L., Jiang, Y., Tang, M. Yang, and Z. Liu, “Electrochemical property of manganese oxide nanobelt bundles with layered structure,” *Chinese J. Chem.*, vol. 30(2), pp. 299–302, 2012.
- [71] Tang, X., Liu, Z. huai., Zhang, C., Yang, Z., and Wang, Z., “Synthesis and capacitive property of hierarchical hollow manganese oxide nanospheres with large specific surface area”, *J. Power Sources.*, vol. 193(2), pp. 939–943, 2009.
- [72] Donne, S. W., Hollenkamp, A. F., and Jones, B. C., “Structure, morphology and electrochemical behaviour of manganese oxides prepared by controlled decomposition of permanganate”, *J. Power Sources.*, vol. 195(1), pp. 367–373. 2010.
- [73] Yang, W., Gao, Z., Wang, J., Wang, B., Liu, Q., Li, Z., Mann, T., Yang, P., Zhang, M., and Liu, L., “Synthesis of reduced graphene nanosheet/urchin-like manganese dioxide composite and high performance as supercapacitor electrode”, *Electrochim. Acta.*, vol. 69, pp. 112–119, 2012.
- [74] Chidembo, A. T., Aboutaleb, S. H., Konstantinov, K., Jafta, C. J., Liu, H. K., and Ozoemena, K. I., “In situ engineering of urchin-like reduced graphene oxide-Mn₂O₃-Mn₃O₄ nanostructures for supercapacitors”, *RSC Adv.*, vol. 4(2), pp. 886-892, 2014.
- [75] Liu, Y., Wei, J., Tian, Y., and Yan, S., “The structure-property relationship of manganese oxides: highly efficient removal of methyl orange from aqueous solution”, *J. Mater. Chem. A.*, vol. 3(37), pp. 19000–19010, 2015.
- [76] Miller, E. E., Hua, Y., and Tezel, F. H., “Materials for energy storage: review of electrode materials and methods of increasing capacitance for supercapacitors”, *Journal of Energy Storage.*, vol. 20, pp. 30–40, 2018.

- [77] Wang, D., Li, Y., Wang, Q., and Wang, T., “Facile synthesis of porous Mn₃O₄ nanocrystal-graphene nanocomposites for electrochemical supercapacitors”, *Eur. J. Inorg. Chem.*, vol. 87, pp. 801-808, 2012.
- [78] Wang, F., Zeng, Y., Zheng, D., Li, C., Liu, P., Lu, X., & Tong, Y., “Three-dimensional iron oxyhydroxide/reduced graphene oxide composites as advanced electrode for electrochemical energy storage”, *carbon.*, vol. 03, 56–62, 2016.
- [79] Liu, L., Lang, J., Zhang, P., Hu, B., and Yan, X., “Facile synthesis of Fe₂O₃ nano-dots@Nitrogen-doped graphene for supercapacitor electrode with ultralong cycle life in KOH Electrolyte”, *ACS Appl. Mater. Interfaces.*, vol. 8(14), pp. 9335-9344, 2016.
- [80] An, K. H., Jeon, K. K., Heo, J. K., Lim, S. C., Bae, D. J., and Lee, Y. H., “High-capacitance supercapacitor using a nanocomposite electrode of single-walled carbon nanotube and polypyrrole”, *J. Electrochem. Soc.*, vol. 149(8), 2002.
- [81] Qian, Y., Lu, S., and Gao, F., “Preparation of MnO₂/graphene composite as electrode material for supercapacitors”, *J. Mater. Sci.*, vol. 46(10), pp. 3517–3522, 2011.
- [82] Akmal, N., Zaid, M., and Idris, N. H., “Enhanced capacitance of hybrid layered graphene / nickel nanocomposite for supercapacitors”, *Nat. Publ. Gr.*, vol. 6 pp. 1–8, 2016.
- [83] Zhang, Y., Su, M., Ge, L., Ge, S., Yu, J., and Song, X., “Synthesis and characterization of graphene nanosheets attached to spiky MnO₂ nanospheres and its application in ultrasensitive immunoassay”, *Carbon.*, vol. 57, pp. 22–33, 2013.
- [84] Peng, L., Peng, X., Liu, B., Wu, C., Xie, Y., and Yu, G., “Ultrathin two-dimensional MnO₂/graphene hybrid nanostructures for high-performance, flexible planar supercapacitors”, *Nano Lett.*, vol. 13(5), pp. 2151–2157, 2013.
- [85] Ye, K. H., Liu, Z. Q., Xu, C. W., Li, N., Chen, Y. B., and Su, Y. Z., “MnO₂/reduced graphene oxide composite as high-performance electrode for flexible supercapacitors”, *Inorg. Chem. Commun.*, vol. 30, pp. 1–4, 2013.
- [86] Wen, K., Chen, G., Jiang, F., Zhou, X., and Yang, J., “A facile approach for preparing MnO₂-graphene composite as anode material for lithium-ion batteries”, *Int. J. Electrochem. Sci.*, vol. 10(5), pp. 3859–3866, 2014.

- [87] Sun, Y., Zhang, W., Li, D., Gao, L., Hou, C., Zhang, Y., and Liu, Y., “Facile synthesis of MnO₂/rGO/Ni composite foam with excellent pseudocapacitive behavior for supercapacitors”, *J. Alloys Compd.*, vol. 649, pp. 579–584, 2015.
- [88] Zhou, H. and Zhai, H. J., “Rapid preparation of the hybrid of MnO₂ dispersed on graphene nanosheets with enhanced supercapacitive performance”, *Electrochim. Acta.*, vol. 215, pp. 339–345, 2016.
- [89] Sadak, O., Wang, W., Guan, J., Sundramoorthy, A. K., and Gunasekaran, S., “MnO₂ nanoflowers deposited on graphene paper as electrode materials for supercapacitors”, *ACS Appl. Nano Mater.*, vol. 2(7), pp. 4386-4394, 2019.
- [90] Gleiter, H., “Nanostructured materials: basic concepts and microstructure”, *Acta Mater.*, vol. 48(1) pp. 1-29, 2000.
- [91] Pokropivny, V. V., and Skorokhod, V. V., “Classification of nanostructures by dimensionality and concept of surface forms engineering in nanomaterial science”, *Mater. Sci. Eng. C.*, vol.27, pp.990-993, 2007.
- [92] Khan, I., Saeed, K., and Khan, I., “Nanoparticles: properties, applications and toxicities”, *Arabian Journal of Chemistry.*, vol. 12, pp. 908–931 2019.
- [93] Tiwari, J. N., Tiwari, R. N., and Kim, K. S., “Zero-dimensional, one-dimensional, two-dimensional and three-dimensional nanostructured materials for advanced electrochemical energy devices”, *Progress in Materials Science.*, vol. 57, pp. 724–803, 2012.
- [94] Yu, Z., Tetard, L., Zhai, L., and Thomas, J., “Supercapacitor electrode materials: Nanostructures from 0 to 3 dimensions”, *Energy and Environmental Science.*, vol. 8(3). pp. 702–730, 2015.
- [95] You, B., Yang, J., Sun, Y., and Su, Q., “Easy synthesis of hollow core, bimodal mesoporous shell carbon nanospheres and their application in supercapacitor”, *Chem. Commun.*, vol. 47(45), pp.12364-12366, 2011.
- [96] Liu, J., Wang, X., Gao, Zhang, Y., Lu, Q., and Liu., “Hollow porous carbon spheres with hierarchical nanoarchitecture for application of the high performance supercapacitors,” *Electrochim. Acta.*, vol. 11 pp. 183-192, 2016.
- [97] Zhang, Z., Gao, Q., Gao, H., Shi, Z., Wu, J., Zhi, M., and Hong, Z., “Nickel oxide aerogel for high performance supercapacitor electrodes”, *RSC Adv.*, vol. 6(113), pp.112620-112624, 2016.

Chapter-3

Characterization Techniques

3 Characterization Techniques

3.1 Fourier Transform Infrared Spectrometry

Fourier Transform Infrared Spectrometry (FTIR) is one of the most common and widely used spectroscopic techniques employed in identifying the functional group present in a molecule. It is based upon characteristic absorption of infrared radiation (IR) of molecules, which is a plot of measured intensity versus wavenumber of IR for a solid, liquid or gas sample.

IR involves the energy region of electromagnetic radiation (EMR) corresponding to wavenumber of $14000 \sim 4 \text{ cm}^{-1}$ which are classified into near-infrared region ($14000 \sim 4000 \text{ cm}^{-1}$), mid-infrared region ($4000 \sim 400 \text{ cm}^{-1}$) and far-infrared region ($400 \sim 4 \text{ cm}^{-1}$). In FTIR mainly mid-infrared region is employed because most of functional groups and bonds in organic and inorganic materials is absorbed radiation within this region. IR active molecules, only those which have a dipole moment that changes as a function of time, are able to interact with IR

The photo image of the instrument is shown in Fig. 3.1



Figure 3.1: A digital image of Shimadzu-FTIR-8400 FTIR machine.

Some molecules have a different structure but same bonding nature at different chemical environment vibrate at different frequencies of IR and thus make it enable to distinguish them from FTIR. Various structural parameters including nature of the

bonds (single/double/triple), mass of the atoms constituting bond, nature of hybridization, mode of vibration, resonance, type of isotope, solvent, etc. may be affected FTIR. [1,2]

The most usual technique of sample preparation for FTIR involves mixing the finely ground solid sample with powdered KBr and pressing the mixture under high pressure. Under pressure, KBr melts and seals the compound into a matrix. The result is a KBr pellet which can be inserted into a holder into the spectrometer. This method is known as the mull technique. FTIR offers various advantages including high scan speed, high resolution, high sensitivity, a wide range of applications, a large amount of structural information, non-destructiveness [1,3].

3.2 X-Ray Diffraction Spectroscopy (XRD)

XRD is a powerful, reliable, versatile non-destructive analytical technique for the qualitative and quantitative analysis of the crystalline materials, in the form of powder or solid to determine the chemical composition, crystal phase and crystallographic structure of materials. In these techniques, X-rays are generated by a cathode ray tube, filtered to produce monochromatic radiation, collimated to concentrate, and directed toward the sample [4]. The constructive interference (and a diffracted ray) is produced by the interaction of the incident rays with the sample when conditions satisfy Bragg's Law which relates the wavelength of electromagnetic radiation to the diffraction angle and the lattice spacing in a crystalline sample. X-ray used in diffraction have wavelengths lying approximately in the range 0.5 to 2.5 Å [4]. All possible diffraction directions of the lattice are attained due to the random orientation of the powdered material by scanning the sample through a range of 2θ angles. As each mineral has a set of unique d-spacing, the conversion of the diffraction peaks to d -spacing allows identification of the mineral. The value of d -spacing is obtained from Bragg's law-

$$2d \sin \theta = n\lambda \dots\dots\dots 3.1$$

where " d " is interlayer spacing, " θ " is the x-ray angle of incidence (and of diffraction) measured with respect to the crystalline planes, " n " is an integer value and " λ " is the wavelength of the incident beam.

Typically, the identification is achieved by comparison of d -spacing with standard reference patterns in the Joint Committee on Powder Diffraction Standards (JCPDS) database. XRD offers detailed information about the lattice parameter, lattice defects, lattice strain, crystallite size (in case of nanoparticles) and the type of molecular bond of the crystalline phase. Crystallite size of crystals are calculated from Scherrer formula

$$D = \frac{k\lambda}{\beta \cos \theta} \dots\dots\dots 3.2$$

where “ D ” is the crystallite size, k is a dimensionless shape factor (typical value 0.9), “ λ ” is the x-ray wavelength, “ β ” is the line broadening at halfway of the maximum intensity (FWHM) and θ is the Bragg angle (in degrees) [5,6]. Fig. 3.2 shows the PANALYTICAL EMPYREAN X-ray Diffractometer.



Figure 3.2 PANALYTICAL EMPYREAN X-ray Diffractometer.

3.3 Field Emission Scanning Electron Microscope (FESEM)

FESEM (Field Emission Scanning Electron Microscope), is a powerful modern technique for the characterization of materials, revealing external morphology (texture), crystalline structure and orientation of materials making up the sample [7,8]. Field Emission Gun (FEG) is used instead of Thermionic Emission Gun (TEG) as an electron emitter gun in the FESEM technique. A focused beam of high-energy electrons is used to generate a variety of signals at the surface of solid specimens. Among the generated signals, secondary electrons are most valuable for showing morphology and topography

on samples and backscattered electrons are most valuable for illustrating contrasts in composition in multiphase samples (i.e. for rapid phase discrimination), are generally used for imaging materials. An SEM images a sample by scanning it in a raster scan pattern with the excited electron beam. In most cases, data are collected over a selected area of the surface of the materials, and a 2-dimensional black-white image is generated that displays spatial variations in these properties. Areas ranging from approximately 1 cm to 5 microns in width can be imaged in a scanning mode using conventional SEM techniques (magnification ranging from 20X to approximately 500000X, the spatial resolution of 50 to 100 nm). The system is computer interfaced and thus provides a recording of the surface images in the computer file for its use as a hard copy [9-11].

The FESEM systems employed in this work. Fig.3.3 shows a photo of the JSM-7600F (FE-SEM, Tokyo, Japan) system using in the Department of Glass and Ceramic Engineering, Bangladesh University of Engineering and Technology (BUET).



Figure 3.3 A photo of SEM JSM-7600F.

The mean particle size, length, diameter, etc. are calculated taking 10-15 measurements from SEM images using “ImageJ” (64-bit Java 1.8.0_112) software.

3.4 Energy Dispersive X-ray Spectroscopy (EDX)

EDX, is a microanalysis technique, used to identify the elemental composition and in chemical characterization of materials, are generally used in conjunction with Electron

Microscopy instruments such as SEM or TEM where the imaging capability of the microscope identifies the specimen of interest [12-14].

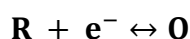
The electrons are ejected from the atoms of the sample comprising the sample's surface by the bombardment of the electron beam of SEM. As a result, electron vacancies are filled by electrons from a higher state, and an x-ray is emitted to balance the energy difference between the vacant and filled. These X-rays can be detected by a Si Li detector, calibrated with respect to cobalt metal emission (6.925 keV), and then used to identify and analyze the elemental composition and abundance of the specimen surface. The various emission lines associated with X-rays emitted from an atom are named after the shell of the initial vacancy, i.e. K, L, M, etc. A Greek letter subscript is used to indicate the shell of the electron that fills the gap [8,13,15]. With the help of supporting software, one can obtain a full elemental spectrum in only a few seconds using the “pot mode technique” and to readily identify peaks, which makes EDX a great survey tool to quickly identify unknown phases prior to quantitative analysis. EDX can also be used in semi-quantitative mode to determine chemical composition by a peak-height ratio relative to a standard. [12,16]

3.5 Investigation of electrochemical capacitive behavior

3.5.1 Cyclic voltammetry (CV)

CV is a powerful and widespread electro-analytical technique commonly employed to investigate the reduction and oxidation processes of molecular species based on the current response of a material as a function of potential. Nowadays these techniques are widely used to characterize the performance of various electrical energy storing devices such as supercapacitors [17-19]. In the CV experiment, the potential of the working electrode is scanned for a predetermined switching potential (known as scan window) with performing a forward and reverse scan. This gives a 'cyclic' sweep of potentials which can be repeated as per interest and a plot of the current vs. potential derived from the data is called a cyclic voltammogram. The initial current response is known as capacitive which originates from the electrical double layer (EDL) formed at electrode surface involving diffusion-controlled process as potential allowed to increase.

The anodic peak current and anodic potential are found when the potential approaches a specific value favoring the reduction of the active material, the current response increases rapidly resulting in an anodic peak and the corresponding current and potential are called anodic peak current and anodic potential. Then current falls off when the maximum rate of mass transfer has been reached and goes down only to reach equilibrium at some steady value. A similar but opposite peak current may be observed when potential meets a value favoring oxidation of the reduced species during its return tour to the initial value [20]



Faradic current which is a response from redox reaction while the remaining responses are usually attributed to EDL is called non-Faradic current. Thus, the capacitive window of a material can be easily identified from the absence or presence of a redox peak in its CV.

Scan rate is the rate of change of potential with time. The total current increase is directly proportional to scan rate which rationalized by considering the size of the diffusion layer and the time taken to record the scan. The magnitude of the current response and the shape of the voltammograms are highly dependent on analyte nature, concentration, scan rates, and experimental conditions. However, depending on the potential window and materials of interest, CV may appear to be slightly distorted in shape indicating the presence of the faradic process and charge storage in that potential window region by the faradic process is known as Pseudocapacitance. When a CV shows a rectangular shape, i.e. the charge storage and release processes to be capacitive. The capacitance calculated from the CV curve is based on the following formula [21]

$$C_{sp} = \frac{\int IdV}{2\vartheta m \nabla V} \dots\dots\dots 3.3$$

where “I” is the current (A), “ ∇V ” is the potential difference during the scan (V), ‘ ϑ ’ is the scan rate, and “m” is the mass of the active material in gram. “ $\int IdV$ ” is known as the integrated area of the CV curve.

3.5.2 Galvanostatic Charge Discharge (GCD)

GCD, also known as chronopotentiometry, is a reliable method to evaluate the electrochemical capacitance of materials under controlled current conditions which gives access to various parameters [22] such as,

- Capacitance,
- Resistance and
- Cyclability

In this technique, a current pulse (as current density) is applied to the working electrode and the resulting potential is measured against a reference electrode as a function of time. The measured potential is abruptly changing due to the IR (internal resistance) loss when current is applied and after that, it gradually changes because concentration over-potential is developed across the electrodes, as the concentration of the reactant is exhausted at the electrode surface. The following graphs are the current excitation signal and potential response as a function of time.

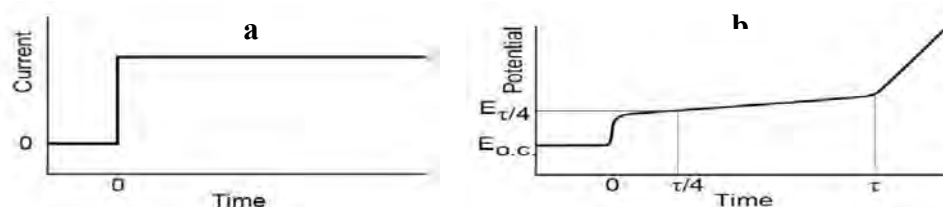


Figure 3.4 (a) Current excitation and (b) potential response in GCD.

It is possible to identify the nature of the electrode material from the GCD. e.g. the potential response of an ideal capacitive material in GCD shows discharge/ charge time to be ~ 1 and can be easily marked.

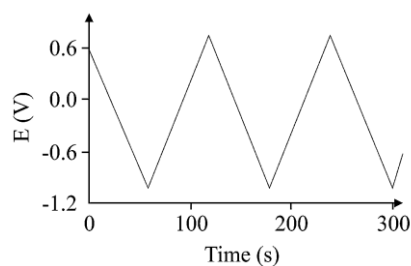


Figure 3.5 Potential response of an ideal electrochemical capacitor in GCD.

The specific capacitance of an electrochemical capacitor can be easily calculated from its potential response in GCD on the basis of the relationship [23]

$$C_{sp} = \frac{i\Delta t}{m\Delta V} = j \frac{\Delta t}{\Delta V} \dots \dots \dots (3.4)$$

where “ C_{sp} ” is the specific capacitance, “ I ” discharge current (cathodic current), “ m ” is the mass of active electrode material, “ Δt ” is the total time of discharge and “ ΔV ” is the potential drop during discharge. $\frac{\Delta v}{\Delta t} = \text{discharge slope}$

3.5.3 Electrochemical Impedance Spectroscopy(EIS)

EIS are carried out at different A.C. frequencies are used to find out the double-layer capacitance and for the characterization of electrode processes and complex interfaces. EIS is a technique that gives the direct connection between the real system and idealized equivalent circuit which comprises of discrete electrical components (R= resistance, C= capacitor, and L=inductor) in their series and parallel combination. Electrochemical capacitors are the real systems in which either blocking /polarizable electrodes (have either planar geometry or large surface area porous electrodes, in case of electrochemical double-layer capacitors) or electroactive electrode materials (in case of redox capacitors) are used [22].

Electrochemical impedance (Z) is the total effect of resistance or the measure of the opposition to the passage of the current when an AC voltage source is applied. However, in real circuit systems, i.e. RLC circuit, resistance (R) is accompanied by reactance (X) from capacitor (C) and the inductor (L), collectively known as impedance. Following Ohm’s law $V=IR$, we can write in that case, $V=IZ$, where impedance Z use the same unit ohm, as used by resistance [23]

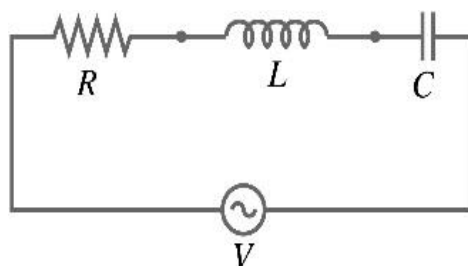


Figure 3.6 An R.L.C series circuit

Impedance data are commonly represented in two forms. One as the Nyquist plot, showing the variation of Z_{img} with Z_{real} and the other as Bode plot showing the frequency dependence of phase angle. Electrochemical processes involve various types of resistance originating from solution, charge transfer, electrical double layer (capacitor), diffusion, etc. and their equivalent circuit, commonly known as Randles circuit, can be drawn from EIS study. A Randles circuit is an equivalent electrical circuit that consists of an active electrolyte resistance R_s in series with the parallel combination of the double-layer capacitance C_{dl} and an impedance of a faradaic reaction.

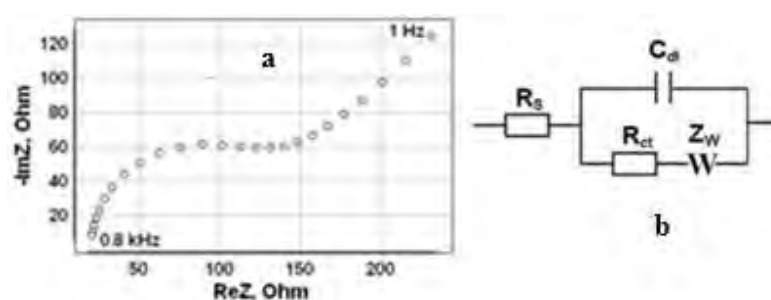


Figure 3.7(a) A typical Nyquist plot and (b) its equivalent circuit

EIS offers the chance of both diagnostic and application of electrochemical processes. With EIS, it is possible to identify the nature of an electroactive material. It has been applied in engineering, biosensor applications, etc.

3.5.4 Determination of energy density and power density

Energy density and power density are similar to energy and power, except that their values relate to volume. Energy density is the amount of energy that can be stored in a given mass of a substance or system or region of space per unit volume. The higher the energy density of a system or material, the greater the amount of energy stored in its mass. Having a high energy density does not give information on how quickly this energy can be used. This knowledge is contained in a substance's power density. Power density is the amount of power (time rate of energy transfer) per unit volume and is a measure of power output per unit volume. It describes the rate at which its energy can be put out. A high energy density does not necessarily mean a high-power density and in fact, having a high energy density may go along with a low power density. The energy density (E) and power density (P) values of the synthesized materials were

calculated from the known highest value of capacitance obtained either from CV or GCD curves using the following equations [24-26]:

$$E = 0.5 \times C_{sp} (\Delta V)^2 / 3.6 \dots\dots\dots(3.5)$$

$$P = E \times 3600 / \Delta t \quad \dots\dots\dots(3.6)$$

Where E is the energy density of the electrode (Wh/kg), P is the average power density (W/kg), C_{sp} is the specific capacitance of the active material (F/g), ΔV is the operating voltage range or potential window (V) and Δt is the discharge time (s) in GCD curve.

3.6 References

- [1] Kriz, G. S., Pavia, D. L., Lampman, G. M., “*Introduction to Spectroscopy*”, 5th ed. Stamford, USA: Cengage learning, 2000.
- [2] Stuart, B. H., “*Infrared Spectroscopy: Fundamentals and Applications*”, 2004.
- [3] Stuart, B. H., George, B., and McIntyre, P., “*Modern Infrared Spectroscopy*”, Wiley, 1996.
- [4] Dorset, D. L. “X-ray Diffraction: A Practical Approach”, *Microscopy and Microanalysis.*, vol. 4, pp. 513–515, 1998.
- [5] Bishnoi, A., Kumar, S., and Joshi, N. “Wide-Angle X-ray Diffraction (WXR D). In *Microscopy Methods in Nanomaterials Characterization*”, Elsevier., pp. 313–337, 2017.
- [6] Toraya, H., “Introduction to X-ray analysis using the diffraction method”, *Rigaku J.*, vol. 32(2), pp. 35–43, 2016.
- [7] Egerton, R. F., “*Physical Principles of Electron Microscopy: An Introduction to TEM, SEM, and AEM*”, Springer US, 2006.
- [8] Grundy, P. J., and Jones, G. A “*Electron microscopy in the study of materials*”, London : Edward Arnold, 1976.
- [9] Backer, H. C., “SCANNING ELECTRON MICROSCOPY.” *Lubrication* vol. 61, pp. 37–56, 1975.
- [10] Amer, Dr. M., “*Methods and materials*”, *Assiut Journal for Environmental Studies.*, vol. 2001.
- [11] Ul-Hamid, A., “ A Beginners’ Guide to Scanning Electron Microscopy. A Beginners’ Guide to Scanning Electron Microscopy”, *Springer International Publishing.*, pp. 1–25, 2018.
- [12] Ngo, P. D., “Energy Dispersive Spectroscopy”, *Fail. Anal. Integr. Circuits.*, pp. 205–215, 2012.
- [13] Ismail, A. F., Khulbe, K. C., and Matsuura, T., “ *RO Membrane Characterization*”, *Reverse Osmosis.*, pp 57-90, 2018.
- [14] Scimeca, M., Bischetti, S., Lamsira, H.K., Bonfiglio, R., and Bonanno, E. “Energy dispersive X-ray (EDX) microanalysis: A powerful tool in biomedical research and diagnosis”. *European Journal of Histochemistry.*, vol. 62, pp. 89–99, 2018.
- [15] Musić, S., Filipović-Vinceković, N., and Sekovanić, L., “Introduction to Energy Dispersive X-Ray Spectrometry (EDS)”, *UC Riverside.*, pp. 1–12, 2011.

- [16] *Energy-dispersive X-ray spectroscopy*, Wikipedia, the free encyclopedia, http://en.wikipedia.org/wiki/Energy-dispersive_X-ray_spectroscopy.
- [17] Zhang, J., Jiang, J., and Zhao, X. S., “Synthesis and capacitive properties of manganese oxide nanosheets dispersed on functionalized graphene sheets”, *J. Phys. Chem. C.*, vol. 115(14), pp. 6448–6454, 2011.
- [18] Wang, J., “*Analytical Electrochemistry*”, 2nd ed. John Wiley & Sons, Inc., New York, 2000.
- [19] Liu, Y. F., Yuan, G. H., Jiang, Z. H., and Yao, Z. P., “Solvothermal synthesis of Mn₃O₄ nanoparticle/graphene sheet composites and their supercapacitive properties”, *J. Nanomater.*, 2014.
- [20] Bard, L. R., A. J., and Faulkner., “*Electrochemical methods fundamentals of electrochemistry*”, 2nd ed. John Wiley & Sons, Inc., New York, 1994.
- [21] Wang, H., Gao, Q., and Hu, J., “Asymmetric capacitor based on superior porous Ni-Zn-Co oxide/hydroxide and carbon electrodes”, *J. Power Sources.*, vol. 195(9), pp. 3017–3024, 2010.
- [22] Zhao, X., Hou, Y., Wang, Y., Yang, L., Zhu, L., Cao, R., and Sha, Z. “Prepared MnO₂ with different crystal forms as electrode materials for supercapacitors: experimental research from hydrothermal crystallization process to electrochemical performances”, *RSC Adv.*, vol. 7(64), pp. 40286–40294, 2017.
- [23] Barsoukov, E. R., and Macdonald, J., “*Impedance spectroscopy-theory , experiment , and applications*”, 2nd ed. John Wiley & Sons, Inc., New Jersey., 2005.
- [24] González, A., Goikolea, E., Barrena, J. A. and Mysyk, R. “Review on supercapacitors: technologies and materials”, *Renew. and Sustain. En. Rev.*, vol. 58, pp. 1189–1206, 2016.
- [25] Winter, M., and Brodd, R. J., “What are batteries, fuel cells, and supercapacitors?”, *Chem. Rev.*, vol. 104, pp. 4245-4269, 2004.
- [26] Gao, Z., Wang, J., Li, Z., Yang, W., Wang, B., Hou, M., He, Y., Mann, T., Yang, P., Zhang, M., Liu, L., “Graphene nanosheet/Ni²⁺/Al³⁺ layered double-hydroxide composite as a novel electrode for a supercapacitor”, *Chem. Mater.*, vol. 23(15), pp. 3509-3516, 2011.

Chapter-4

Experimental

4 Experimental

4.1 Materials and instruments

All the chemicals and reagents used in this work were analytical grade and were used without further purification. All synthesis and washing of this work were performed using double distilled water.

The chemicals and reagents used in this work are listed below:

Name of chemicals and reagents	Source of collection
Sodium hydroxide	Sigma-Aldrich, Switzerland
Hydrogen peroxide	Scharlau, Spain
Sodium nitrate	Merck, Germany
Dimethyl sulfoxide	RCI Labscan, Thailand
Iron (III) nitrate nonahydrate	Sigma-Aldrich, Switzerland
Nickel chloride hexahydrate	Sigma-Aldrich, Switzerland
Ethylene glycol	Merck, Germany
H ₂ SO ₄	Merck, Germany
PVA	Merck, Germany
HCl	RCI Labscan, Thailand
Benzyl alcohol	Merck, Germany
Hydrazine hydrate	Merck, Germany

Synthesis and analysis of the samples were performed using the following instruments:

- Digital balance (CX 220, Citizon, USA and GH-252, AND, Japan)
- Hotplate with digital stirrer (CD 162, Stuart, UK)
- Centrifuge machine (Universal 16A, Hettich, Germany)
- Hot air oven (DSO-500D, Digi system, Taiwan)
- Agate mortar (125mm)
- Muffle furnace (LT 5/12, Nabertherm, Germany)

- pH meter (3510 pH meters, Jenway, UK)
- Ultrasonic bath (Powersonic 505, Hwashin, S. Korea)
- Fourier Transform Infrared Spectrophotometer (FTIR-8400, Shimadzu, Japan)
- X-ray diffractometer (Empyrean, Malvern Panalytical, UK)
- Field Emission Scanning Electron Microscope (FESEM)
- Potentiostat/Galvanostat HAB-151 (Hokuto Denko Ltd.)

4.2 Synthesis of materials

4.2.1 Synthesis of graphene oxide (GO) and reduced graphene oxide (rGO)

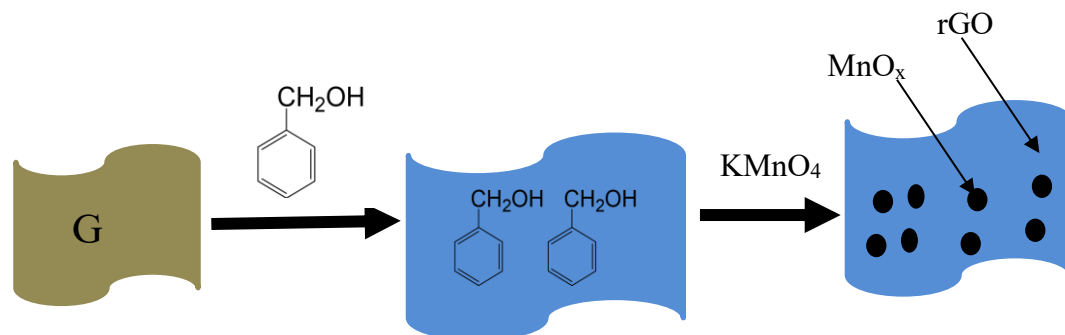
Graphene oxide was prepared from graphite powder (< 20 μm with purity >99.9 wt. %) following the modified Hummers method [1]. In detail, concentrated (98%) solution of H_2SO_4 (46 mL) was slowly added to a mixture of graphite powder (2.0 g), NaNO_3 (1.0 g) and KMnO_4 (6.0 g) in the round bottle flask on an ice bath and stirred for 30 min at temperature below 20 $^\circ\text{C}$. Then the mixture was transferred into the water bath removing the ice bath and was intensely stirred at ~ 35 $^\circ\text{C}$ for 1 h. After completing the reaction, 92 mL distilled water was added to the above mixture while maintaining the temperature at ~ 98 $^\circ\text{C}$ for 30 min, followed by reducing the temperature to ~ 60 $^\circ\text{C}$ with the addition of warm deionized water (280 mL) and H_2O_2 (30 wt%, 20 mL) while stirring continuously for a further 2 h. The mixture was subjected to high power sonication for 30 min and then filtrated to collect the solid product of GO and washed with 4 wt% HCl solution and distilled water several times until the solution was found to be free from chloride ion and the pH of the supernatant was neutral. The prepared solution of GO was preserved in a refrigerator for further use. A portion of GO was then dried in an oven at 60 $^\circ\text{C}$ for 12 h resulting in a thin brown sheet for further use in the preparation of composites.

Reduced graphene oxide (rGO) was prepared from GO by reduction with NH_3 and hydrazine solution [2]. A GO suspension prepared by ultrasonication of 360 mg of GO in 400 mL of water was reduced to a dispersion of graphene sheets by adding aqueous ammonia (5 mL, 25%) and hydrazine hydrate (5 mL) and heating in an oil bath at 95 $^\circ\text{C}$ for 2 hours. For better reduction of GO to rGO, Sodium borohydride (1.2 g) was added to the above reaction mixture and heating in an oil bath for 1 h. After the reaction,

the dispersed graphene was filtered and the collected solid was washed several times with deionized water and finally dried at 60 °C in a hot air oven.

4.2.2 Synthesis of rGO-MnO_x nanocomposite

The flowchart 4.1 shows the synthesis process for obtaining of MnO_x nanoparticles on the surface of rGO nanosheets



Flow chart 4-1: Synthesis process for obtaining of MnO_x nanoparticles on the surface of rGO nanosheets.

In brief, 100 μ L benzyl alcohol and then 200 mg rGO was added into 30 mL DI water under mild stirring condition. The hydrophobic benzyl alcohol was adsorbed on the surface of rGO through ultrasonic treatment for 30 min. 60 mg KMnO₄ was added into the above solution and kept on mild stirring for 10 h at 60°C [3]. The black precipitate was washed several times with distilled water and ethanol and dried 50°C at hot air oven for 12 hours.

4.2.3 Synthesis of Ni nanoparticles

The nickel nanoparticles were prepared through reducing nickel chloride by hydrazine hydrate according to the mass reduction process by forming complex [3]. In a typical experiment, the solutions were prepared by dissolving 0.025mol of NiCl₂.6H₂O (5.95 g of NiCl₂) in 10 mL of distilled water. 0.3 mol of 80% N₂H₄.H₂O (18.75 g of N₂H₄) was poured into the solution instantaneously with vigorous stirring, which resulted in a pale violet precipitate. The additional distilled water was added to wash the precipitate on the wall instantaneously. The temperature of the mixture was increased up to 65°C by the exothermic formation of a Ni complex between NiCl₂ and N₂H₄. When the

solution temperature became 50°C by cooling in an ambient atmosphere, 0.3 mol of a 50 wt.% NaOH solution (12 g of NaOH in 24 mL H₂O, the temperature of NaOH solution 20°C) was poured instantaneously into the above mixture. The solution temperature initially decreased to room temperature and then increased spontaneously up to the second maximum (~54 °C). The reaction was complete 1 h after the temperature reached the second maximum (~54 °C) [4,5]. The black Ni precipitate was washed with distilled water until pH 7 and ethanol respectively and dried at room temperature for 16 h under constant ventilation.

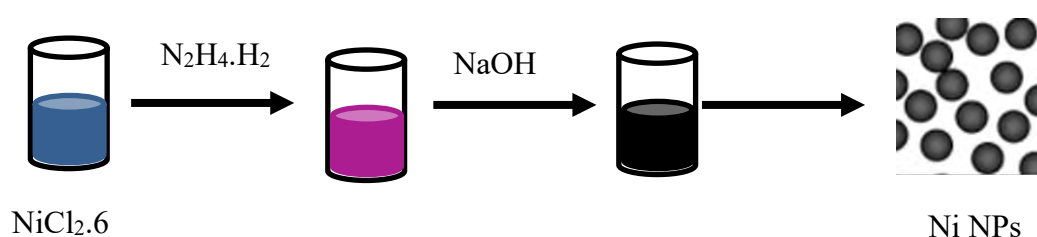


Figure 4.1: Schematic flowchart for the synthesis of Ni NPs

4.2.4 Synthesis of core-shell Ni@rGO nanostructure and coreless (--)@rGO hollow spheres

Ni@rGO core-shell nanostructure was synthesized from Ni NPs and Graphene Oxide (GO) by mixing weight ratio 5:1. Specifically, 400mg previously synthesized GO was added in 100ml distilled H₂O and 2 g of Ni NPs was added into 100ml EG and separately aided to sonicate for 1 h. The two solutions were then mixed together by sonication for 1 h and stirred for 24 hours obtained a blackish-brown gel. To obtained Ni@rGO core-shell nanostructure, the mixture was heated to 100 °C and 12 mL of hydrazine hydrate with 6 mL NH₄OH was added into the mixture and the reaction was kept going at 98 °C for 2 hours [2] and then 2 g of NaBH₄ was added [6] and stirred for another 1 hour to obtaining highly reduced graphene oxide core (Ni@rGO). The product was harvested by centrifugation and washed with deionized water and ethanol before drying in an oven overnight at 60 °C. The coreless (--)@rGO were obtained by dissolving the above prepared Ni@rGO core-shell spheres in a dilute hydrochloric acid solution for 48 h [7]. The complete removal of Ni NPs was confirmed by using the magnet.

4.2.5 Synthesis of core-shell Ni@rGO-MnO_x nanocomposite and coreless porous (--@rGO-MnO_x nanosphere

For the synthesis of Ni@rGO-MnO_x, 400 mg Ni@rGO was added into 100 mL DI water and 500 μL benzyl alcohol under mild stirring conditions. The hydrophobic benzyl alcohol was adsorbed on the surface of Ni@rGO through ultrasonic treatment for 30 min. 60 mg KMnO₄ was added into the above solution and kept on mild stirring for 12 h [3]. The obtained black precipitate was washed several times with distilled water and ethanol. Then the precipitate was dried 50 °C at hot air oven for 12 hours. For the synthesis of hollow (--@rGO-MnO₂, 400 mg hollow (--@rGO was added instead of Ni@rGO with all conditions remaining the same.

The following flowchart shows all pathways of synthesis of Ni@rGO, porous hollow (--@rGO, rGO-MnO_x, core-shell Ni@rGO-MnO_x nanocomposite and porous hollow (--@rGO-MnO_x,

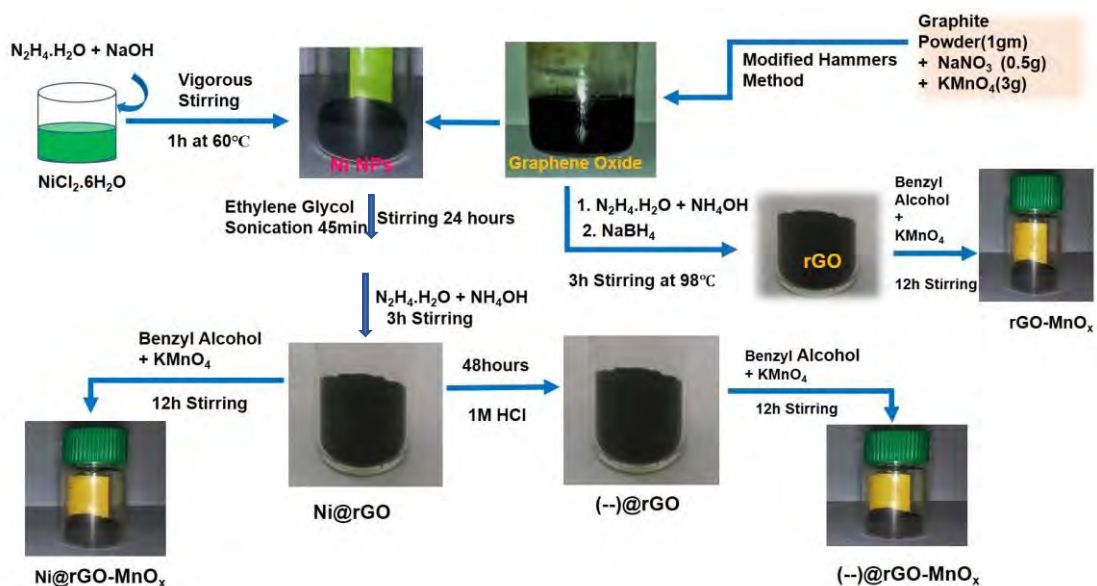


Figure 4.2: A flowchart shows all pathway of Ni-based materials synthesis.

4.2.6 Synthesis of Iron oxide (Fe₃O₄) nanoparticles

Iron Oxide (Fe₃O₄) nanoparticles were synthesized by using precursor mixture FeSO₄ and FeCl₃.6H₂O with a molar ratio of 1:2 at 60 °C for 3 h vigorous stirring [8,9]. In brief, 0.5 M FeCl₃ and 0.25 M FeSO₄ mixed and sonicated for 30 min. Then the mixture was aided for stirring for 1 hour at 60 °C. 50 mL 25% NH₄OH was added dropwise to

the above mixture until the pH raised to 11 and a blackish precipitate was formed and stirred for the next 2 hours. The precipitate was separated with an external magnet and washed with distilled water several times until the pH turned to 7. Finally, the black precipitate was washed with ethanol to remove the unreacted substance and dried at a hot air oven at 100 °C for 12 hours.

4.2.7 Synthesis of Fe₃O₄@rGO core-shell nanostructure and coreless hollow (--@rGO

Fe₃O₄@rGO core-shell spheres were synthesized from Fe₃O₄ NPs and GO by mixing weight ratio 5:1. Specifically, 400 mg GO was added in 100 mL distilled H₂O and 2 g of Fe₃O₄ NPs was added into 100 mL EG and separately aided to sonicate for 1h. The two solutions were then mixed together by sonication for 1 hour and stirred for 24h hours obtained a blackish-brown gel. To obtained Fe₃O₄@rGO core-shell spheres, the mixture was heated to 100 °C and 12 mL of hydrazine hydrate with 6 ml NH₄OH was added into the mixture and the reaction was kept going at 98 °C for 2 hours [2]. The product was harvested by centrifugation and washed with deionized water and ethanol before drying in an oven overnight at 60 °C. The coreless (--@rGO were obtained by dissolving the above prepared Fe₃O₄@rGO core-shell spheres in a 37% hydrochloric acid solution for 4 days [7]. The complete removal of Fe₃O₄ NPs was confirmed by using an external magnet.

4.2.8 Synthesis of Fe₃O₄@rGO-MnO_x composite and (--@rGO-MnO_x composite

For the synthesis of Fe₃O₄@rGO-MnO_x, 400 mg Fe₃O₄@rGO was added into 100 mL DI water and 500 µL benzyl alcohol under mild stirring conditions. The hydrophobic benzyl alcohol was adsorbed on the surface of Fe₃O₄@rGO through ultrasonic treatment for 30 min. 60 mg KMnO₄ was added into the above solution and kept on mild stirring for 12 h [3]. The obtained black precipitate was washed several times with distilled water and ethanol. Then the precipitate was dried 50°C at hot air oven for 12 h. For the synthesis of coreless hollow (--@rGO-MnO_x, 400mg coreless (--@rGO was added instead of Fe₃O₄@rGO with all conditions remaining the same, explained earlier.

The following flowchart shows all pathways of synthesis of $\text{Fe}_3\text{O}_4@\text{rGO}$, coreless $(-)\text{@rGO}$, rGO-MnO_x , Core-shell $\text{Fe}_3\text{O}_4@\text{rGO-MnO}_x$ nanocomposite and coreless $(-)\text{@rGO-MnO}_x$ hollow sphere.

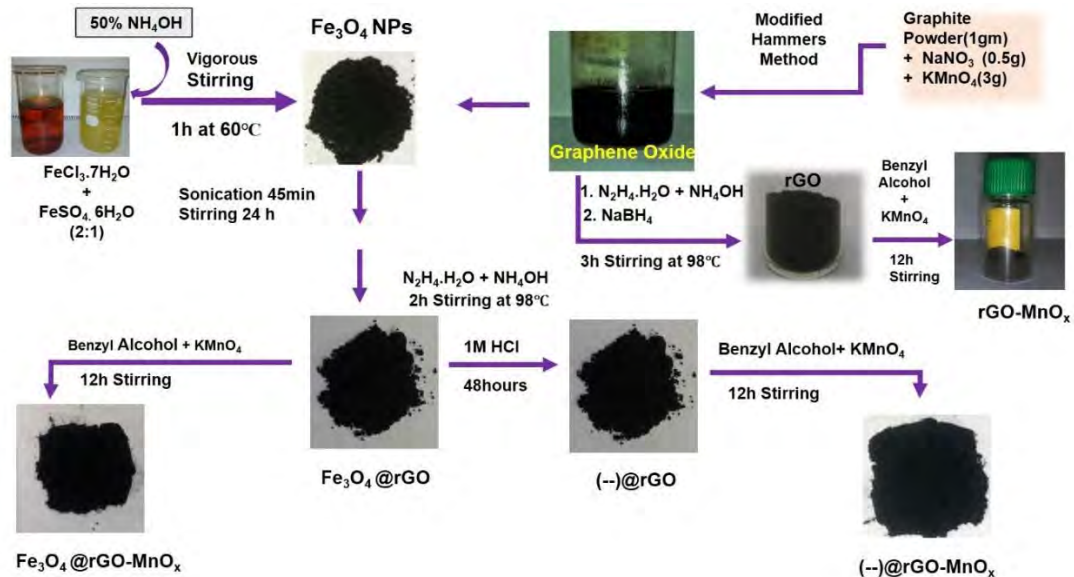


Figure 4.3: A flowchart shows all pathway of Fe_3O_4 based materials synthesis.

4.3 Structural Characterization by X-Ray Diffraction (XRD)

The x-ray diffraction pattern of the nanocomposites was recorded with a PANALYTICAL EMPYREAN X-ray. Diffractometer operating at 40 kV and 40 mA using $\text{Cu K}\alpha 1$ radiation ($\lambda = 1.540598\text{\AA}$), fitted with a scintillation detector. The powdered samples were taken within two plain glass slides ($25\text{mm} \times 75\text{mm}$) forming a film, was placed inside the diffractometer. The measurement was performed in the continuous mode with a scan speed of 3.0 deg/min within the scan range of $0\text{-}70$ degrees while the scan width was 0.02 deg .

4.4 Surface morphology by Field Emission Scanning Electron Microscope (FESEM)

The surface morphology of the samples was analyzed with Schottky Field Emission Scanning Electron Microscope (Model: JSM-7600F, JEOL, Japan) via secondary

electron imaging. In this case, after finely powdering, ~ 1-2 mg of the dried powder sample was placed on a 1 cm × 1cm conducting steel plate which was then dispersed on a conducting carbon glued strip. It was dried with air from the hand pump. The sample loaded strip was then mounted to the main FESEM chamber integrated with the instrument to view sample surface that evacuated to ~ 10⁻³ to 10⁻⁴ torr and then a very thin gold layer (~few nanometers thick) were sputtered on the sample to ensure the conductivity of the sample surface. The acceleration voltage of the electron gun was 5 kV or 10kV with probe current zero and the working distance was ~8 mm. However, voltage for graphene was 15 kV as it is a conductive material that gives better resolution at such high voltage. Various magnification range was used, varying from 5000-50,000 times. The mean particle size, length, diameter, etc. were calculated taking 10-15 measurements from SEM images using “ImageJ” (64-bit Java 1.8.0_112) software.

4.5 Chemical Characterization

4.5.1 Fourier Transform Infrared spectroscopy (FTIR)

The IR spectra of the samples were recorded with an FTIR spectrophotometer (Model “FTIR-8400”, Shimadzu, Japan). In each case, about 1 mg finely ground solid dry sample was mixed with 125 mg of pure and dry KBr powder, ground homogenously in a mortar by a pestle and compressed mechanically in a metal holder under a high pressure to make a translucent pellet. Under pressure, KBr melts and seals the compound into a matrix. The resultant pellet was then placed in the path of the IR beam with a sample holder for measurement

4.5.2 Elemental analysis by Energy Dispersive X-Ray (EDX) spectroscopy

The EDX spectra of the samples were analyzed with the Schottky Field Emission Scanning Electron Microscope (JSM-7600F, JEOL) equipped with an EDX detector within the voltage acceleration range of 0-12 kV as like FESEM.

4.6 Investigation of electrochemical capacitive behavior

The electrochemical performance of a material can be possible to examine by three different methods by CV, GCD, and EIS [8].

4.6.1 Experimental setup

To investigate the electrochemical capacitive behavior of the nanocomposites, a three-electrode system, a single compartment cell was employed, which utilized a modified graphite electrode with only an exposed surface area of radius ~ 0.3 cm as the working electrode. A Platinum (Pt) and an Ag | AgCl | KCl (sat.) electrode were used as counter electrodes and reference electrode respectively. The modification of the graphite electrode was performed by the solvent casting and drop drying method. First, 5~10 mg of active material along with $\sim 25\%$ PVA as a binder was added to a mixture of 100 μL ethanol (EtOH) and 150 μL dimethyl sulphoxide (DMSO). The mixtures were subjected to sonication in a digital ultrasonic bath for 1 hour.

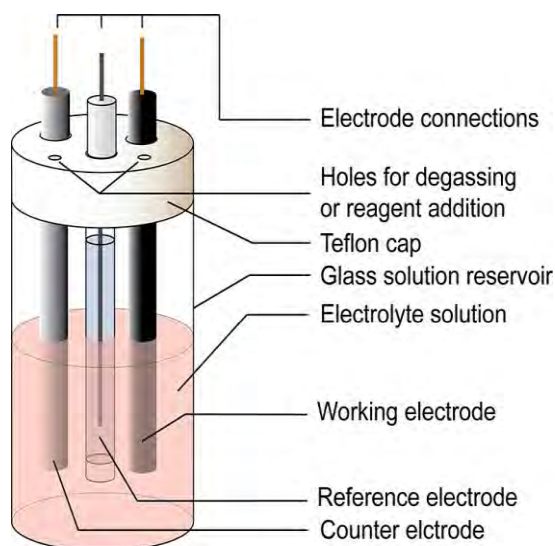


Figure 4.4: Electrochemical cell of three electrode system.

Then, 15 μL of that mixture was cast on the graphite electrode surface with a micropipette in a way that, it left no exposed surface area uncovered. Finally, the electrode was dried at 60°C in an oven for several hours which resulted in the formation of a thin film of the sample on the graphite surface. The experiments were conducted in an electrolyte solution of 0.5 M Na_2SO_4 . Each time, before use, the electrodes were cleaned carefully. The graphite electrode surface was cleaned by polishing

mechanically on a smooth piece of paper placed on the glass. With different samples, all the experiments were performed in a similar fashion. All the electrochemical analysis for a single sample was performed at a time one after another with the same setup.

4.6.2 Electrochemical analysis

The electrochemical characterization such as CV and GCD known as Chronopotentiometry of the nanocomposite was carried out performed using three-electrode system [10] in a computer control Potentiostat/Galvanostat (HANKO HAB-151) and cyclic stability in addition with electrochemical impedance spectroscopy (EIS) of the nanocomposites was carried out in a computer-controlled electrochemical working station (CHI 660E, CH Instruments, USA). The CV of the samples was to find the potential window within which they show capacitive behavior and its dependency on the scan rate. Initially, in each case, CV was taken within -1 to 1.0 V which was later adjusted to the symmetric shape of cyclic voltammogram that corresponds to capacitive behavior. Then, CV was performed at different scan rates, starting from 5 mV/s to up to 50 mV/s. GCD also known as the Chrono-potentiometric technique, was used to evaluate the specific capacitance of the samples with different charging-discharging current or current density varying from 0.1 A/g to 0.9 A/g within suitable potential window chosen from CV. Again, the same potential window was used to find the cyclic stability of the three nanocomposites by observing specific capacitance for the first 50 cycles in general and 500 cycles for the synthesized nanocomposite at the current density 5 A/g. EIS was carried out to investigate the arranged electrochemical system and measure the equivalent circuit resistance. It was performed at different AC potentials within the potential window used for Chronopotentiometric measurement. Impedance data were recorded within the frequency range of 1 mHz to 1 MHz with an amplitude of 10 mV and a quiet time of 2 s at OCP.

4.7 References

- [1] Hummers, W. S., and Offeman, R. E., "Preparation of graphitic oxide", *J. Am. Chem. Soc.*, vol. 80(6), pp. 1339, 1958.
- [2] Lee, J. W. T. E., Hall, A. S., Jong-Duk Kim, J. -D. and Mallouk, "A Facile and template-free hydrothermal synthesis of Mn₃O₄ nanorods on graphene sheets for supercapacitor electrodes with long cycle stability", pp. 19445, 2012.
- [3] S. Wu, W. Chen, and Yan, L., "Fabrication of a 3D MnO₂/graphene hydrogel for high-performance asymmetric supercapacitors", *J. Mater. Chem. A*, vol. 2(8), pp. 2765–2772, 2014.
- [4] Choi, J.Y., Lee, Y.K., Yoon, S.M., Lee, H.C., Kim, B.K., Kim, J.M., Kim, K.M., and Lee, J.H., "A chemical route to large-scale preparation of spherical and monodisperse Ni powders", *J. Am. Ceram. Soc.*, vol. 88(11), pp. 3020–3023, 2005.
- [5] Wu, X., Xing, W., Zhang, L., Zhuo, S., Zhou, J., Wang, G., and Qiao, S., "Nickel nanoparticles prepared by hydrazine hydrate reduction and their application in supercapacitor", *Powder Technol.*, vol. 224, pp. 162–167, 2012.
- [6] Dreyer, D. R., Park, S., Bielawski, W., and Ruoff, R. S., "The chemistry of graphene oxide", *Chem Soc Rev.*, vol. 39, pp. 228–240. 2010.
- [7] Li, C., and Shi, G., "Three-dimensional graphene architectures", *Nanoscale*, vol. 4(18), pp. 5549–5563, 2012.
- [8] Ghasemi, S., and Ahmadi, F., "Effect of surfactant on the electrochemical performance of graphene /iron oxide electrode for supercapacitor", *J. Power Sources*, vol. 289, pp. 129–137, 2015.
- [9] Mohanraj, K., and Sivakumar, G., "Synthesis of γ -Fe₂O₃, Fe₃O₄ and copper doped fe₃o₄ nanoparticles by sonochemical method", *Sains Malaysiana*, vol. 46(10,) pp. 1935–1942, 2017.
- [10] Bard, A. J. and Faulkner, L. R., "Electrochemical methods: fundamentals and applications", John Wiley and Sons, New Jersey, 2001.

Chapter-5

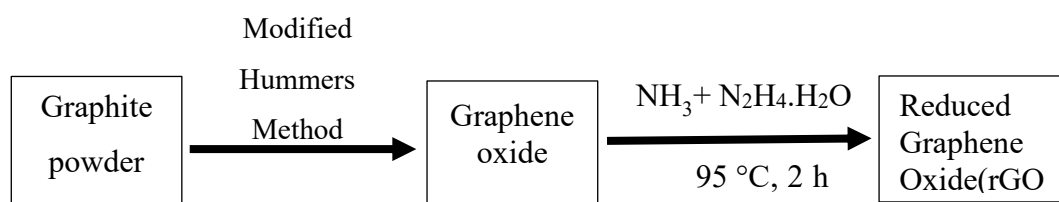
Results and Discussion

5 Results and Discussion

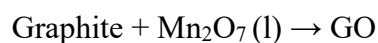
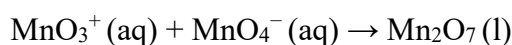
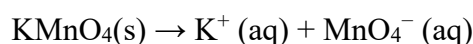
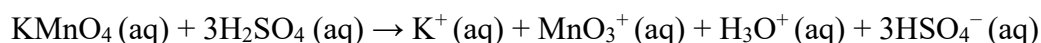
5.1 Synthesis of Materials: Steps of Reactions

5.1.1 Synthesis of Graphene Oxide (GO) and Reduced Graphene Oxide (rGO)

The ternary nanocomposite was synthesized using graphene oxide (GO) as a precursor. GO was synthesized following the Modified Hummers method [1] a well-known and commonly adopted technique in this regard [2,3]. A brief description of the preparation technique is discussed in section 4.2.1 which is nothing but strong oxidation of graphite. In the oxygenation of graphite by combining together sulfuric acid and potassium permanganate which form a dark red di-manganese heptoxide which plays the key role as reported and Sodium nitrate serves as a catalyst in this conversion.



Further oxidation occurs by permanganate ion after the addition of water and before the addition of hydrogen peroxide, which is used to reduce residual permanganate and manganese dioxide from earlier steps. The washing with HCl and water results GO suspension free of impurities [4-7]

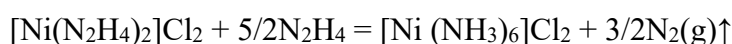
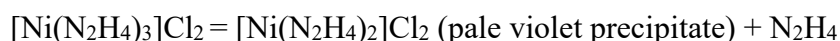
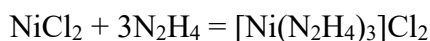


Reduced graphene oxide was prepared from GO by reduction with NH_3 and hydrazine hydrate solution [8]. The mechanism behind this lies in the removal of oxygen-

containing functional groups attached to the carbon plane by hydrogen. It takes quite a time but slow reduction by ammonia solution prevents aggregation of graphene sheets.

5.1.2 Synthesis of Ni nanoparticles, Ni@rGO-MnO₂ and porous crumpled (--@rGO-MnO₂

As the inclusion of Ni to rGO-MnO₂ the spherical Ni nanoparticle is synthesized earlier describe the procedure in section 4.2.3. Ni NPs were synthesized using a highly concentrated NiCl₂ solution as a precursor with NaOH solution and subsequent complexing agent hydrazine hydrate without external heating [9-11]. Ni complex (pale violet precipitate) was formed between NiCl₂ and N₂H₄ solution, and subsequent addition of NaOH solution prompted successive reactions from the Ni complex decomposition via Ni(OH)₂ formation to the reduction of a Ni(OH)₂ gel into well-defined Ni spheres. Considering the molar ratio ([N₂H₄]: [NiCl₂] = 3:1) used, Ni[(N₂H₄)₃]Cl₂ is a probable complex species. The following reaction is

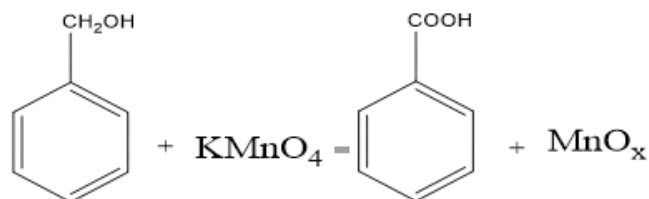


The decomposition of a Ni complex in a highly alkaline environment (pH 13) will result in the formation of Ni(OH)₂ and it can be reduced by N₂H₄ from the following reaction



For the synthesis of core-shell Ni@rGO-MnO₂ nanocomposite and porous hollow (--@rGO-MnO₂ nanosphere, Ni@rGO was synthesized by using EG coated Ni nanoparticles GO. GO involves vinyl functional group derivatives due to the presence of oxygen-functional hydrophilic groups such as hydroxyl, carbonyl, and carboxyl, which facilitate to form strong interaction between EG coated Ni and GO. Ni@rGO core-shell nanosphere was formed using hydrazine hydrate through chemical reduction. Hollow (--@rGO nanosphere etching by using HCl which react with Ni to form NiCl₂ and after then MnO₂ was deposited on Ni@rGO and hollow (--@rGO nanosphere by in situ chemical reduction of KMnO₄ using benzyl alcohol in a neutral medium which was initially anchored to Ni@rGO and (--@rGO in an aqueous suspension.

The hydrophobic benzyl alcohol was adsorbed on the surface of RGO and then self-assemble as MnO₂ nanoparticles [12,13]. The following redox reaction.



In this process, the benzyl alcohol acts as a linker between rGO and MnO₄⁻ ions and also serves as a sacrificial reductant to reduce the aqueous MnO₄⁻ ions into MnO₂. Considering the chemical reduction function of benzyl alcohol to convert GO into rGO, the benzyl alcohol could well prevent the chemical oxidation of RGO. For comparison, rGO-MnO₂ compact composite was synthesized without first two steps of section 5.1.2.

5.1.3 Synthesis of Fe₃O₄, core-shell Fe₃O₄@rGO-MnO₂ nanocomposite, and hollow crumpled (--)@rGO-MnO₂ composite

The magnetic Fe₃O₄ nanoparticles were synthesized by the chemical co-precipitation method, and the detailed procedure is described in section 4.2.6. In a typical mechanism, the sufficient amount of Fe²⁺ and Fe³⁺ ions precursor is mixed with water. However, no precipitate was formed because of low pH and it was pH 2. Hence, a 25 % NH₃ solution was added drop by drop into the solution to increasing the pH from 2 to 9. Subsequently, the brown color precipitate was formed and it was turned into brownish-black at pH 12, due to the following chemical reactions



Fe(OH)₃ and Fe(OH)₂ was formed when pH of the reaction system increases, which are owing to the hydrolysis of Fe³⁺ and Fe²⁺ ions respectively, to produces Fe₃O₄ by rapid nucleation at high pH such more pH 10 [14-18]. Core-shell Fe₃O₄@rGO-MnO_x and hollow crumpled (--)@rGO-MnO_x composite was synthesized by deposition of MnO_x on Fe₃O₄@rGO and (--)@rGO by *in-situ* chemical reduction of KMnO₄ using benzyl alcohol in the neutral medium which was explained in section 5.1.2.

5.2 Characterization

5.2.1 Structural Characterization by X-Ray Diffraction (XRD) analysis

5.2.1.1 Ni-based nanocomposites- (--)*@*rGO, rGO-MnO₂, Ni*@*rGO-MnO₂, and (--)*@*rGO-MnO₂

As shown in Fig. 5.1(a) the XRD pattern of hollow (--)*@*rGO synthesized from Ni*@*rGO shows the broad peak at 26.25° which corresponds to the (002) hexagonal plane of graphene (Lattice: Hexagonal, Space Group.: P63/mmc (194), and cell parameters $a = 2.47$, $c = 6.72$). Besides the intense (002) peak, other low-intensity peaks corresponding to the (100), (004), diffraction planes could also be seen corresponding to the 2θ angles of 43.28°, 54.68°, respectively, in the XRD plot. The crystallite size of the prepared graphene layer using Debye Scherrer equation (Section 3.2) is found equal to 2.17 nm with a lattice strain of 0.0733. A broad peak centered at $2\theta = 26.26^\circ$ corresponding to the interlayer spacing (d spacing) of 3.39 Å (lattice parameters $a = 3.47$ Å, $b = 3.47$ Å and $c = 5.21$ Å), calculated from Bragg's law with a wavelength of Cu K α as 1.5406 Å, which might be attributed to very thin graphene layers due to high degree of exfoliation and the value obtained from the fit into hexagonal is in well agreement with the graphitic nature of carbon [18,19]. The XRD indicates the graphene synthesized is highly reduced from graphene oxide (JCPDS No. 75-1621) [20] removing oxygen-containing functional groups from GO sheets due to reduction by ammonia and hydrazine solutions [1].

For rGO-MnO₂ (shown in Fig. 5.1(b)) and (--)*@*rGO-MnO₂ (Fig. 5.1(c)) the main peaks of the two-dimensional layered birnessite form can be measured at $2\theta = 12.2^\circ$, 24.7° , 36.9° , and 65.7° , confirming the formation of this MnO₂ phase (JCPDS no. 43-1456) [21]. The main peaks are attributed to (001) (002), (111), (100), (312), planes of MnO₂. The birnessite pattern was indexed to a monoclinic type with space group C2/m and unit cell parameters of $a) 5.174$ Å, $b) 2.850$ Å, $c) 7.336$ Å, and $\beta = 103.18^\circ$ [21-23]. The observed broad peaks are characteristic of a poorly crystallized powder. The reduction of MnO₄⁻ produces birnessite-type manganese oxide. Birnessite δ -MnO₂ is a layered manganese oxide formed by [MnO₆] octahedral sharing edges, with alkaline cations and water molecules between layers [22-24]. In order to reveal the crystal structure of the Ni*@* rGO-MnO₂, XRD was conducted and presented in Fig. 5.1(c). It can be seen

that the XRD pattern exhibits three well-resolved peaks at 2θ (44.5° , 51.8° , 76.4°), which coincide with the (111), (200), and (220) planes of nickel nanomaterials, respectively, according to a standard PDF card (No. 04-0850) [9-11], and presence of MnO_2 as form of two-dimensional layered birnessite type structure which can be confirmed by the presence of main peaks at $2\theta = 12.2^\circ$, 24.7° , 36.9° , and 65.7° , (JCPDS no. 43-1456) [22].

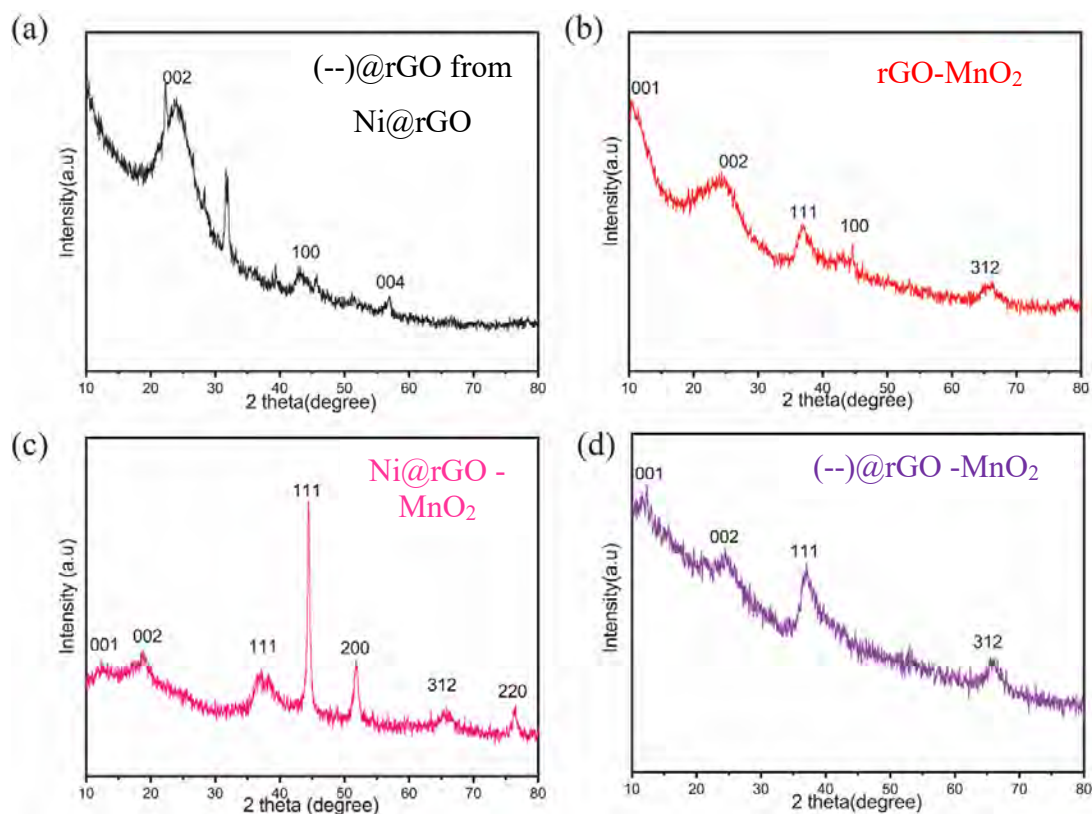


Figure 5.1: XRD patterns of (a) (--)-rGO (b) rGO- MnO_2 (c) Ni@rGO- MnO_2 (d) (--)-@rGO- MnO_2

This suggests that the as-prepared nanomaterials are contained nickel nanoparticles which are coated with rGO that embedded with MnO_2 . The grain size of the nanoparticles can be calculated from the major diffraction peak (111) using Scherrer's equation (section 3.2) [10] using wavelength, λ (0.15418 nm), β the full width at half maximum peak, and θ is the Bragg's angle of the XRD peak. The grain sizes are calculated to be about 12 nm the Scherrer's equation. The characteristic peak of rGO can be distinguished from the others on the XRD pattern of all nanocomposite, although its intensity is relatively weak. The weight percent of rGO is responsible for this [25]. The hazy peak at $2\theta = \sim 25.1^\circ$ can be attributed to the (002) plane of rGO. The absence

of any sharp peak but the presence in the graphitic carbon, related to rGO indicates the surface was covered with a high amount of manganese oxides [22]. Low crystallinity is related to random packing of MnO₂ which is indicated by founding broad peak with weak intensity. It is noticeable that the increase in the degree of crystallization can improve the stability of electrode materials but it's not beneficial for transportation of charge, resulting in the lowed capacitive performance of MnO₂. So, it can be expected that the low crystallinity with the amorphous nature of MnO₂ is good for enhancing capacitive performance [13]. The crystal plane with 2θ of synthesized nanoparticles is shown in table-5.1.

Table: 5-1: The crystal plane with 2θ(°) of synthesized nanoparticles

(-->@rGO	rGO-MnO ₂	Ni@rGO-MnO ₂	(-->@rGO-MnO ₂
12.2° (001)	12.2° (001)	12.2° (001)	12.2° (001)
25.1° (002)	24.7° (002)	24.7° (002)	24.7° (002)
	36.9° (111)	36.9° (111)	36.9° (111)
43.28° (101)		44.5° (111)	
		51.8° (200)	
	65.7° (312)	65.7° (312)	65.7° (312)
		76.4° (220)	

5.2.1.2 Fe₃O₄ based nanocomposites-rGO, hollow crumpled (-->@rGO, rGO-MnO₂, core-shelled Fe₃O₄@rGO-MnO₂ and hollow(-->@rGO-MnO₂

The XRD pattern of hollow crumpled (-->@rGO obtained by exclusion of Fe₃O₄ from Fe₃O₄@rGO by etching with concentrated HCl are shown in Fig. 5.2(a) the broad peak at 25.98° which corresponds to the (002) hexagonal plane of graphene (Lattice: Hexagonal, Space Group.: P63/mmc (194), and cell parameters a = 2.47, c = 6.72). (JCPDS No. 75-1621) [20]. Some other low-intensity peaks corresponding to the 2θ angles of 44.28°, 54.68°, diffraction planes could also be seen corresponding to the (100), (004), respectively, in the XRD plot. The crystalline size of the prepared graphene layer using the Debye Scherrer equation (Section 3.2) is found equal to 2.16 nm with a lattice strain of 0.074. A broad peak centered at 2θ = 25.98° corresponding to the interlayer spacing (d spacing) of 3.40 Å (lattice parameters a = 3.465 Å, b = 3.465 Å and c = 5.2 Å), calculated from Bragg's law with a wavelength of Cu Kα as

1.5406 Å, which might be attributed to very thin graphene layers due to high degree of exfoliation and the value obtained from the fit into hexagonal is in well agreement with the graphitic nature of carbon[18,19]. As per XRD patterns(Fig. 5.2(a)) no corresponding peak for Fe_3O_4 is found indicate that complete removal of Fe_3O_4

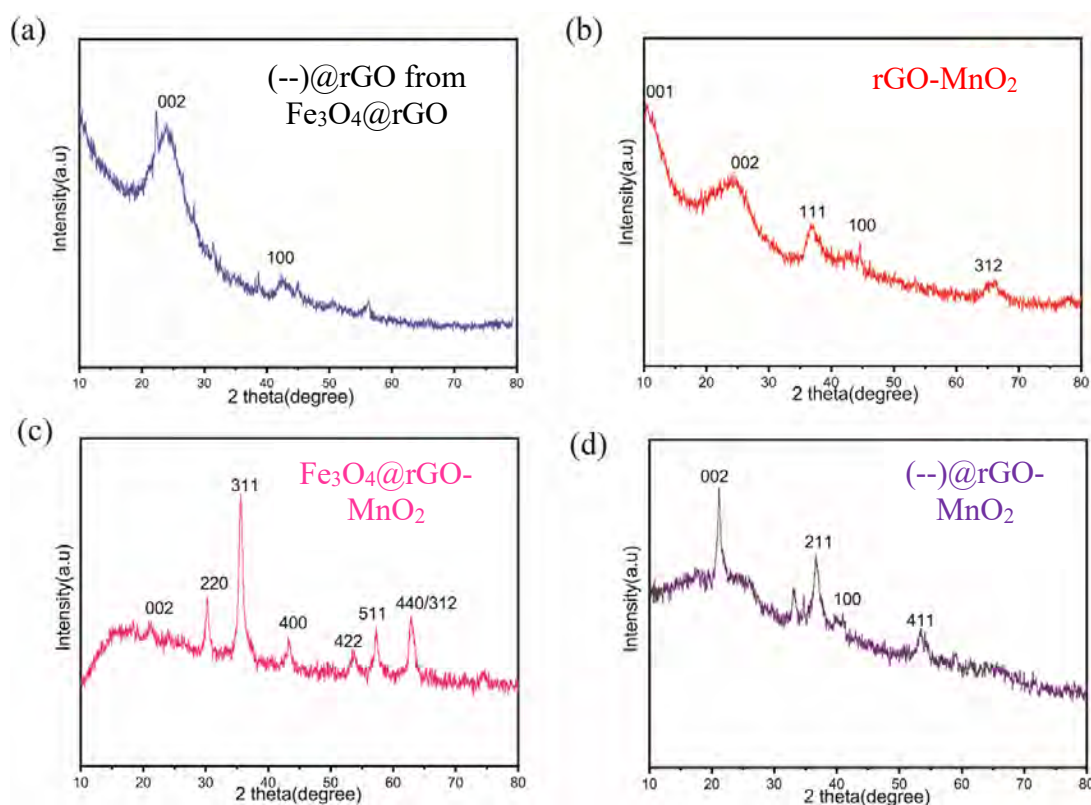


Figure 5.2: XRD patterns of (a) (--)-rGO (b)rGO-MnO₂ (c) Fe₃O₄@rGO-MnO₂ (d) (--)-@rGO-MnO₂.

To obtain the crystal structure of the Fe₃O₄@rGO-MnO₂, XRD was conducted and presented in Fig. 5.2(c). It can be seen that the XRD pattern exhibits well-resolved peaks at 2θ (30.37°, 35.55°, 43.2°, 53.37°, 57.4°, and 62.74°), which coincide with the (220), (311), (400), (422) (511), and (440) planes of cubic magnetite, respectively, according to a (JCPDS NO-880315) [3, 16, 26-27]. and presence of MnO₂ as a form of two-dimensional layered birnessite type structure which can be confirmed by the presence of main peaks at $2\theta = 12.2^\circ, 25.7^\circ, 36.8^\circ,$ and 66° , (JCPDS no. 18-0802) [28].

In case of rGO-MnO₂ and (--)-@rGO-MnO₂, the main peaks of the two-dimensional layered birnessite form can be measured at $2\theta = 12.2^\circ, 24.7^\circ, 36.9^\circ,$ and 65.7° ,

confirming the formation of this MnO₂ phase (JCPDS no. 43-1456) [21] are shown in Fig. 5.2(b) and Fig. 5.2(d), respectively. The main peaks are attributed to (001) (002), (111), (100), (312), planes of MnO₂ with birnessite pattern was indexed to a monoclinic type with space group C2/m and unit cell parameters of a= 5.174 Å, b= 2.850 Å, c= 7.336 Å [21-23]. The observed broad peaks are characteristic of a poorly crystallized powder. The birnessite δ-MnO₂ is a layered manganese oxide formed by [MnO₆] octahedral sharing edges, with alkaline cations and water molecules between layers [22-24].

Table: 5-2:The crystal plane with 2θ(°) of synthesized nanoparticles

(-->@rGO	rGO-MnO ₂	Fe ₃ O ₄ @rGO-MnO ₂	(-->@rGO-MnO ₂
001(12.2°)	001(12.20°)	002(25.7°)	002(25.98°)
002(25.98°)	002(25.98°)	220(30.37°)	
		311(35.55°)	
	111((36.90°)	111(36.80°)	211(39.90°)
	100(43.35°)	400(43.20°)	100(43.35°)
		422(53.37°)	411(55.15°)
		511(57.05°)	
		440(62.74°)	

5.2.2 Chemical Characterization -Elemental analysis by EDX

5.2.2.1 (-->@rGO nanosphere from Ni@rGO

The EDX spectra of (-->@rGO nanosphere are shown in Fig. 5.3. The elemental composition from the EDX spectra of graphene as shown in Table-5.3 indicates that the synthesized product is graphene (80.92% C and 19.07% O). However, there is a small amount of impurities present in the sample corresponding to a very small peak closer to baseline which may be introduced during the synthesis of the material.

Table 5-3: Elemental composition of (-->@rGO

Sample Location	C (Mass %)	O (Mass %)
1	81.23	18.77
2	81.55	18.45
3	80.0	20
Average	80.92	19.07

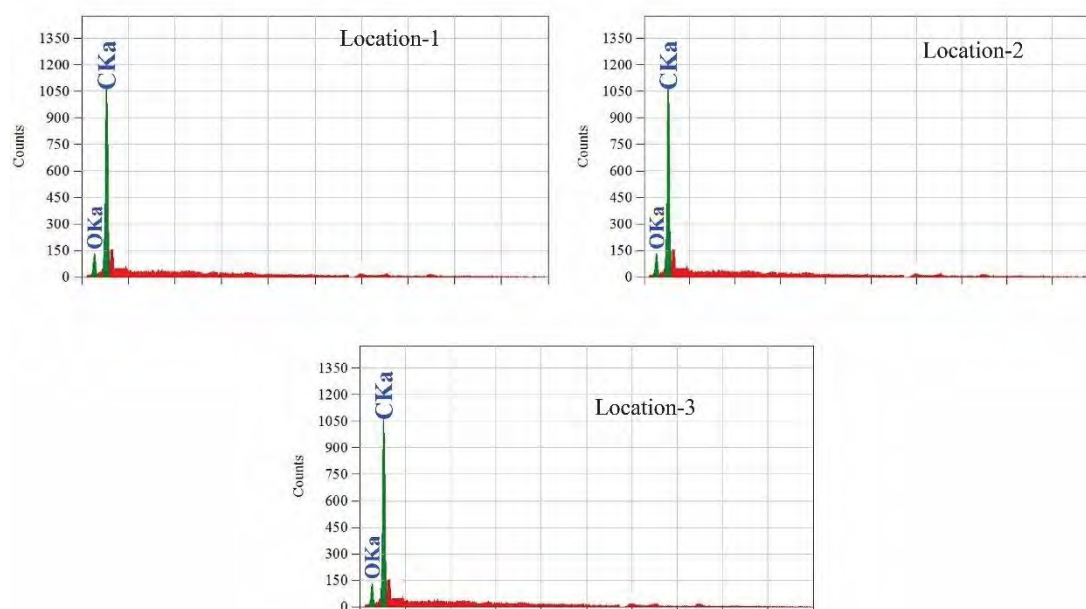


Figure 5.3: EDX spectra at three locations (01, 02 and 03) of (-->@rGO from Ni@rGO.

5.2.2.2 rGO-MnO₂ nanocomposites

Figure-5.4 shown the EDX of rGO-MnO₂ nanocomposite is clear evidence of the formation of manganese oxide nanoparticles on reduced graphene oxide sheet. The relative abundance of oxygen atom compared to manganese atom can be attributed to the presence of moisture along with some oxygen-containing functional group of rGO.

Table 5-4: Elemental composition of rGO-MnO₂

Sample Location	C (Mass %)	O (Mass %)	Mn (Mass %)
1	49.48	27.03	23.49
2	50.30	24.97	24.73
3	31.87	31.62	36.51
Average	43.88	27.87	28.24

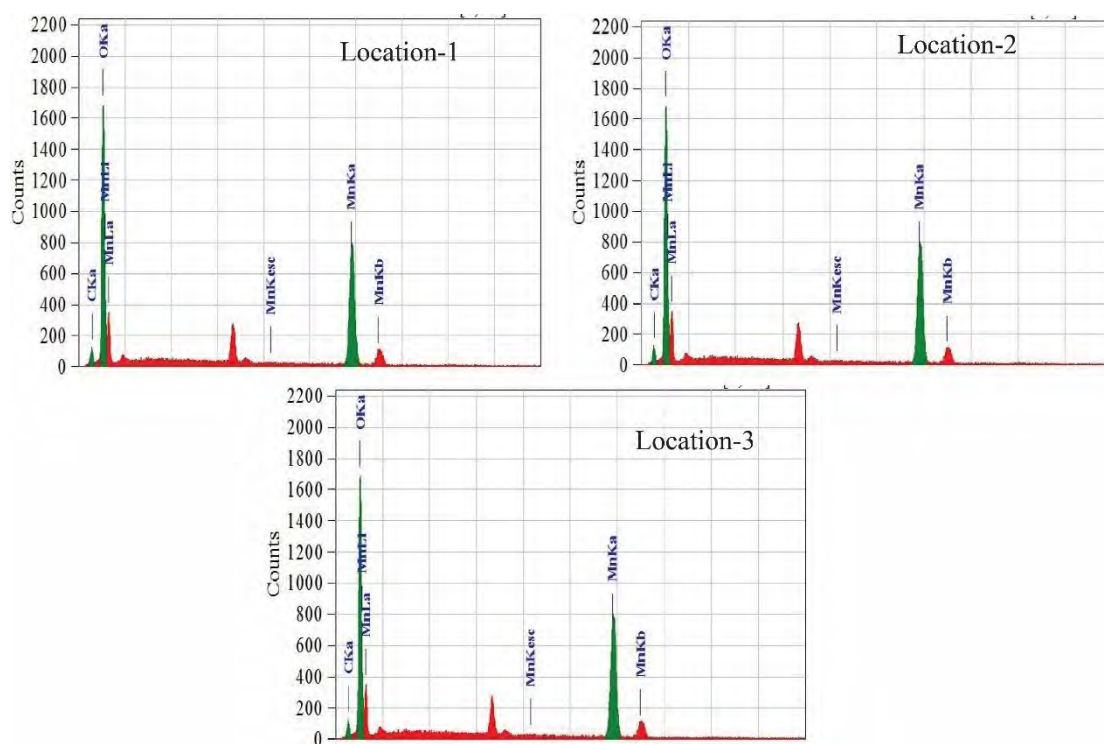


Figure 5.4: EDX spectra at three locations (01, 02 and 03) of rGO-MnO₂.

5.2.2.3 Core-shell Ni@rGO-MnO₂ nanocomposite

The EDX spectrum of core-shell Ni@ rGO-MnO₂ nanocomposite obtained from the incorporation of Ni nanoparticles in the core of rGO-MnO₂ are shown in Figure-5.5

which shows the atomic percentages of Mn, O, Ni and C determined from the intensity of the lines.

Table 5-5: Elemental composition of Ni@rGO-MnO₂

Sample Location	C (Mass %)	O (Mass %)	Ni (Mass%)	Mn (Mass %)
1	12.53	35.64	26.37	25.47
2	12.99	35.20	25.49	26.32
3	10.44	35.67	27.48	26.20
Average	11.99	35.50	26.45	26.03

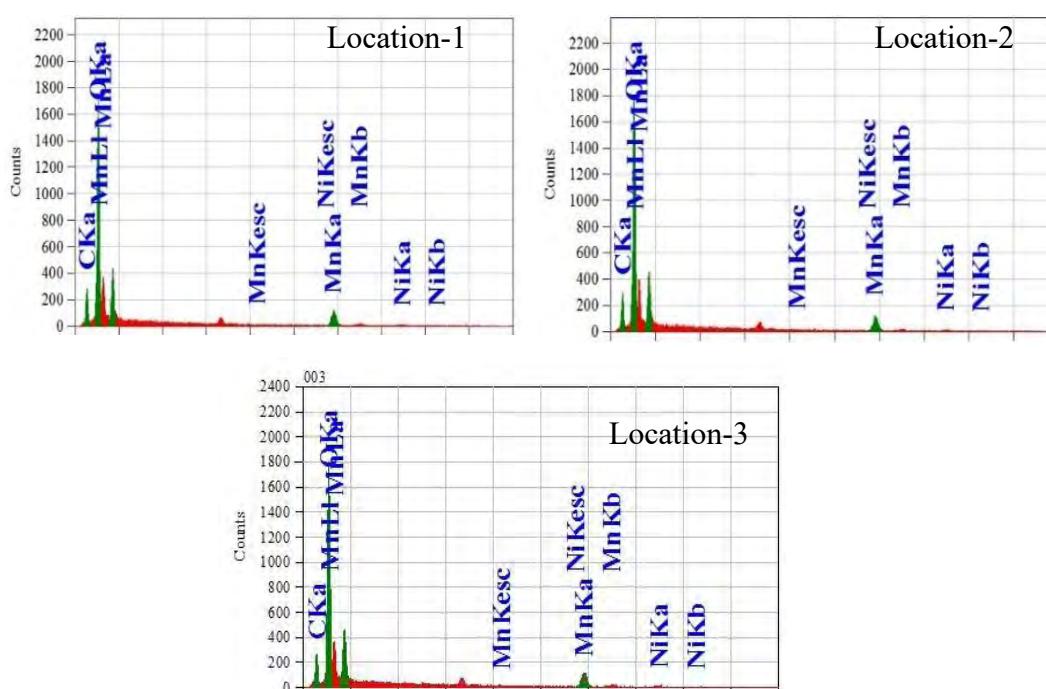


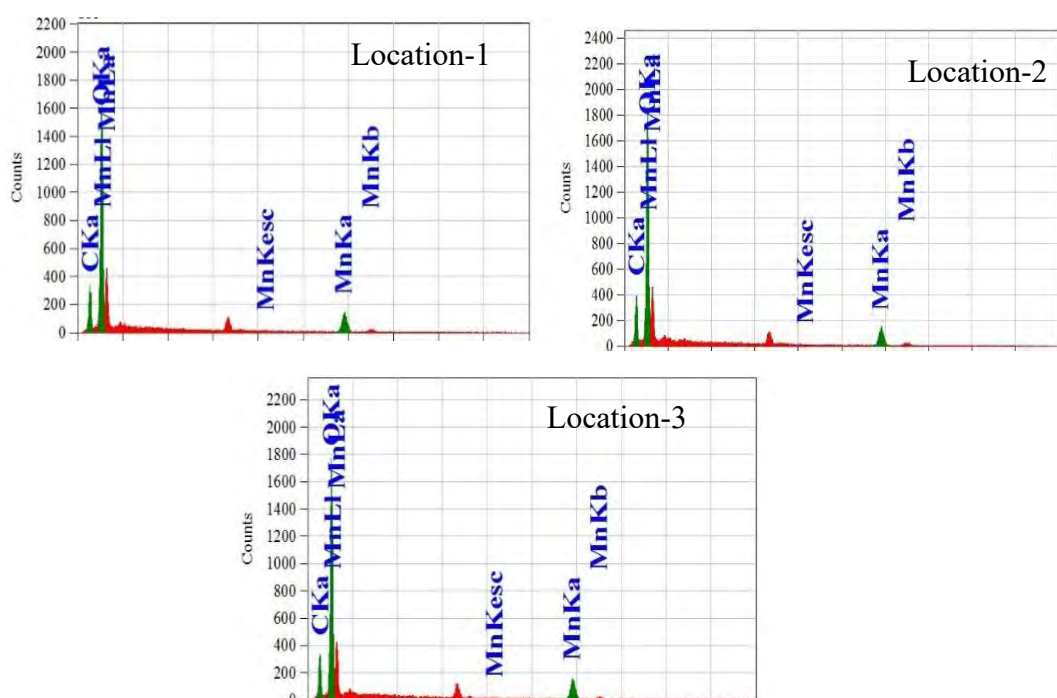
Figure 5.5: EDX spectra at three locations (01, 02 and 03) of Ni@rGO-MnO₂.

5.2.2.4 Hollow crumple (–)@rGO-MnO₂ nanosphere from Ni@rGO-MnO₂

The EDX spectrum of Ni@rGO-MnO₂ ternary nanocomposite obtained from the removal of Ni nanoparticles in the core of rGO-MnO₂ are shown in Figure-5.6 respectively which shows the atomic percentages of Mn, O, and C determined from the intensity of the lines. From the amount, the percentage has clear evidence of the removal of Ni nanoparticles Ni@ rGO-MnO₂.

Table 5-6: Elemental composition of (--)@rGO-MnO₂

Sample Location	C (Mass %)	O (Mass %)	Mn (Mass %)
1	16.54	42.43	41.01
2	15.92	40.98	43.09
3	14.74	40.99	44.27
Average	15.74	41.47	42.79

Figure 5.6: EDX spectra at three locations (01, 02 and 03) of (--)@rGO-MnO₂.

5.2.2.5 Hollow crumpled (--)@rGO nanosphere from Fe₃O₄@rGO

The EDX spectra of hollow graphene synthesized from Fe₃O₄@rGO core-shell structure is shown in Fig-5.7. The elemental composition from the EDX spectra of graphene as shown in Table 5.7 indicates that the synthesized product is graphene (100% C). However, there is a small amount of impurities present in the sample corresponding to a very small peak closer to baseline which may be introduced during the synthesis of the material.

Table 5-7: Elemental composition of rGO

Location	C (Mass %)	O (Mass %)
1	100	0
2	100	0
3	100	0
Average	100	

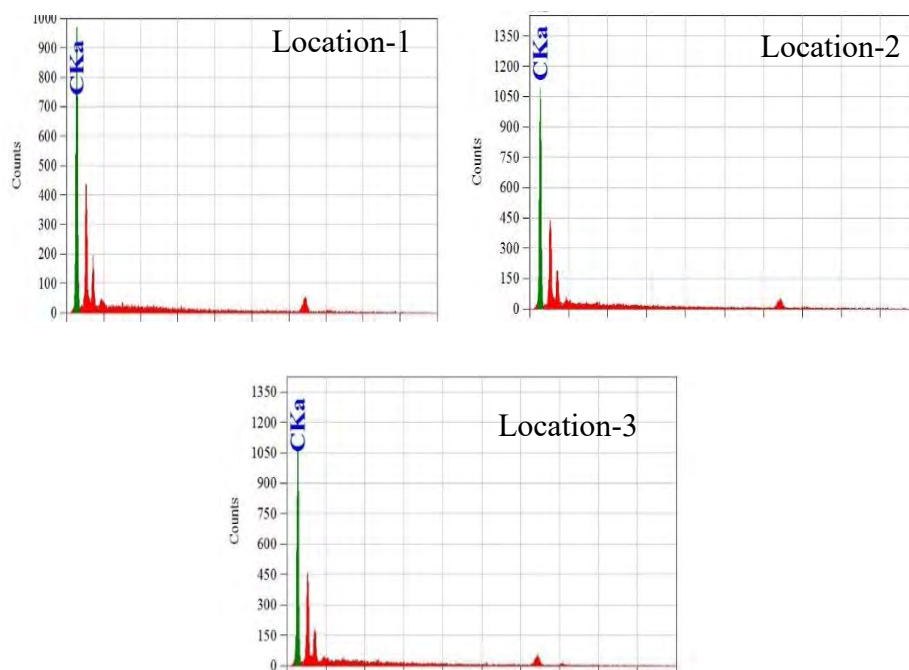


Figure 5.7: EDX spectra at three locations (01, 02 and 03) of (-)-rGO from $\text{Fe}_3\text{O}_4@\text{rGO}$.

5.2.2.6 Core-shell $\text{Fe}_3\text{O}_4@\text{rGO}-\text{MnO}_2$ nanocomposite

The EDX spectrum of core-shell $\text{Fe}_3\text{O}_4@\text{rGO}-\text{MnO}_2$ nanocomposite obtained from the incorporation of iron oxide (Fe_3O_4) nanoparticles in the core of rGO- MnO_2 are shown in Fig-5.8 for three different locations which show the atomic percentages of Mn, O, Fe and C determined from the intensity of the lines.

Table 5-8: Elemental composition of $\text{Fe}_3\text{O}_4@\text{rGO-MnO}_2$

Location	C (Mass %)	O (Mass %)	Fe (Mass%)	Mn (Mass %)
1	36.87	33.09	20.46	9.58
2	30.07	30.69	30.97	8.28
3	24.63	34.61	32.86	7.90
Average	30.52	32.8	27.81	8.59

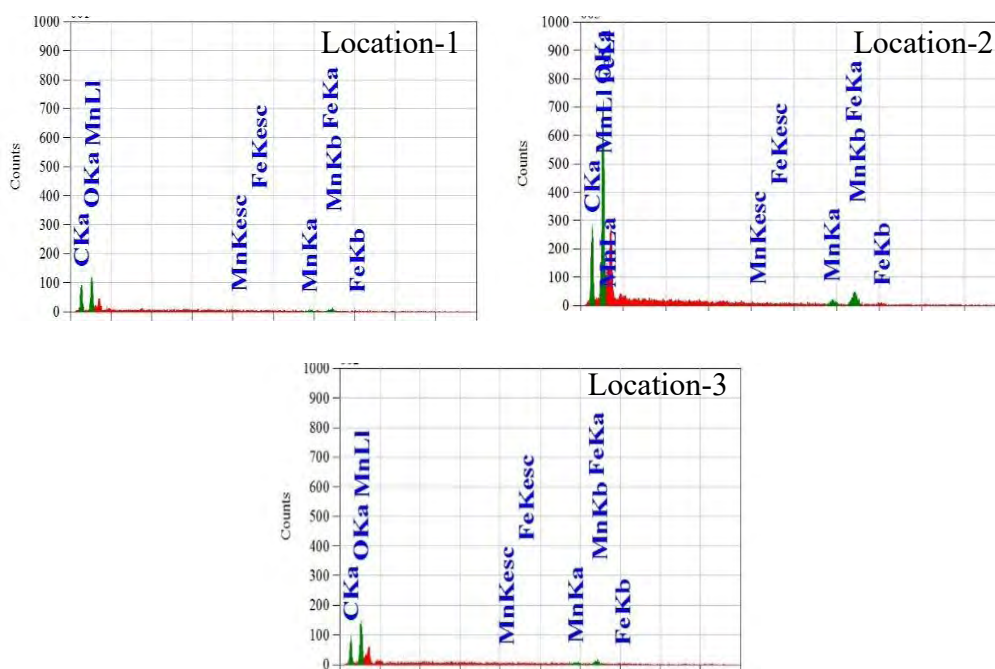


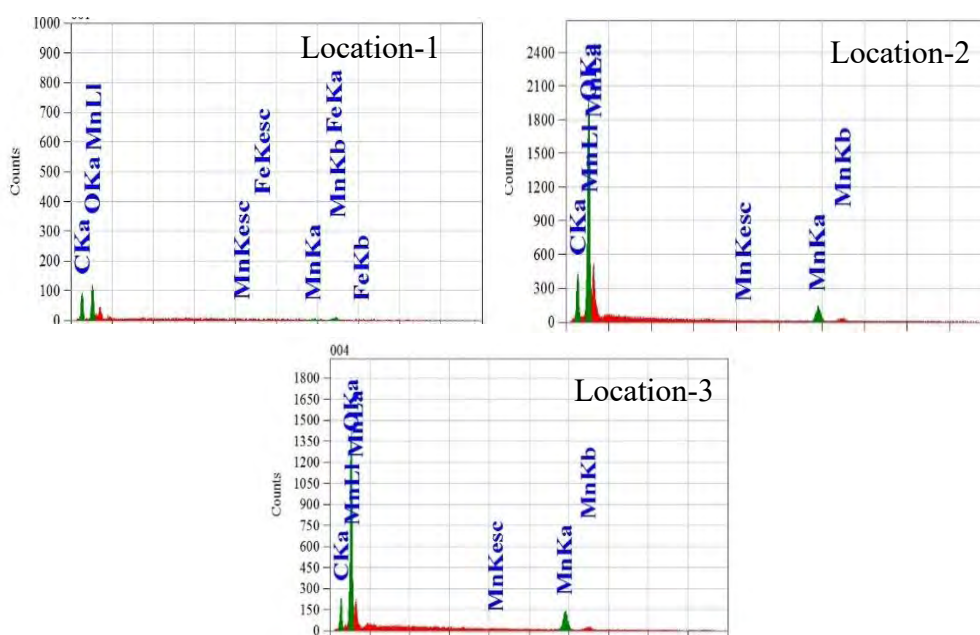
Figure 5.8: EDX spectra at three locations (1, 2 and 3) of $\text{Fe}_3\text{O}_4@\text{rGO-MnO}_2$ core-shell.

5.2.2.7 Hollow crumple ($--$) rGO-MnO_2 from core-shell $\text{Fe}_3\text{O}_4@\text{rGO-MnO}_2$ nanocomposite :

Figure-5.9 shows the EDX spectrum of hollow crumple ($--$) rGO-MnO_2 ternary nanocomposite obtained from removal of Fe_3O_4 nanoparticles in the core of rGO-MnO_2 respectively for three different locations. From EDX the mass percentages of Mn, O., and C determined from the intensity of the lines are measured shown in table-5.9.

Table 5-9: Elemental composition of (--)@rGO-MnO₂

Location	C (Mass %)	O (Mass %)	Mn (Mass %)
1	17.44	46.10	36.46
2	17.88	46.82	35.38
3	12.69	39.95	47.36
Average	16.00	44.29	39.74

Figure 5.9: EDX spectra at three locations (1, 2 and 3) of core-shell Fe₃O₄@rGO-MnO₂

5.2.3 Chemical characterization by FTIR analysis

5.2.3.1 Ni NPs based nanomaterials (GO, rGO, Ni@rGO, hollow (--)@rGO nanosphere, rGO-MnO₂, and core-shell Ni@rGO-MnO₂ and hollow crumple (--)@rGO-MnO₂ nanocomposite):

The FTIR spectra of GO shows the strong broad peak centered at **3440 cm⁻¹** of stretching vibration of O–H bond refers to alcohol and carboxylic acid groups as well as adsorbed water molecules. The weak sharp peak centered stretching vibration at **1720 cm⁻¹** of C=O denotes the presence of a carboxylic group and carbonyl moieties. The weak broad peak centered at **1250 cm⁻¹** of stretching vibration of C-O bond refers

to the presence of the epoxy group. The presence of these groups is further strengthened by the occurrence of weak broad peak centered at 1365 cm^{-1} corresponding to deformed C-OH stretching vibration and medium sharp peak centered at 1060 cm^{-1} corresponding to C-O stretching vibration of alkoxy groups.

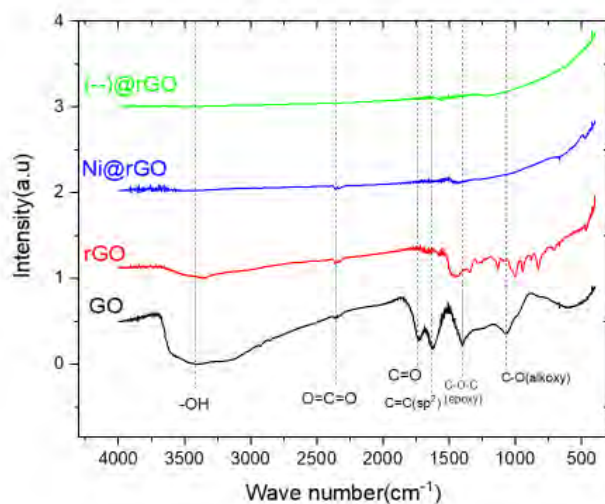


Table 5-10: FTIR bands of Ni

NPs based nanomaterials	
3450	-OH
2360	O=C=O(CO ₂)
1720	C=O(carbonyl)
1580	C=C(sp ²)
1250	C-O-C(epoxy)
1060	C-O(alkoxy)
1350	C-OH deform
1120	C-O-H (stretching)

Figure 5.10: FTIR spectrum of GO, rGO sheet, Ni@rGO, and hollow (--@rGO) nanosphere.

The above information suggests the presence of various oxygen-containing functional groups on its surface assuring its formation. The medium sharp peak centered at $1620\text{--}1660\text{ cm}^{-1}$ is mainly from stretching vibration of C=C bond indicating the presence of sp² hybridized carbon along with a contribution from bending vibration of O-H bond resulting higher intensity [1-4, 6, 29-32]. The chemical reduction of GO to rGO was primarily confirmed by FTIR analysis. The absence of C=O carbonyl peak (1720 cm^{-1}), C-OH deformed bond peak (1365 cm^{-1}) and C-O alkoxy peak (1060 cm^{-1}) indicate the removal of the corresponding groups while the peak at 3450 cm^{-1} correspondings to O-H stretching vibration and the peak at 1230 cm^{-1} corresponding to C-O-C with reduced intensity indicates the presence of alcoholic and epoxy groups respectively at a lower extent compared to GO in rGO sheet, Ni@rGO and hollow (--@rGO) nanosphere[30-34]. Also, for the rGO sheet, the peak at 1120 cm^{-1} of stretching vibration of C-O-H claims an incomplete reduction of GO. The peak at 1580 cm^{-1} comes from C=C skeletal vibration, free of the influence of O-H bending

vibration, Thus, it is safe to assume that rGO has been formed. The peak at 2360 cm^{-1} corresponds to stretching vibration of C=O bond within CO_2 molecule, erupted during the reduction of GO in addition to atmospheric CO_2 [30,32-35].

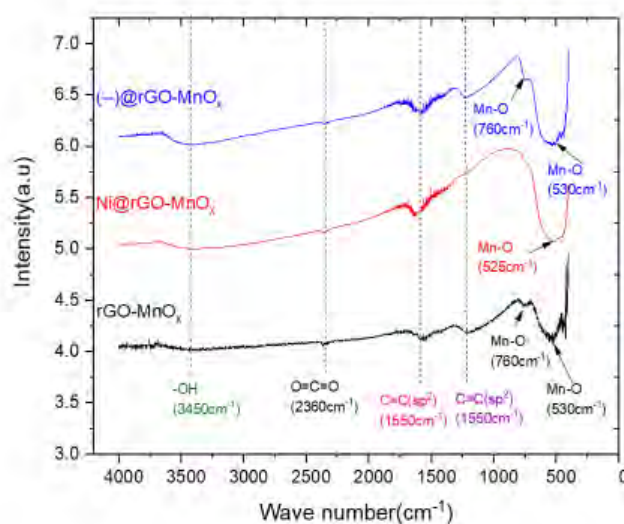


Table 5-11 FIIR bands for Ni NPs based nanomaterials

Frequency(cm^{-1})	Functional Group
3450	-O-H
2360	O=C=O(CO_2)
1550	C=C(sp^2)
1250	C-O-C(epoxy)
760	Mn-O(bending)
530	Mn-O(stretching)

Figure 5.11: FTIR spectrums of rGO-MnO_2 , core-shell Ni@rGO-MnO_2 , and hollow crumpled ($--@rGO-MnO_2$) nanocomposite.

The absorption bands in the range of $400\text{--}750\text{ cm}^{-1}$ for all materials except graphene have corresponded to the characteristic stretching vibrations of O–Mn–O, which demonstrated the presence of the manganese oxide in the sample and The vibration frequency found at 580 and 632 cm^{-1} are characteristic of Mn-O stretching modes in tetrahedral sites, whereas the vibration frequency located at 530 cm^{-1} corresponds to the distortion vibration of Mn-O in an octahedral environment [36-37].

In Fig. 5.11 for the FTIR of rGO-MnO_2 , Ni@rGO-MnO_2 and ($--@rGO-MnO_2$) shows a high-intensity peaks around 530 cm^{-1} , may be assigned to the characteristic stretching vibrations of O–Mn–O corroborating the presence of MnO_2 in the all sample Also, it is found that low intense peak is located around 760 cm^{-1} for rGO-MnO_2 and ($--@rGO-MnO_2$) corresponding to Mn-O stretching vibration [36-37]. The peak at 1551 cm^{-1} refers to C=C(sp^2) skeletal vibration of graphene while the peaks at 3450 , 1250 cm^{-1} corresponding to O-H, and C-O-C respectively predict the presence of certain

functional groups along with water indicating rGO in rGO-MnO₂, Ni@rGO-MnO₂, and (--)@rGO-MnO₂, respectively. The peak at 2360 for C=O stretching vibration of CO₂ is present as usual [34].

5.2.3.2 FTIR analysis of iron oxide-based nanomaterials (GO, rGO, Fe₃O₄, Fe₃O₄@rGO, hollow crumpled (--)@rGO, rGO-MnO₂, Fe₃O₄@rGO-MnO₂ core-shell and hollow (-)@rGO-MnO₂ nanocomposite).

The FT-IR spectrum of Fe₃O₄ nanoparticles, Fe₃O₄@rGO core-shell nanocomposite shows, in Fig, 5.12 & 5.13, broad peaks at 565 cm⁻¹ may correspond to Fe-O stretching vibration mode [18, 26]. A broad peak is centered at 3455 cm⁻¹ corresponds to the stretching vibration of the intermolecular hydrogen bond (O-H) existing between the adsorbed water molecules [2-5]. FTIR spectrum clearly shows the absence of C=O carbonyl peak (1720 cm⁻¹), C-OH deformed bond peak (1365 cm⁻¹) and C-O alkoxy peak (1060 cm⁻¹) indicate the removal of the corresponding groups while the peak at 3450 cm⁻¹ correspondings to O-H stretching vibration and the peak at 1230 cm⁻¹ corresponding to C-O-C [17]. The peak at 1580 cm⁻¹ comes from C=C skeletal vibration, free of the influence of O-H bending vibration [1-4, 6, 29-32].

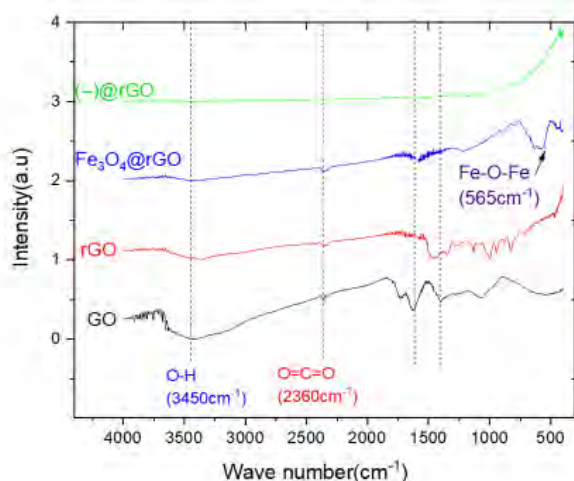


Table 5-12 FTIR band of iron oxide-based nanomaterials

Frequency(cm ⁻¹)	Functional Group
3450	-OH
2360	O=C=O(CO ₂)
1730	C=O(carbonyl)
1550	C=C(sp ²)
1250	C-O-C(epoxy)
1060	C-O(alkoxy)
565	Fe-O-Fe

Figure 5.12: FTIR spectrum of GO, rGO sheet, Fe₃O₄@rGO, and hollow porous (--)@rGO.

The peak at 2360 cm^{-1} for C=O stretching vibration of CO_2 is present as usual. The total absence of all peak in $(--)\text{@rGO}$ indicates the complete removal of the corresponding groups and iron oxide also.

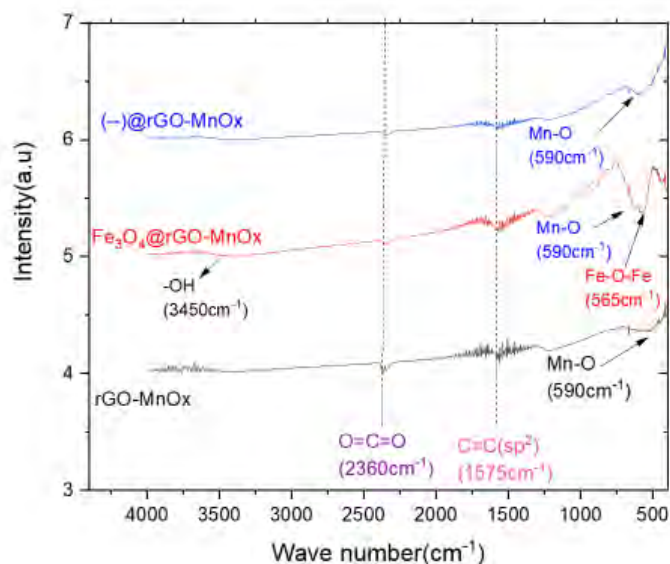


Table 5-13 FTIR bands for iron oxide-based nanomaterials

Frequency(cm^{-1})	Functional Group
3450	-OH
2360	O=C=O(CO_2)
1550	C=C(sp^2)
1250	C-O-C(epoxy)
590	Mn-O(stretching)
565	Fe-O-Fe

Figure 5.13: FTIR spectrums of rGO-MnO_2 , $\text{Fe}_3\text{O}_4\text{@rGO-MnO}_2$, and hollow crumpled $(--)\text{@rGO-MnO}_2$ nanocomposite.

In the case, $\text{Fe}_3\text{O}_4\text{@rGO-MnO}_2$ show two respective peaks at 565 and 590 cm^{-1} may correspond to Fe-O [18,26] and Mn-O [36-37] stretching vibration mode respectively, indicating both Mn-O and Fe-O are present in $\text{Fe}_3\text{O}_4\text{@rGO-MnO}_2$ with all other peaks as like $\text{Fe}_3\text{O}_4\text{@rGO}$ [18,26]. In the case of rGO-MnO_2 and $(--)\text{@rGO-MnO}_2$ shows a broad peak around 580 to 600 cm^{-1} indicating the presence of manganese oxide [36-37]. A broad peak at 590 cm^{-1} for both rGO-MnO_2 and $(--)\text{@rGO-MnO}_2$ corresponding to Mn-O stretching vibration, and no peak appeared at 565 cm^{-1} for $(--)\text{@rGO-MnO}_2$ indicating that the removal iron oxide from the core (Fig. 5.13) which is confirmed by EDX of $(--)\text{@rGO-MnO}_2$

5.2.4 Morphology study by FESEM Analysis

5.2.4.1 Ni NPs based nanomaterials

Figure 5.14(a) shows the FESEM image of rGO synthesized from chemical reduction with hydrazine hydrate of GO with the wrinkled and folded appearance and appear to be very thin with a sheet-like structure having isolated layers arranged intermittently edge-to-edge [36]. It can be explained that during reduction from graphene oxide, hydrazine has readily reacted with the epoxide functional groups to form hydrazine alcohols which are mainly responsible for the incorporation of nitrogen. The view of the graphene sheet has assumed a flake-like structure with a rippled silk surface which is agglomerated. The geometric wrinkling and rippling are caused by the nanoscale interlocking of graphene sheets, providing enhanced mechanical properties, reduced surface energy, increased surface roughness and area [36]. It constitutes multilayers of graphene sheets overlapped in parallel for interpenetration allowing possibly the design of thin-film supercapacitors devices [8]. The corrugations in graphene sheets can cause electron transfer rates 10-folds faster than at the basal plane of graphite [38]. The graphene layers are more or less transparent as observed from the image.

As shown in Figure 5.14(b), the FESEM image of the hollow graphene spheres are indicated it has different geometry like spherical structure by inclusion, leading to a core-shell structure spheres from where graphene nanospheres were prepared by exclusion the Ni template from the core, and the spherical geometry was retained. In addition, it should be pointed out that the electrostatic attraction between the GO sheets and the EG coated Ni spheres plays a key role in the formation of the core-shell structure. The graphene hollow The FESEM image also indicates that the rGO layers were very thin and uniform polydisperse nano ball-like structure of graphene is formed indicated by red circle. This kind of structure may be affected by extra functionalize characteristics such as high surface area and porous nature and short diffusion path for the electrolyte.

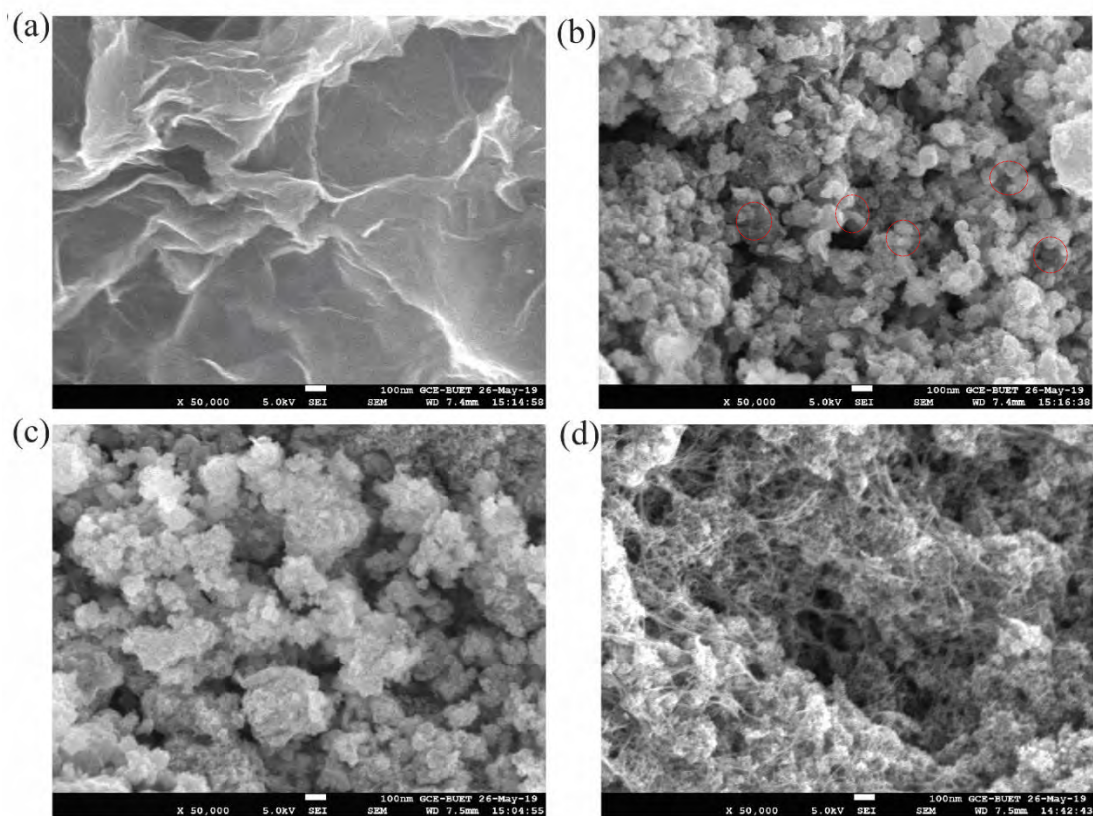


Figure 5.14: FESEM images of (a) rGO (b) (-)-@rGO from Ni@rGO (c) Ni@rGO-MnO₂ and (d) (-)-@rGO-MnO₂ from Ni@rGO-MnO₂.

Figure 5.14(c) shows the FESEM of Ni@rGO-MnO_x core-shell ternary nanocomposite. As can be observed in the image it can be clearly seen that the Ni@rGO core-shell structure is covered with a dense deposition layer of MnO₂ with two type morphology, presenting a dendrite cluster-like structure. It can also be seen that the nanoparticles are of highly nanoporous materials and there occur uniformly distributed spherical aggregates of nanoparticles with random distributions and seems to be poor crystalline from XRD which may enhance the functionality of the materials. In addition to this, the surface consisted of some of the very thin fiber-like products with about 11.3 nm in mean diameter and about 360 nm in mean length, which maintain the morphology of the product. Moreover, it is seen that the surface is highly covered with a large amount of MnO_x nanoparticle with the mean size and area of about 42.8 nm and 85.8 nm respectively on Ni@rGO core-shell spheres. Such a nanostructure could be expected to shorten significantly the distance of ions diffusion in the solid phase and exhibit good pseudocapacitance [12, 38].

Figure 5.14(d) shows the FESEM of hollow crumple (--)@rGO-MnO₂ nanocomposite. As can be observed in the SEM image of the hollow porous (--)@rGO-MnO₂ nanocomposite shows a high yield of manganese oxide nanoparticles covering the surface of hollow porous (--)@rGO spheres, with almost homogenous dispersion with a nanoporous surface which may play an important role in its applications. It can also be seen that the nanoparticles (rod and wire shape) are of highly nanoporous materials and uniformly distributed of nanoparticles on the nanosphere of graphene which may enhance the functionality of the materials. The nanofiber with about 11.3 nm in mean diameter and about 360 nm in mean length, which maintains the morphology of the product. Such a nanostructure would be expected to shorten significantly the distance of ions diffusion in the solid phase and exhibit good pseudocapacitance with EDLC for porous morphology [12,38].

5.2.4.2 Iron oxide-based nanomaterials

The FESEM image of rGO, as per Figure 5.15(a), showing the morphology with the indication of the reduction process reduces oxygen-containing groups, the sheets undergo shrinking with smaller in-between spacing, as seen in the above image with an apparent thickness of ~ 5 nm. The rGO sheet has assumed a flake-like structure with a rippled surface with a wrinkled and folded appearance. Figure 5.15 (b) shows the FESEM of hollow crumpled (--) @rGO prepared from Fe₃O₄@rGO core-shell composite by etching of Fe₃O₄ using HCl. As can be observed in the image it can be clearly seen that the rGO nanosheets are lost its uniform sheet-like structure and highly disorder and crumping occur on the incorporation of iron oxide .it is also point out that the hollow structure is formed by removal of iron oxide with a specific morphology which was retained. Electrostatic attraction between the GO sheets and the EG coated iron oxide plays a key role in the formation of the core-shell structure. The SEM image also indicates that the rGO layers were very thin and uniform polydisperse hollow crumple structure with hexagonal and cube shape is formed. This kind of structure may be affected by extra functionalize characteristics such as high surface area and porous nature and short diffusion path for the electrolyte [39].

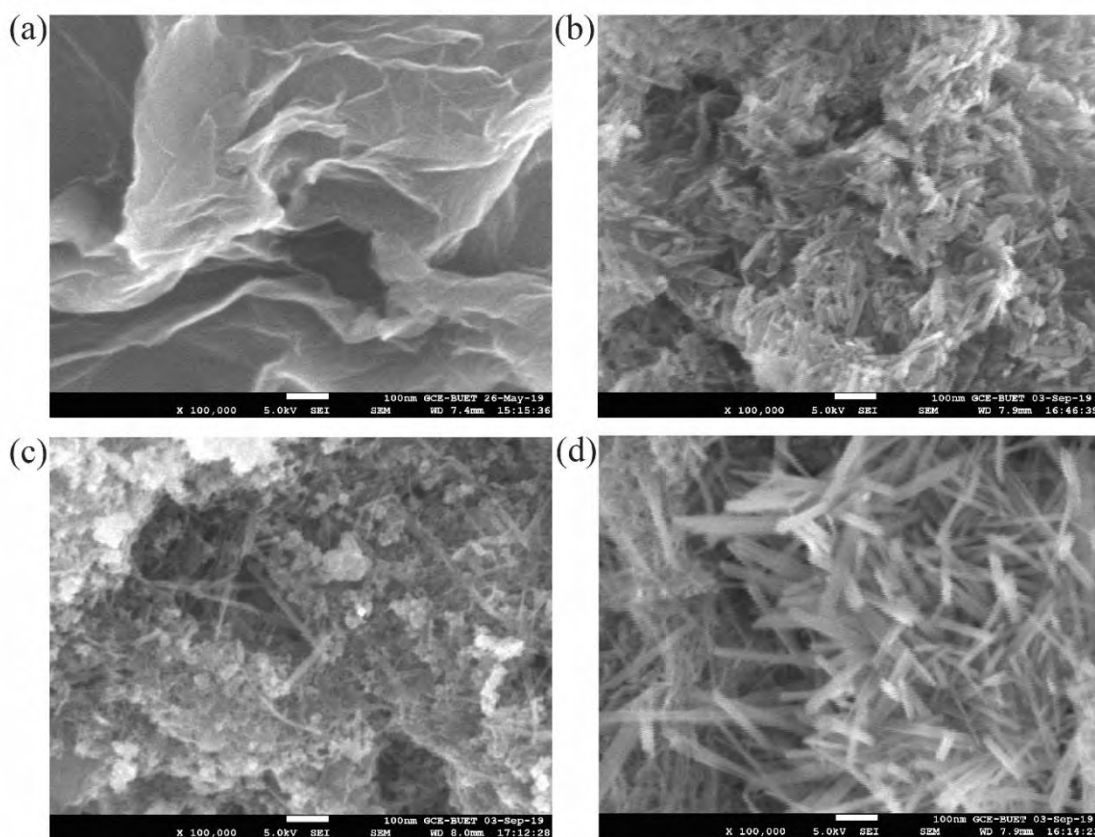


Figure 5.15: FESEM image of (a) rGO sheet (b) (-)-@rGO from Fe_3O_4 @rGO (c) Fe_3O_4 @rGO-MnO₂ and (d) (-)-@rGO-MnO₂ from Fe_3O_4 @rGO-MnO₂.

The FESEM image of Fe_3O_4 @rGO-MnO₂ core-shell nanocomposite is shown in Figure 5.15(c). As can be observed in the image, it can be clearly seen that the Fe_3O_4 @rGO-MnO₂ formed with mixed geometry. It can also be seen that the nanoparticles are highly distributed over the core-shell Fe_3O_4 @rGO nanocomposite and there occur uniformly distributed aggregates of nanoparticles with random distributions and seem to be amorphous, which may enhance the functionality of the materials. In addition to this, the surface consisted of fiber, needle shape nanomaterials with about 12 nm in mean diameter and about 370 nm in mean length, which maintain the morphology of the product. Moreover, it is seen that the surface is highly covered with a large amount of MnO₂ nanoparticle with cube-like shape and the mean size and area of about 42 nm and 80 nm respectively on Fe_3O_4 @rGO core-shell nanostructure. Such type of nanostructure with mixed geometrical shape could be expected to shorten significantly the distance of ion diffusion in the solid phase and serve advantage for good pseudocapacitance [12, 38].

Figure 5.15(d) shows the FESEM image of hollow crumpled (--)@rGO-MnO₂ nanocomposite indicate the highly porous nanoparticle materials which may enhance the functionality of the materials. The FESEM image also shows the presence of dense cube, fiber, and hexagonal like structure with properly distributed and shaped. It can also be seen that the composite forms MnO₂ cube with uniform dispersion which may be attributed to the high surface area which may reason behind its high capacitive properties. Moreover, it is seen that the surface is highly covered with a large amount of MnO₂ cube-like nanoparticle with the mean size and area of about 44 nm and 90 nm respectively on (--)@rGO.

5.3 Investigation of electrochemical performance of Ni-based nanocomposite

The performances of supercapacitors devices using synthesized nanocomposites were analyzed using CV, GCD and EIS.

5.3.1 CV & GCD of rGO, Ni@rGO, and hollow (--)@rGO

The CV curves of rGO, Ni@rGO and hollow (--)@rGO as represented in Figure 5.16(a), (b) and (c) respectively, shows the symmetric small rectangular in shape within the potential range from -0.1 to 0.8 V at different scan rates (2, 5, 10, 20 and 50 mV/s). At high scan rate, the rectangular shape is deformed because of electrolyte ions get little time to penetrate the surface of the electrode. rGO has shown an almost symmetric shaped CV curve for all scan rates(Fig. 5.16(a)), which indicates an electrical double layer capacitor of the electrode material with no pseudocapacitance effect due to functional groups such as epoxy, hydroxyl, and carboxyl functional groups, which came from the chemical synthesis process, indicating the complete reduction of graphene oxide into graphene using ammonia and hydrazine solution and sodium borohydride [8]. CV curve of core-shell Ni@rGO nanocomposite in Figure 5.16(b) is less symmetric with deforming rectangular in shape whereas Figure 5.16(c) is rectangular in shape, indicating an excellent capacitive behavior of (--)@rGO than Ni@rGO. With scan rates, the rectangular shape is deformed more prominent for Ni@rGO core-shell nanocomposites, the curves (Fig. 5.16(a)) exhibited a so-called quasi rectangular shape along the axis without obvious redox peaks even with the introduction of Ni nanoparticles [40]. However, curves show that with increasing scan rates the rectangular shape is not deformed for hollow (--)@rGO nanosphere.

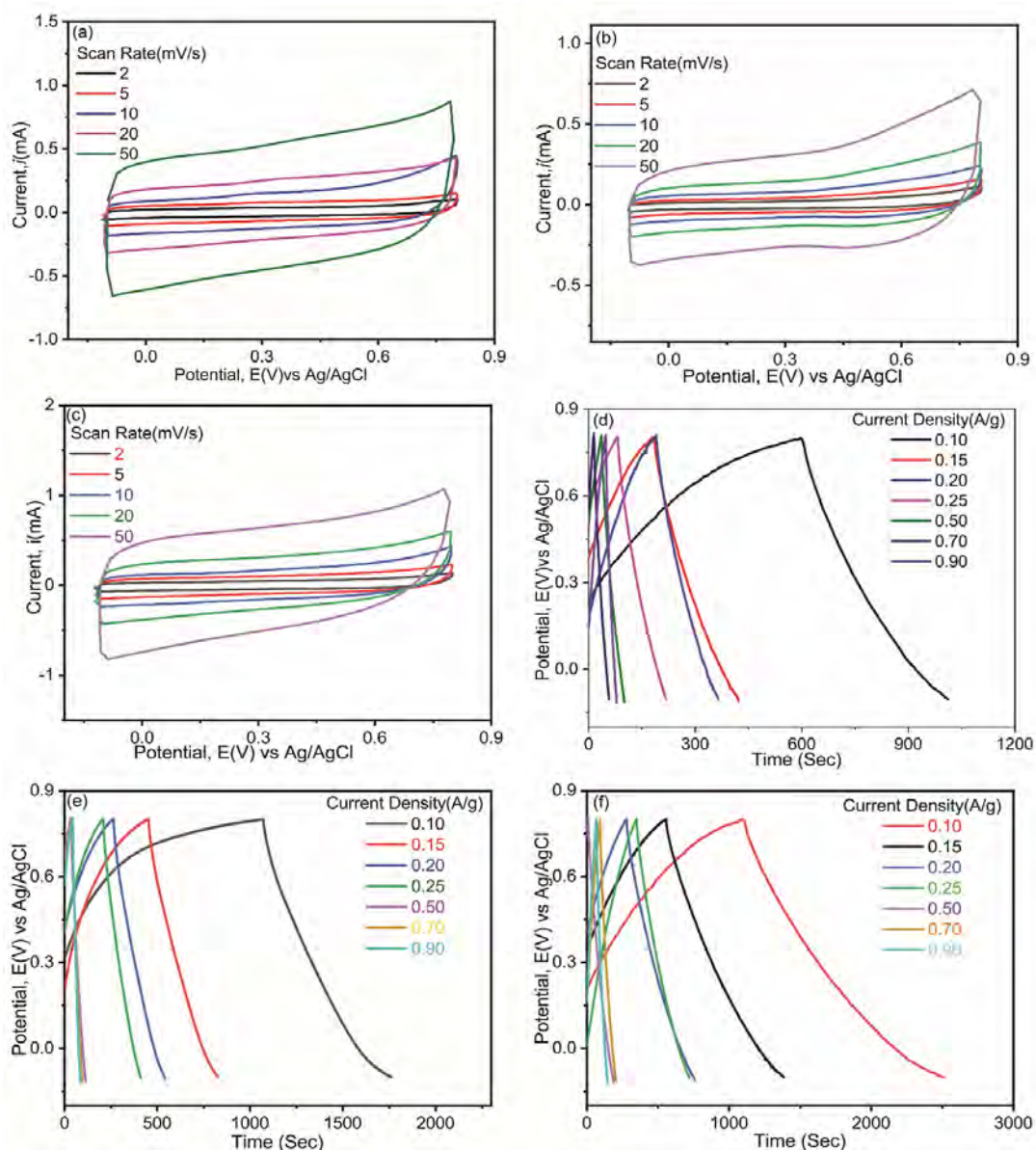


Figure 5.16: CV curves of (a-c) within potential window -0.1 to 0.8 V at different scan rates (2, 5, 10, 20, and 50 mV/s) and GCD curves (d-f) at different current densities (0.1, 0.15, 0.2, 0.25, 0.5, 0.7 and 0.9 A/g) of rGO, Ni@rGO, (-)-@rGO respectively.

It may be for high porosity of graphene hollow and crumple structure compare to graphene sheet for adsorption and desorption electrolyte ions with a facilitating highly porous surface and defend the agglomeration of rGO nanosphere for EDL formation which is shown SEM image in the previous section. The slope variation of GCD curves with respect to the time dependence of potential illustrates that the double layer capacitance behavior of the electrodes resulted from the electrochemical adsorption and desorption

from the electrode-electrolyte interface. The GCD curves of rGO, Ni@rGO and hollow and crumple (--)@rGO as represented in Fig. 5.16(d), (e) and (f) respectively, the shape of the GCD curve is in typical symmetrical or triangular shape, which indicates that there is no pseudocapacitance distortion behavior that may arise from the presence of functional groups in the graphene layer due to incomplete reduction and symmetric triangles without obvious potential drop (IR drop), confirming the characteristic EDLC [41].

To obtain more detailed information on the capacitance performance of the as-prepared graphene nanostructure, GCD curves with various current densities were studied. The highest specific capacitance value was found from the GCD curve at 0.1 A/g current density as 47, 83 and 166 F/g for rGO, Ni@rGO, and hollow (--)@rGO, respectively. The specific capacitance values of rGO, Ni@rGO and hollow (--)@rGO crumple nanosphere are calculated from the Eq. 3.4 shows in table-5.14. It may be noted from Fig. 5.17 that the C_{sp} decreases as usual manner with increasing current density even within a slight changed or adjusted (to get almost symmetric triangular-shaped curve) potential window. The high specific capacitance might be due to more porosity and high surface area of the hollow and crumple (--)@rGO synthesized [42]. The interaction between rGO and Ni nanoparticles produced a better electrochemical performance because it removes the stacking of rGO and may increase surface area.

Table 5-14: Calculated specific capacitance for of rGO, Ni@rGO and hollow (--)@rGO

Current Density(A/g)	rGO	Ni@rGO	(--)@rGO
	Specific Capacitance(F/g)		
0.1	47	83	166
0.15	42	66	147
0.2	40	64	114
0.25	39	58	110
0.5	38	45	103
0.7	34	42	92
0.9	32	40	83

The high surface area of rGO and Ni nanoparticles and conductivity rGO provides better access to electrolytes by facilitating to significantly reduce large stacks of graphene sheets and OH⁻ soaking in bulk materials. Since the electrical conductivity of most metal is poor, using Ni@rGO nanocomposites represent a promising way to

increase the conductivity and promoted the transportation of electrical charges that occurs within the metal nanoparticles and also absorption-desorption of charges on the rGO surface. Hereby, the dual charge-storage mechanism (EDL and pseudocapacitance) benefits the capacitance of the Ni@rGO nanocomposite. On the other hand (--)@rGO porous and hollow crumple structure attributes the outstanding capacitive behavior for their unique structure.

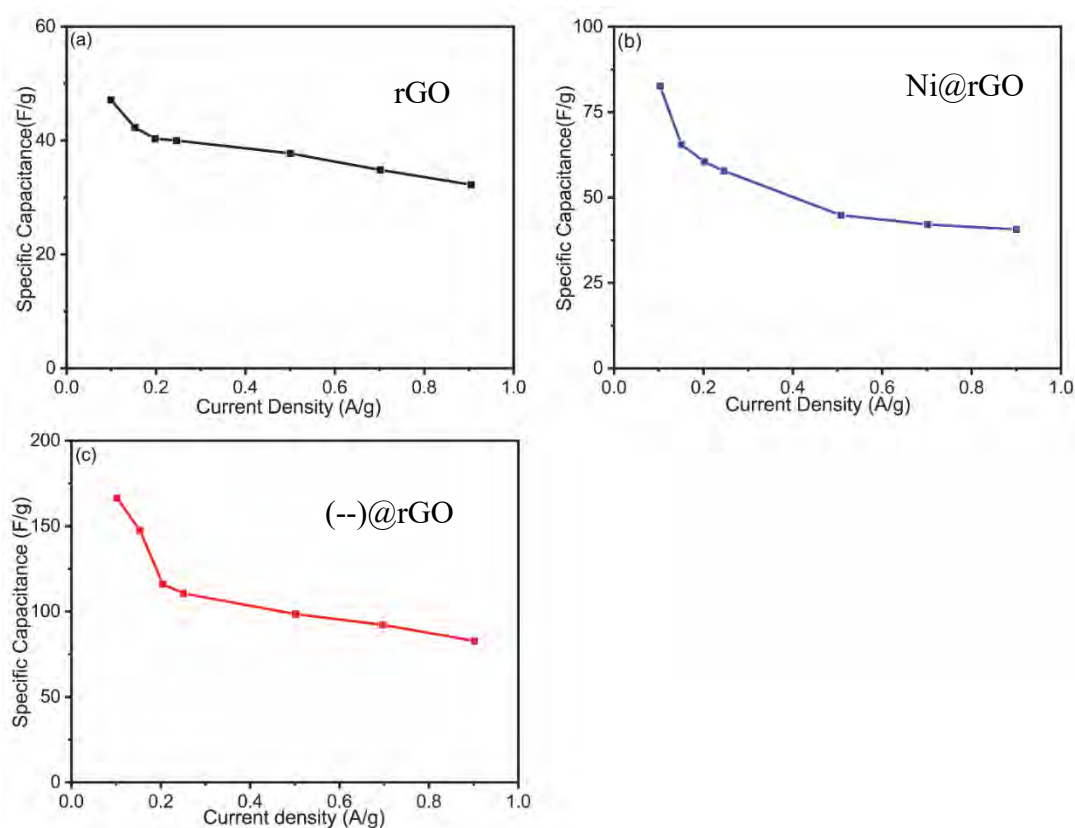


Figure 5.17: C_{sp} (F/g) of (a-c) at different current densities (0.1, 0.15, 0.2, 0.25, 0.5, 0.7 and 0.9 A/g) of rGO, Ni@rGO, (--)@rGO within potential window -0.1 to 0.8 V, respectively.

As the graphene hollow spheres can maintain their structure by removal of Ni template from the core and after being processed to fabricate supercapacitor electrodes, so compared with planar graphene sheets, the hollow graphene spheres are beneficial for better capacitive behavior [42]. Zaid et al. reported G/Ni nanocomposite with high C_{sp} 275 F/g at 2 A/g current density within the potential range which was higher than bare graphene (145 F/g) and bare Ni (3 F/g) synthesized via ball mill process [43].

5.3.2 CV and GCD of rGO-MnO₂ nanocomposite

The CV characteristics curves of rGO-MnO₂ composite is shown in Fig. 5.18(a) within the potential range from -0.1 to 0.8 V at scan rates of (2, 5, 10, 20 and 50 mV/s) in 0.5 M Na₂SO₄ solution respectively. The CV curves shows the symmetric small rectangular in shape within the potential range from -0.1 to 0.8 V at different scan rates. The rectangular shape is slightly deformed with scan rates because of electrolyte ions get little time to penetrate the surface of the electrode at high scan rate.

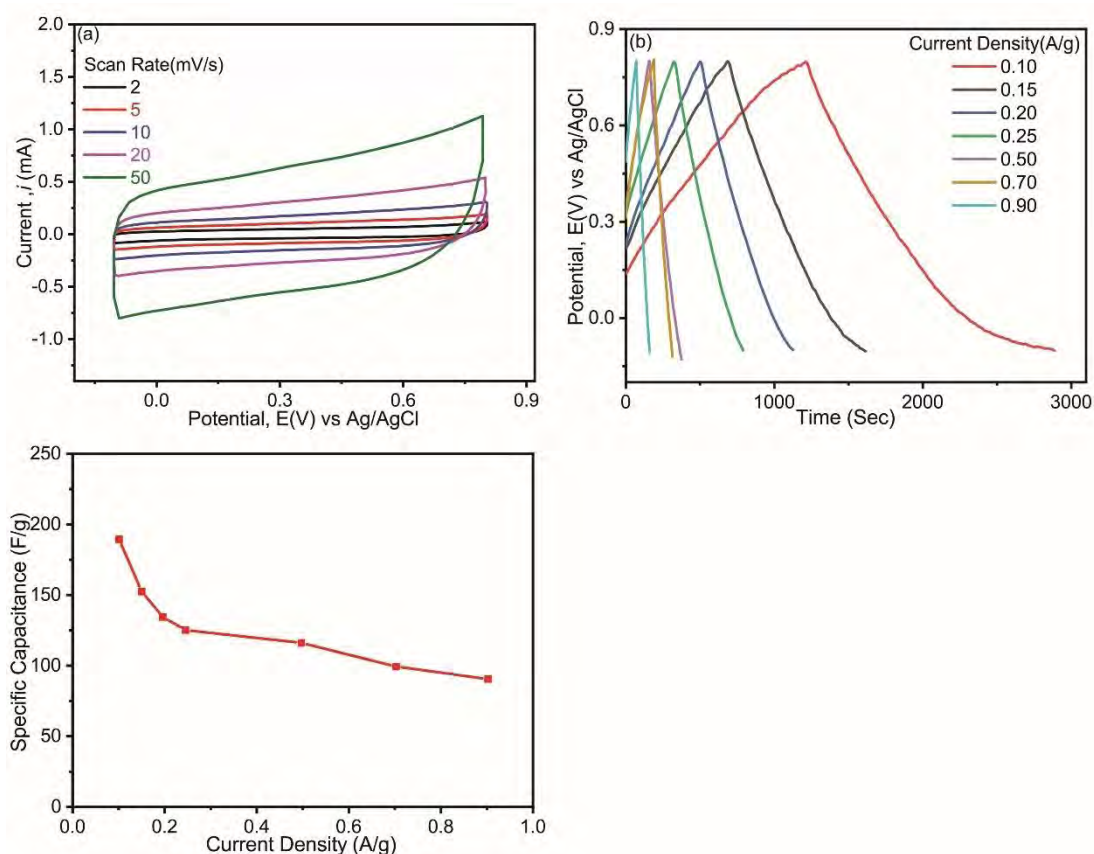


Figure 5.18: (a) CV at different scan rates (2, 5, 10, 20 and 50 mV/s) (b) GCD at different current densities (0.1, 0.15, 0.2, 0.25, 0.5, 0.7 and 0.9 A/g) (c) C_{sp} (F/g) at different current densities within potential window -0.1 to 0.8 V of rGO-MnO₂.

The rGO-MnO₂ nanocomposite shows a rectangular shape, shown in Fig. 5.18(a) with lack of symmetry and improving area of CV indicating the capacitance is probably due to combined double layer and pseudocapacitance contribution [44] which support the Randles–Sevcik equation (current proportional to the square root of scan rate) i.e. different scan rate shows increase of current with the increase of scan rate which is due

to mass transfer ion adsorption-desorption [44]. To obtain more detailed information on the capacitance performance of the as-prepared nanocomposite, GCD curves with various current densities were studied and from the discharging time the calculated capacitance values of rGO-MnO₂ are 189, 152, 135, 125, 116, 99, 90 F/g at current density of 0.1, 0.15, 0.2, 0.25, 0.5, 0.7, and 0.9 A/g, respectively, shows in Fig. 5.18(c). The GCD curves are almost symmetrical to its corresponding discharge counterpart with a slight curvature at low current density, indicating the pseudocapacitance contribution along with double layer contribution. rGO-MnO₂ composite with enhanced electrical conductivity for the incorporation of rGO, promote fast charging and discharging of the MnO₂ nanostructure in the electrolyte and preserving the high-surface-area interface between the MnO₂ nanomaterials and the electrolyte [45]. rGO sheets are agglomeration and growth of MnO₂ on rGO slightly reduced agglomeration and form a compact structure of the solid structure of MnO₂ in the rGO-MnO₂ nanocomposite significantly restricts the electron transfer, resulting in poor electrochemical performance [42,46]. The specific capacitance of mainly for faradic redox between MnO₂ and Na₂SO₄ electrolyte according to the following electrochemical reaction [24]



Thus, the electrical performance of rGO-MnO₂ nanocomposite is little high compared to rGO, Ni@rGO and (-@rGO in capacitance is ascribed to the high inner charge storage and inefficient ion transportation ions due to compact structure of composite and both contribution of EDLC and pseudocapacitance.

5.3.3 CV and GCD of Ni@rGO-MnO₂ nanocomposite

The CV characteristics curves of Ni@rGO-MnO₂ composite are shown in Fig. 5.19(a) within the potential range from -0.1 V to 0.8 V at different scan rates (2, 5, 10, 20 and 50 mV/s) in 0.5 M Na₂SO₄ solution respectively. For core-shell Ni@rGO-MnO₂ nanocomposite shows symmetric quasi-rectangular shape along the axis without an obvious redox peak even with the introduction of Ni nanoparticles, as shown in Fig. 5.19(a), indicating the good capacitive behavior of supercapacitors electrodes for Ni@rGO-MnO₂ the capacitance is probably due to combined double layer and pseudocapacitance contribution.

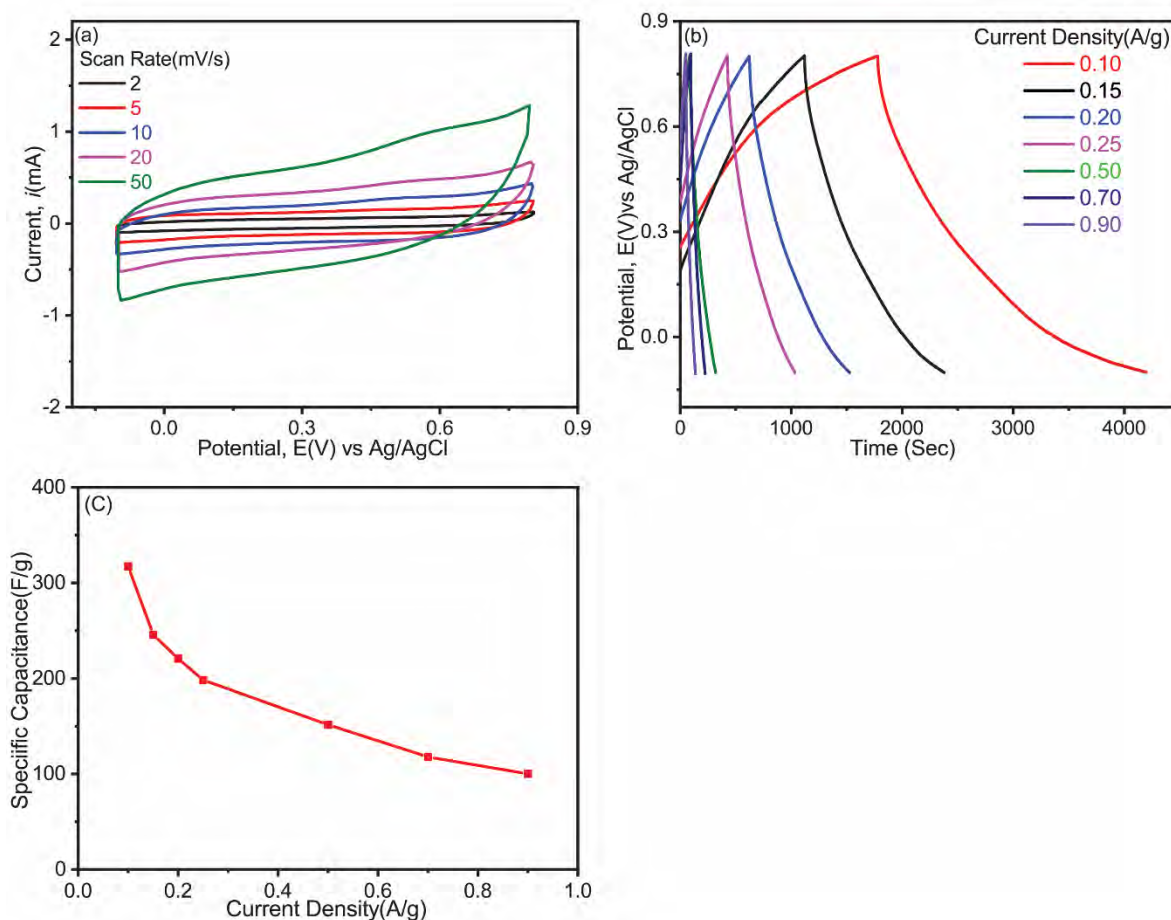


Figure 5.19: (a) Cyclic voltammograms at different scan rates (2, 5, 10, 20 & 50 mV/s) (b) GCD curves at different current densities (0.1, 0.15, 0.2, 0.25, 0.5, 0.7, and 0.9 A/g) (c) Specific capacitance(F/g) at different current densities within potential window -0.1 V to 0.8 V of Ni@rGO-MnO₂.

The shape of the CV curve was still markedly rectangular in shape, even at high scan rates. A very low gradient redox peak has appeared around 0.50~0.55V may responsible for redox reaction occurs for Ni NPs during charging-discharging that may act as a good contributor in overall capacitance. Fig. 5.19(b) shows the GCD curve of core-shell Ni@rGO-MnO₂ nanocomposite at current densities of 0.1, 0.15, 0.2, 0.25, 0.5, 0.7, and 0.9 A/g. The highest specific capacitance value was found from the GCD curve of core-shell Ni@rGO-MnO₂ nanocomposite 317 F/g at 0.1 A/g current density. For studies electrochemical capacitance behavior of synthesizes nanocomposite by the inclusion of Ni in the core of rGO-MnO₂ as shown in Fig. 5.19(b) where the shape of the curve is symmetric triangles without an obvious potential drop (IR drop) of electrode material with confirming the characteristic electric double-layer capacitance and

pseudocapacitance. The capacitance values of core-shell Ni@rGO-MnO₂ nanocomposite are 317, 245, 233, 198, 151, 117 and 100 F/g at current density of 0.1, 0.15, 0.2, 0.25, 0.5, 0.7, and 0.9 A/g, respectively, shows in Fig. 21(c).

The unique combination of Ni and rGO can facilitate transportation for electron by improves the crumbliness of rGO with numerous wrinkles and folds, resulting in further boosting the electrochemical properties of the as-prepared Ni@rGO-MnO₂ nanocomposites. Therefore, during the charge-discharge process, ion and charge transport is faster, may favor the cycle life stability [24,47]. In addition, the incorporation of clusters and rod-like MnO₂ over the core-shell Ni@rGO structure initiates the combined effect of pseudocapacitance arising from Ni and MnO₂ sites and the EDLC contribution by the rGO with preserving the high-surface-area interface between the MnO₂ nanomaterials and the electrolyte and reducing the stacks of graphene which makes the composite highly accessible for electrolyte ions for adsorption-desorption [48]. Hereby, the dual charge-storage mechanism benefits the capacitance of the Ni@rGO-MnO₂ nanocomposite.

5.3.4 CV and GCD of hollow and porous (--)@rGO-MnO₂ nanocomposite

The CV of hollow and porous (--)@rGO-MnO₂ are shown in Fig. 5.20(a) within the potential range from -0.1 to 0.8 V at different scan rates of 2, 5, 10, 20 and 50 mV/s in 0.5 M Na₂SO₄ solution, respectively. The CV curve are the nearly rectangular-like shape within the potential window, indicating the ideal capacitive behavior at all scan rates. However, the current response of hollow and porous (--)@rGO-MnO₂ nanosphere was much high which was ascribed to the unique porous and crumpled structure which supported the SEM image. However, curves show that with increasing scan rates the rectangular shape is not deformed that may for high porosity of nanostructure for adsorption and desorption electrolyte ions. Similar rectangular CV curves reveal the ideal pseudo-capacitive nature which can be attributed to fast electro-sorption of Na⁺ cation and the subsequent quick reversible faradaic process proceeding of nanofiber and rod shape MnO₂ from porous and hollow (--)@rGO-MnO₂ [24] mention in Eq. 5.1. It is also noted that Fig. 5.20(a) that the CV of (--)@rGO-MnO₂ extends to a wide region of positive and negative current indicating its better electronic conductivity due to easy movement of ions through hollow and porous graphene which is supported the Randles-Sevcik equation, indicating porous and more accessible

surface area due to crumple and hollow nature of the rGO, an important factor for charge storage by EDLC [28,49]. GCD with various current densities were studied, as shown in Fig. 5.20(b). The highest C_{sp} value was found from the GCD curve of hollow and porous (--)-@rGO-MnO₂ nanosphere 688 F/g at 0.1 A/g current density respectively.

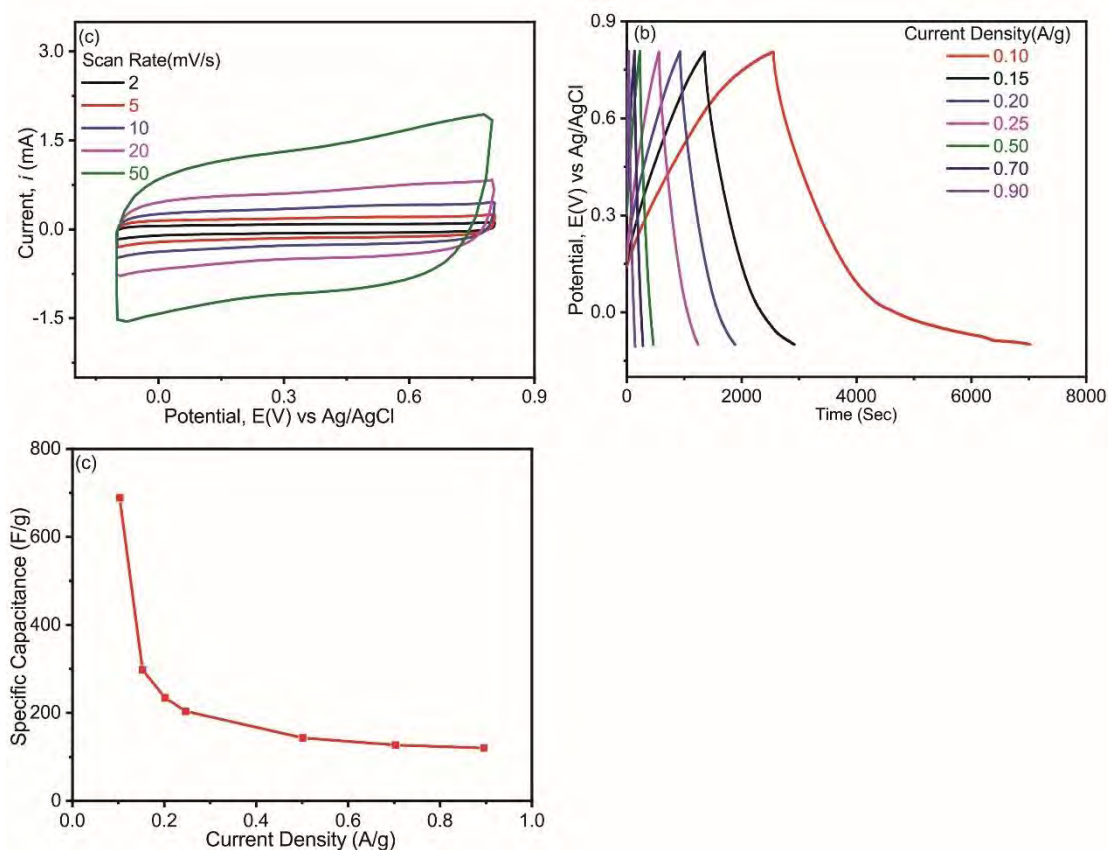


Figure 5.20: (a) CV curves at different scan rates (2, 5, 10, 20 and 50 mV/s) (b) GCD curves at different current densities (0.1, 0.15, 0.2, 0.25, 0.5, 0.7, and 0.9 A/g) (c) C_{sp} (F/g) at different current densities within potential window -0.1 to 0.8 V of hollow (--)-@rGO-MnO₂.

The capacitance values of (--)-@rGO-MnO₂ are 688, 297, 234, 203, 143, 126, 120 F/g at current density of 0.1, 0.15, 0.2, 0.25, 0.5, 0.7, and 0.9 A/g. The GCD curves of (--)-@rGO-MnO₂ are tained symmetrical to its corresponding discharge counterpart with a slight curvature at low current density, indicating the materials undergoing certain internal oxidation-reduction [28] and the diffusion of ions from the electrolyte can gain access to almost all available pores of the electrode, leading to a complete insertion reaction which is responsible for high capacitance which is probably due to

the combination of EDLC from rGO and pseudo-capacitance from the redox reaction of MnO_2 . The $(\text{--})@\text{rGO-MnO}_2$ electrode exhibits significantly improved electrochemical performance which is attributed from their unique hollow and porous spherical structure with rod and fiber shape MnO_2 which undergoes faradic redox reaction with Na_2SO_4 electrolyte shown in Eq. 5.1 .

By removal of Ni template from core the graphene can maintain their porous crumpled structure with more accessible surface area after being processed to fabricate supercapacitors electrodes, so compared with MnO_2 on planar graphene sheets, the hollow $(\text{--})@\text{rGO-MnO}_2$ nanosphere offers various unique features from improving the specific capacitance [42]. Thus, the dual charge-storage mechanism, enlarged and accessible surface area, porous spherical structure, reduce large stacks benefits to the improved specific capacitance of the hollow $(\text{--})@\text{rGO-MnO}_2$ nanosphere used as supercapacitors materials[46].

5.4 Comparative studies on electrochemical performances of Ni-based nanomaterials

5.4.1 CV and GCD analysis

To compare the variation of electrochemical performance of hollow and porous $(\text{--})@\text{rGO-MnO}_2$ due to inclusion and exclusion of core Ni nanoparticles with that of the core-shell $\text{Ni}@\text{rGO-MnO}_2$ and rGO-MnO_2 electrodes, CV and GCD were estimated within a potential range of -0.1 to 0.8 V vs Ag/AgCl in 0.5 M Na_2SO_4 at scan rate 5 mV/s are shown in Fig. 5.21(a). The nature of the CV curve of hollow and porous $(\text{--})@\text{rGO-MnO}_2$ nanosphere is actual rectangular with much larger rectangular area which indicates excellent capacitive behavior of over $\text{Ni}@\text{rGO-MnO}_2$ and rGO-MnO_2 nanocomposite, which is probably due to the combination of EDLC from hollow rGO nanosphere and pseudo-capacitance from the redox reaction of porous MnO_2 nanorods.

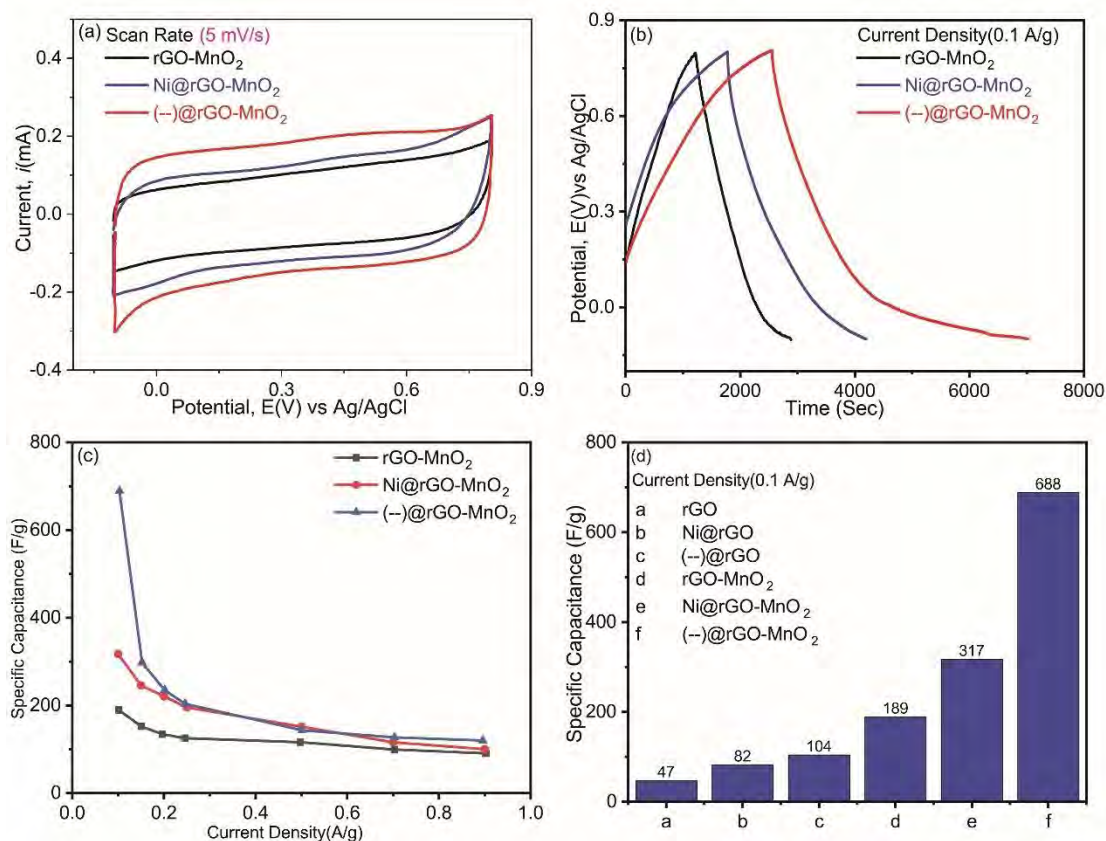


Figure 5.21: (a) CV curve at scan (5 mV s^{-1}) (b) GCD curve at current density (0.1 A/g) (c) and (d) C_{sp} (F/g) at current density (0.1 A/g) within -0.1 V to 0.8 V of Ni-based nanomaterials.

The GCD measurements of hollow and porous (-)@rGO-MnO₂, core-shell Ni@rGO-MnO₂, and rGO-MnO₂ nanocomposite were carried out at current density 0.1 A/g , as shown in Fig. 5.21(b). The GCD curve of (-)@rGO-MnO₂ are tainted symmetrical than that of Ni@rGO-MnO₂ and rGO-MnO₂ to its corresponding discharge counterpart with a slight curvature at 0.1 A/g current density, indicating the materials undergoing certain internal oxidation-reduction [28] and the diffusion of ions from the electrolyte can gain access to almost all available pores of the electrode, leading to a complete insertion reaction which is responsible for high capacitance which is probably due to the combination of double-layer capacitance from rGO and pseudo-capacitance from the redox reaction of MnO₂.

Using Eq. 3.4. C_{sp} are calculated from the corresponding discharge curves, shown in Fig. 5.21(c) and the highest values are 688, 317 and 189 F/g at 0.1 A/g , respectively. The hollow and porous (-)@rGO-MnO₂ nanocomposite exhibits a much longer

charge/discharge time (of about more than 3 times) than that of the rGO-MnO₂ nanocomposite. The higher specific capacitance of hollow and porous (--)@rGO-MnO₂ nanosphere can be attributed to the synergetic effect of the high conductivity of porous and hollow rGO sphere and rapid redox process rod-shaped structure of MnO₂. As compared to MnO₂ on planar graphene sheets, the hollow and porous (--)@rGO-MnO₂ nanosphere having some unique properties such as (1) it can reduce large stacks of rGO with facilitate more accessible surface area available for electrolyte ion adsorption which improve the electron transfer rate [42-46]; (2) it offers more free spaces in and between rGO and MnO₂, that offers fully wetted rGO by electrolyte to the electrochemical sites and provides short diffusion path lengths for adsorbing ions with high conductivity [42-46]; and (3) the active electrolyte ions (Na⁺) to intercalate and de-intercalate more easily and sufficiently from the electrolyte by enlarged and accessible surface area [42-46]. Meanwhile, the compact structure of the MnO₂ solids on rGO sheet leads to the poor specific capacitance of rGO-MnO₂ nanocomposite significantly restricts the electron transfer, with a low accessible surface area and less contact of electrolyte ion with active materials, resulting in poor electrochemical performance [42-46].

5.4.2 Determination of energy density and power density

The energy density (E) and power density (P) of the prepared materials were calculated from the known highest capacitance value of the sample obtained either from CD curves using the Eq. 3.5 and 3.6. Thus, the nanocomposite, hollow (--)@rGO-MnO₂ with the highest capacitance value (688 F/g), among them as prepared nanomaterials will store greater the amount of energy in a small amount of volume than that of all other prepared nanomaterials indicating a good electrode candidate for supercapacitors with the good electrochemical properties. It may be noted that a high energy density does not necessarily mean a high-power density indicates materials with low energy density may also have a high-power density. Power density describes the rate at which its energy can be put out (time rate of energy transfer) and is a measure of power output per unit volume.

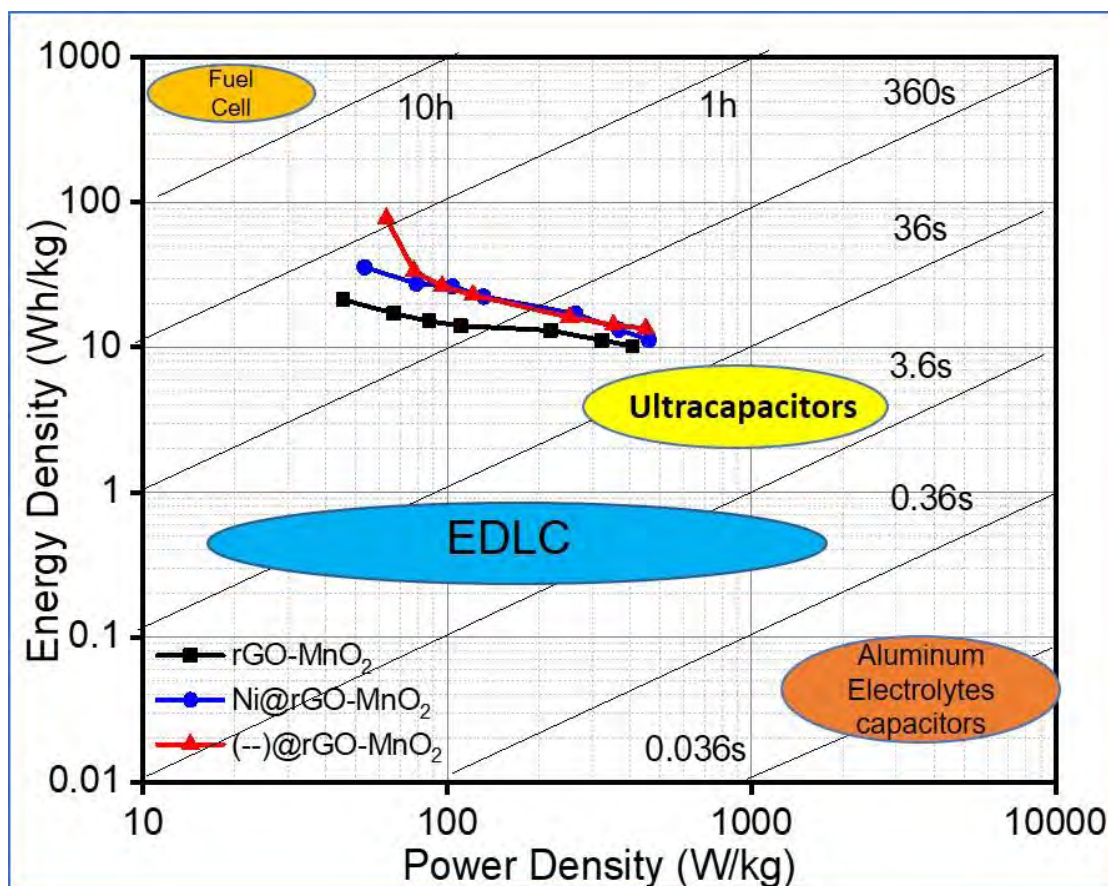


Figure 5.22: Ragone plot for energy density and power density of Ni-based nanomaterials.

If a system has a high-power density, then it can output large amounts of energy based on its volume. Thus, hollow and porous (--)-@rGO-MnO₂ nanocomposite with the highest value of energy density (77 Wh/kg) as well as power density (63 W/kg) will act better in supercapacitors applications. Typically having a high energy density goes along with a low power density. An object with a high energy density, but low power density can perform work for a relatively long period of time (e. g. mobile phone). Generally, a high-power density material discharge energy faster than a low power density material. Since they release their energy quickly, high power density systems can also recharge quickly. This makes a system with a high-power density ideal. Generally, a capacitor has a higher power density than a battery. The energy density of the battery, however, is higher than the energy density of the capacitor [47].

5.4.3 EIS analysis

The fundamental behavior of electrode materials for supercapacitors is investigated by using EIS [24,46], which not only provides useful information on the electrochemical frequency of the system but also allows for the measurement of redox reaction resistance and equivalent series resistance of the electrode [46, 51]. The Nyquist impedance plots for pure rGO-MnO₂, Ni@rGO-MnO₂, hollow and porous (--)@rGO-MnO₂ are shown in Fig. 5.23. The plots are composed of a very small arc in the high-frequency region and of a line in the low-frequency region. At the very high-frequency intercepts for all three electrodes are almost the same, indicating that they have the same combinational resistance of ionic resistance of the electrolyte, intrinsic resistance of substrate, and contact resistance at the active material/current collector interface (R_e). The semicircle in the high-to-medium-frequency region corresponds to a parallel combination of charge transfer resistance (R_{ct}) and the double-layer capacitance (C_{dl}) on the grain surface, [46-47, 51-53]. The black line representing rGO-MnO₂ shows a larger semi-circle than the red and blue line for Ni@rGO-MnO₂ and (--)@rGO-MnO₂, respectively revealing a decreased resistance and high conductance of the composite after the addition of MnO₂ to Ni@rGO core-shell and (--)@rGO coreless hollow crumpled structure which suggests that Ni NPs and MnO₂ has aided the matrix via the inherent pseudocapacitive nature[24,54]. This owes to the unique porous structure of (--)@rGO-MnO₂, which facilitates a faster cation insertion/extraction process into/from MnO₂ lattice[52-53]. Furthermore, the 45° sloped portions at the mid-frequency region is the typical warburg resistance reflecting the ion diffusion behavior of the electrolyte. The smaller the warburg region, the lower the electronic transport resistance, less obstruction for ion diffusion and better charge propagation behavior [46,51-52]. As shown in the inset of Fig. 5.23, all the electrode has a smaller Warburg region, which presents a minor Warburg resistance. It implies that the highly porous graphene nanosphere with well-decorated MnO₂ on the surface is able to facilitate the penetration of electrolyte, leading to fast diffusion of electrolyte into the pores of MnO₂. Thus, the unique structure of (--)@rGO-MnO₂ hybrid facilitates small R_{ct} , diffusive resistance and Warburg resistance, which can make for fast electron and ion transport. Thus, the (--)@rGO-MnO₂ electrode could show good charge propagation behavior and ideal supercapacitive performance.

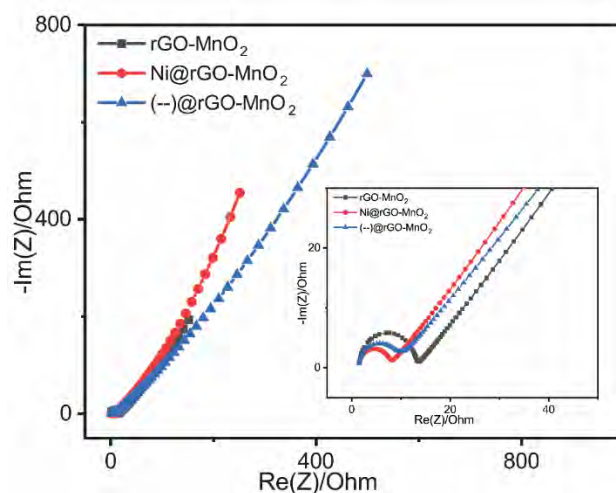


Figure 5.23. Nyquist plots of the pure rGO-MnO₂, Ni@ rGO-MnO₂, and (--)@rGO-MnO₂ electrodes.

The R_{ct} values, which are equal to the diameter of the semicircle [46, 51-52, 55-56], have the order Ni@ rGO-MnO₂ < (--)@rGO-MnO₂ < rGO-MnO₂. R_{ct} of the Ni@ rGO-MnO₂ composite electrode is approximately half that of the rGO-MnO₂ electrode and slightly larger than that of the (--)@rGO-MnO₂ electrode. This result may be due to the addition of the high surface area of and crumpled and stack free structure Ni@ rGO-MnO₂ and the porous and hollow structure of (--)@rGO-MnO₂, which enhances the conductivity of the composites. Additionally, the Ni NPs with MnO₂ prevent the aggregation of the graphene sheets, and the graphene sheets overlap each other to form a conductive network in the composites. The obtained values of R_s , C_{dl} , R_{ct} , were calculated from the complex nonlinear least-squares (CNLS) fitting of the experimental impedance spectra and are presented in Table –5.15

Table 5.15: The obtained values of R_s , C_{dl} , C_p , R_{ct} for Ni-based nanomaterials

	R_s (Ohm)	R_{ct} (Ohm)	C_{dl} (μ F)	C_p (F)
rGO-MnO ₂	1.4	11.5	0.09	0.03
Ni@rGO-MnO ₂	1.4	6.1	0.18	0.007
(--)@rGO-MnO ₂	1.4	7.5	0.25	0.008

As an equivalent circuit model, the following Randles circuit can be proposed

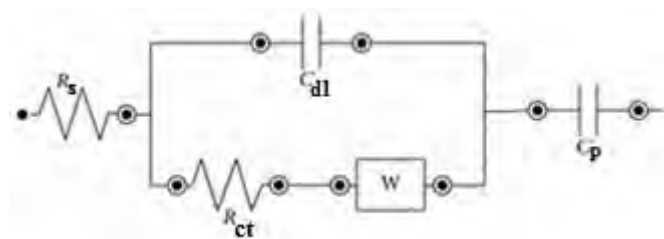


Figure 5.24: Randles circuit representing the equivalent circuit for the nanocomposites under experiment.

where, R_s represents electrolyte resistance, C_{dl} stands for the electrical double layer that is formed on the interface between the electrode and its surrounding electrolyte as ions from the solution adsorb onto the electrode surface, C_p represents pseudocapacitance, R_{ct} represents the charge transfer resistance from kinetically controlled electrochemical reaction and W represents the warburg impedance arises from diffusion [24,51,57]

5.4.4 Cycle stability of $(-)-@rGO-MnO_2$ from $Ni@rGO-MnO_2$

The cycle stability of the $(-)-@rGO-MnO_2$ was evaluated by repeating the GCD test in the potential range of -0.1 to 0.8 V vs. Ag/AgCl at a current density of 5 A/g for 1000 cycles. The GCD curve of first (left) and last (right) 5 cycles of the GCD test of the $(-)-@rGO-MnO_2$ for 1000 cycles and showed uniform structure retain after 1000 cycles as like first 5 cycles. For the first 30 cycles, the specific capacitance was calculated with an interval of 5 cycles. It showed that the $rGO-MnO_2$, $Ni@rGO-MnO_2$ and $(-)-@rGO-MnO_2$ retains 96.51%, 100.41% and 136.11% specific capacity respectively after 30 cycles, showed in Fig. 5.25(c). After 1000 cycles, the capacitance still remained 97.2% of the initial capacitance, demonstrating good electrochemical stability of the synthesized $(-)-@rGO-MnO_2$ by the exclusion of Ni NPs, shown in Fig. 5.25(d). Thus, the $(-)-@rGO-MnO_2$ shows maximum retention capacity. The preliminary increase in the capacitance can be explained as a result of complete exposure of the active sites of the electrode to the electrolyte after repeated charging-discharging. The specific and the interfacial capacitance values are decreased by a certain amount with increasing number of cycles due to the loss of active material caused by dissolution and/or detachment during the early charging and discharging cycles in the electrolyte or oxygen evolution [24,46,56].

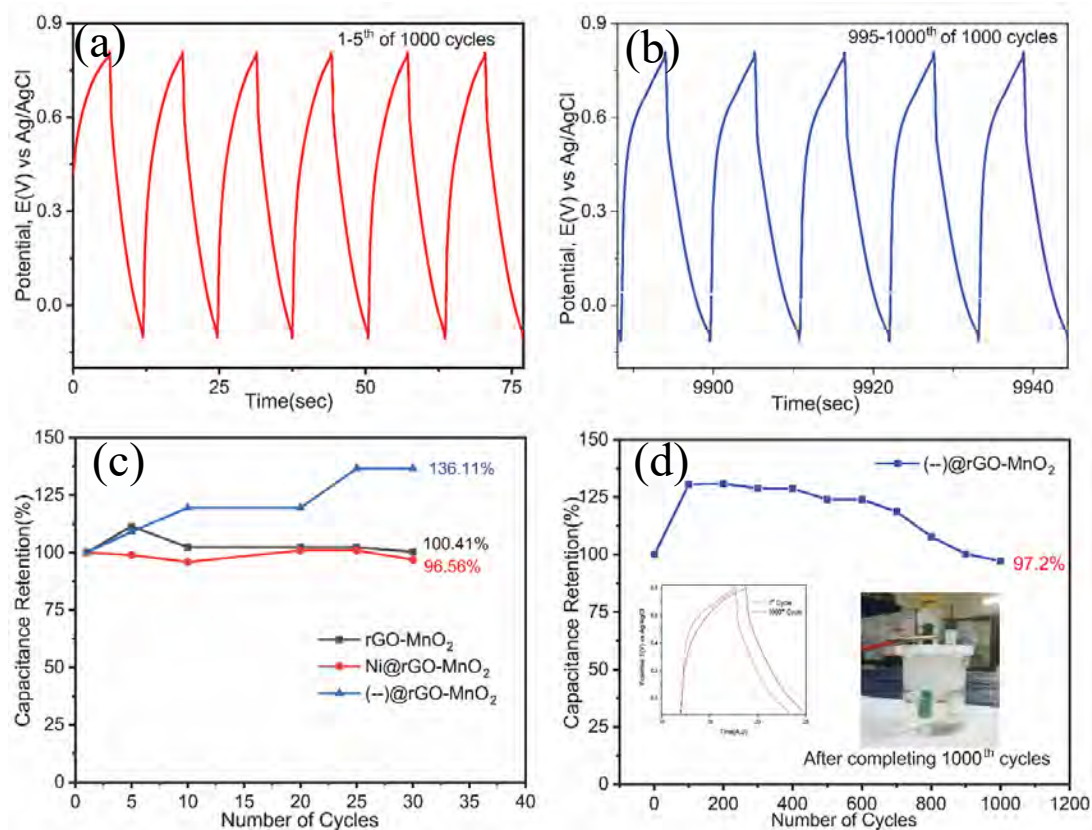


Fig. 5.25: The GCD curve of (-)-@rGO-MnO₂ (a) first 5 cycles (left) and (b) last (right) 5 cycles for 1000 and (c) capacitance retention profile of the rGO-MnO₂, Ni@rGO-MnO₂ and (-)-@rGO-MnO₂ within -0.1 to 0.8 V at 5 A/g for (d) (-)-@rGO-MnO₂ within -0.1 to 0.8 V at 5 A/g for 1000 cycles.

5.5 Investigation of electrochemical performance of iron oxide-based nanocomposite

5.5.1 CV and GCD of rGO, Fe₃O₄@rGO and hollow crumpled (--)@rGO

The cyclic voltammetry is performed to obtain electrochemical properties of rGO, core-shell Fe₃O₄@rGO nanocomposite and hollow (--)@rGO nanocomposite, are shown in Fig. 5.26(a), (c) and (e) within the potential range from -0.15 to 0.75 V with various scan rates (2, 5, 10, 20 and 50 mV/s) in 0.5M Na₂SO₄ solution respectively. Fig. 5.26(a) indicates that the complete reduction of graphene oxide into graphene using ammonia and hydrazine solution and sodium borohydride. Fig. 5.26(c) is the slightly symmetric deform rectangular in shape that may affect the pseudocapacitance of iron oxide whereas Fig. 5.26(e) is exact rectangular in shape, indicating an excellent capacitive behavior of (--)@rGO than Fe₃O₄@rGO, indicating an excellent capacitive behavior due to only electrochemical capacitance. However, curves show that with increasing scan rates the rectangular shape is not deformed for hollow crumple (--)@rGO nanosphere. It may be for high porosity and crumpling of graphene hollow structure compare to graphene sheet for adsorption and desorption electrolyte ions with a facilitating highly porous surface and defend the agglomeration of rGO for EDL formation [59].

The GCD curves of rGO, core-shell Fe₃O₄@rGO nanocomposite and hollow (--)@rGO nanocomposite at different current densities respectively are shown in Fig. 5.26(b), (d) and (f) within the potential range from -0.15 V to 0.75 V with various. Accordingly, the GCD curves at various current densities as shown in Fig. 5.26(b), (d) and (f) are symmetric triangles without an obvious potential drop (IR drop), confirming the characteristic EDLC in addition with pseudocapacitance for core-shell Fe₃O₄@rGO nanocomposite. The capacitance values of rGO, core-shell Fe₃O₄@rGO and hollow (--)@rGO nanocomposite are calculated for various current densities of 0.1, 0.15, 0.2, 0.25, 0.5, 0.7, and 0.9 A/g respectively shows in Fig. 5.27. The highest capacitance values at the current density of 0.1 A/g for rGO sheet, Fe₃O₄@rGO, (--)@rGO are found 81, 365 and 259 F/g, respectively.

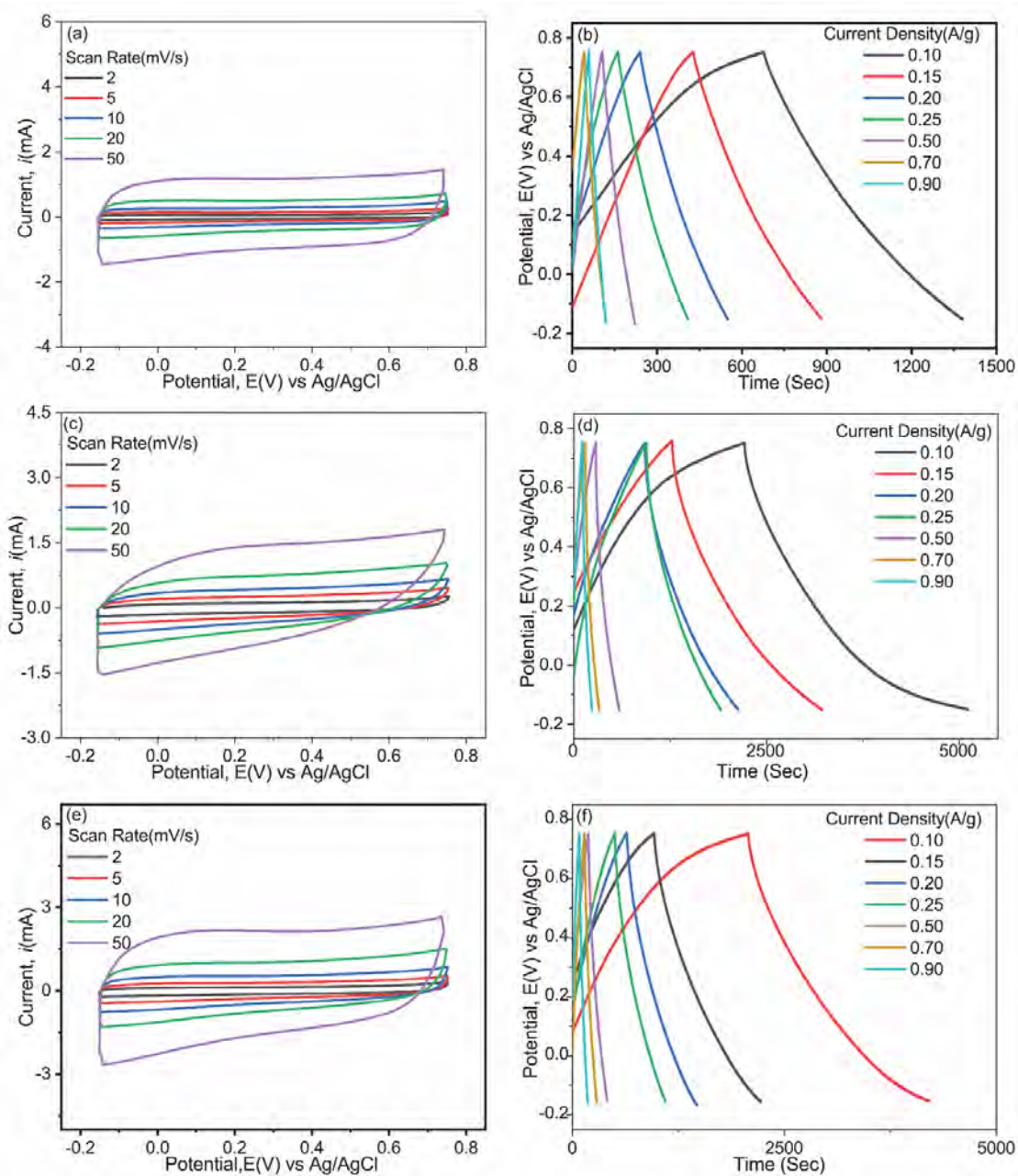


Figure 5.26: CV curves (a,c,e) within potential window -0.15 to 0.75V at different scan rates (2, 5, 10, 20, and 50 mV/s) and GCD curves (b,d,f) at different current densities (0.1, 0.15, 0.2, 0.25, 0.5, 0.7 and 0.9 A/g) of rGO, Fe₃O₄@rGO, (-)-@rGO, respectively.

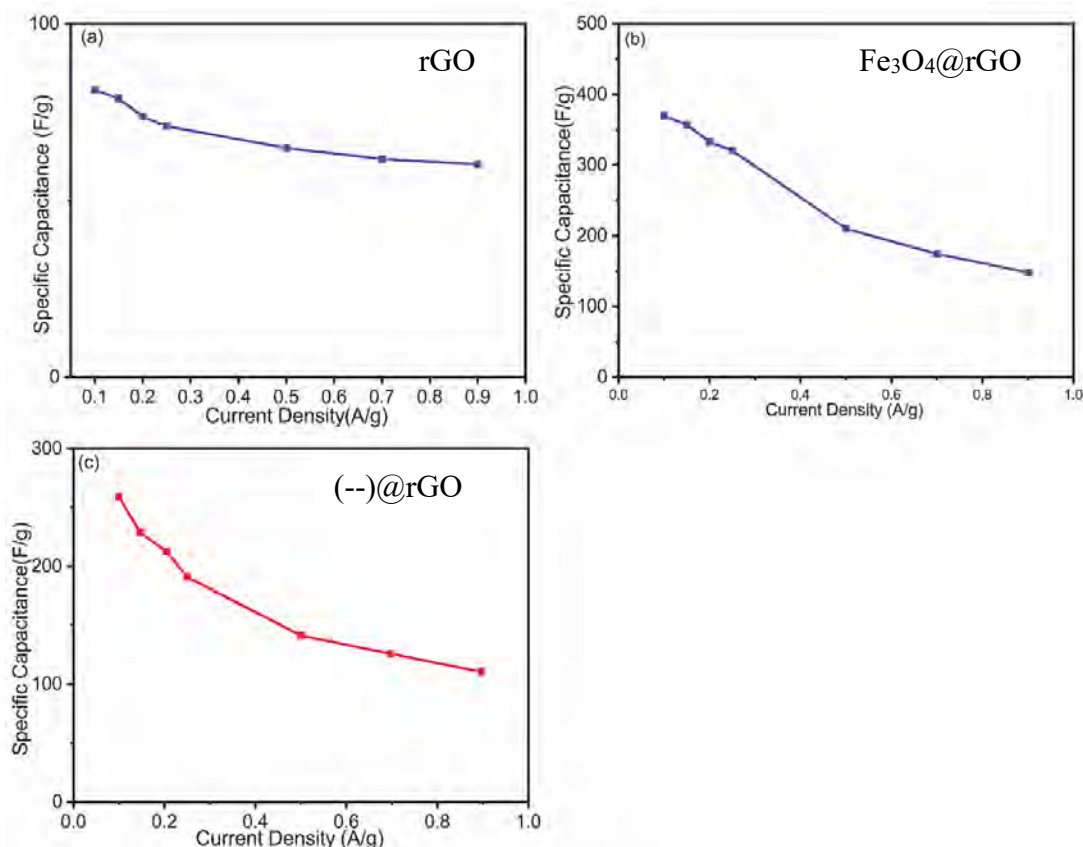


Figure 5.27: C_{sp} (F/g) of (a-c) at different current densities (0.1, 0.15, 0.2, 0.25, 0.5, 0.7 and 0.9 A/g) of , core-shell $\text{Fe}_3\text{O}_4@\text{rGO}$, and $(--)\text{rGO}$ within potential window -0.15 to 0.75 V, respectively.

The high surface area of rGO and Fe_3O_4 nanoparticles due to its shape and conductivity rGO provides better access to electrolytes by facilitating to significantly reduce large stacks of graphene sheets and OH^- soaking in bulk materials [59]. So $\text{Fe}_3\text{O}_4@\text{rGO}$ nanocomposites represent a promising way to increase the conductivity over poor conductivity of metal-oxide due to the incorporation of highly conductive rGO and promoted the transportation of electrical charges occurs within the metal oxide nanoparticles and also absorption-desorption of charges on the rGO surface. In $(--)\text{rGO}$ hollow, the graphene layer has high crumping and aging which is beneficial for forming more double layers with different sides hence the capacitive performance is increased compared to the rGO sheet.

5.5.2 CV and GCD of rGO-MnO₂ nanocomposite

The CV curve of rGO-MnO₂ composite is shown in Fig. 5.28(a) at various scan rates (2, 5, 10, 20 and 50 mV/s) within the potential range from -0.15 to 0.75 V were studied in 0.5 M Na₂SO₄ solution.

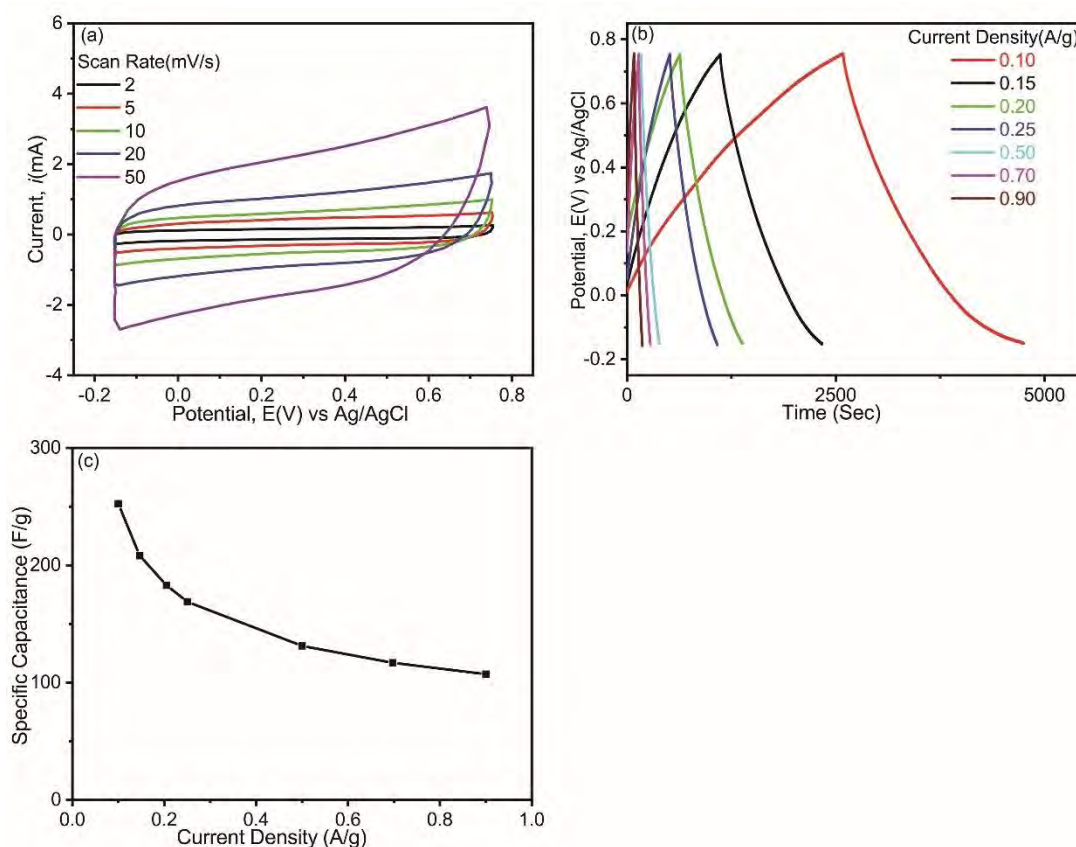


Figure 5.28: (a) CV curves at different scan rates (2, 5, 10, 20 and 50 mV/s) (b) GCD curves at different current densities (0.1, 0.15, 0.2, 0.25, 0.5, 0.70, and 0.9 A/g) (c) C_{sp} (F/g) at different current densities of rGO-MnO₂ within -0.15 to 0.75 V.

The rGO-MnO₂ nanocomposite shows a quasi-rectangular shape with a large area indicating the capacitance is probably due to the combined EDL from rGO and pseudocapacitance contribution from MnO₂ which is depicted in Fig.5.28(a). This means that rGO-MnO₂ nanocomposite may give a better specific capacitance value compared to rGO as the specific capacitance is proportional to the area under the rectangular segment of the CV curve.

The highest specific capacitance value was calculated from the GCD curve of rGO-MnO₂ nanocomposite 252 F/g at current density 0.1 A/g respectively. The GCD curve of rGO-MnO₂ nanocomposite at current densities 0.1, 0.15, 0.2, 0.25, 0.5, 0.7, and 0.9

A/g are shown in Fig. 5.28(b). The GCD curves of rGO-MnO₂ are almost symmetrical triangle. rGO-MnO₂ composite with enhanced electrical conductivity for the incorporation of rGO, promote fast charging and discharging of the MnO₂ nanostructure in the electrolyte and preserving the high-surface-area interface between the MnO₂ nanomaterials and the electrolyte which allow the active electrolyte ions (alkali ions) to intercalate and de-intercalate more easily and sufficiently. From the discharging time the calculated capacitance values of rGO-MnO₂ are 252, 208, 183, 168, 131, 116, and 107 F/g at current density of 0.1, 0.15, 0.2, 0.25, 0.5, 0.7, and 0.9 A/g respectively are shown in Fig. 5.28(c). Thus, the electrochemical performance of rGO-MnO₂ nanocomposite is little high compared to rGO in capacitance is ascribed to the high inner charge storage and inefficient ion transportation ions due to compact structure of composite and both contribution of EDLC and pseudocapacitance.

5.5.3 CV and GCD of Fe₃O₄@rGO-MnO₂ nanocomposite

The CV characteristics curves of Fe₃O₄@rGO-MnO₂ composite is shown in Fig. 5.29(a) within the potential range from -0.15 to 0.75 V at different scan rates (2, 5, 10, 20 and 50 mV/s) in 0.5 M Na₂SO₄ solution, respectively. For core-shell Fe₃O₄@rGO-MnO₂ nanocomposite shows smooth symmetric quasi-rectangular shape in Fig. 5.29(a). It is cleared from CV curves that along the axis without obvious redox peaks even with the introduction of Fe₃O₄ nanoparticles, indicating the good capacitive behavior of electrodes for core-shell Fe₃O₄@rGO-MnO₂ nanocomposite. The capacitance is probably due to the combined role of the electrical double layer and pseudocapacitance contribution. The shape of the CV curve was still markedly rectangular in shape, even at high scan rates. No redox peak has appeared within the potential window ensured that the iron oxide is in core and manganese oxide over Fe₃O₄@rGO core-shell structure with flawless crystalline shape may responsible for redox reaction during charging-discharging that may act as a good contributor in overall capacitance.

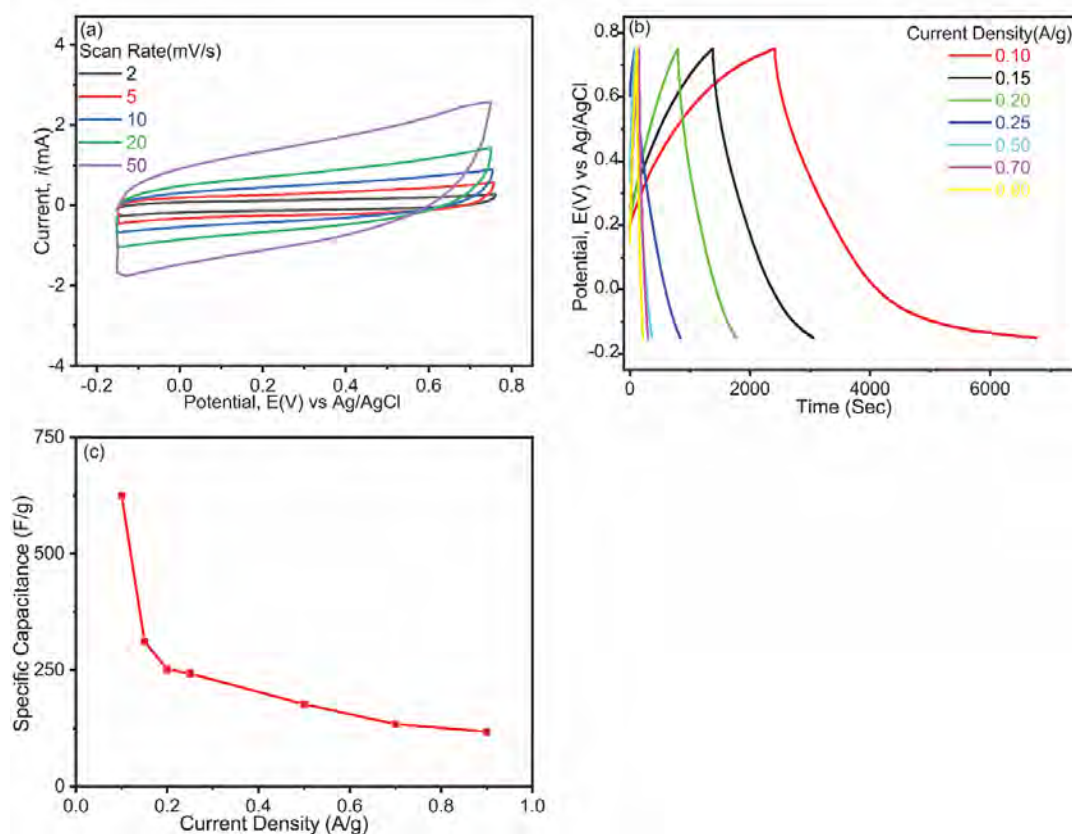


Figure 5.29: (a) CV curves at different scan rates (2, 5, 10, 20 and 50 mV/s) (b) GCD curves at different current densities (0.1, 0.15, 0.2, 0.25, 0.5, 0.7 and 0.9 A/g) (c) C_{sp} (F/g) at different current densities within potential window -0.15 to 0.75 V of Fe₃O₄@rGO-MnO₂.

The GCD was performed for different current densities (0.1, 0.15, 0.2, 0.25, 0.5, 0.7 and 0.9 A/g) are shown in Fig. 5.29(b), for studies electrochemical capacitance behavior of synthesizes core-shell Fe₃O₄@rGO-MnO₂ nanocomposite by incorporation of Fe₃O₄ in core of rGO-MnO₂. The shape of the curve is symmetric triangles without obvious potential drop (IR drop) with a curvature at the end of discharge for low current density which indicates internal redox reaction of electrode material [28] which contribute to pseudocapacitance in addition with the characteristic electrical double layer capacitance. The calculated capacitance values 311, 251, 242, 176, 133, and 117 F/g of core-shell Fe₃O₄@rGO-MnO₂ nanocomposite at current density of 0.1, 0.15, 0.2, 0.25, 0.5, 0.7 and 0.9 A/g, respectively, depicted at Fig. 5.29(c). The unique combination of Fe₃O₄ and rGO can facilitate transportation for electron, resulting in further boosting the electrochemical properties of the as-prepared Fe₃O₄@rGO-MnO₂ core-shell nanocomposite. As no obvious peak found in the CV which indicates that the

Fe_3O_4 is fully covered with rGO and incorporation of Fe_3O_4 in core improves the stacks of rGO with numerous wrinkles and folds can induce high electronic conductivity and more reactive sites. Therefore, during the charge-discharge process, ion and charge transport is faster, may favor the cycle life stability [59]. Combine effect of pseudocapacitance arising from Fe_3O_4 and MnO_2 sites and the EDLC contribution by the rGO which is initiated by incorporation of MnO_2 with crystalline shape over the Fe_3O_4 @rGO core-shell structure. Needle and rod-like mixed shape MnO_2 nanoparticles on core-shell Fe_3O_4 @rGO may be preserved the high-surface-area interface between the MnO_2 nanomaterials and the electrolyte that makes the composite highly accessible for electrolyte ions for adsorption-desorption for EDLC along with pseudocapacitance introduce from redox reaction of MnO_2 and Fe_3O_4 sites in aqueous electrolyte. Hereby, the dual charge-storage mechanism, low stacking and high accessible surface area benefits for the high capacitance of the Fe_3O_4 @rGO- MnO_2 core-shell nanocomposite.

5.5.4 CV and GCD of hollow crumpled (--)@rGO- MnO_2 nanocomposite

The CV of hollow (--)@rGO- MnO_2 nanocomposite is shown in Fig. 5.30(a) within the potential range from -0.15 to 0.75 V at different scan rates of (2, 5, 10, 20 and 50 mV/s) in 0.5 M Na_2SO_4 solution. The CV curve of hollow crumpled (--)@rGO- MnO_2 nanocomposite shows the nearly rectangular-like shape within the potential window, indicating the ideal capacitive behavior at all scan rates. However, the current response of hollow crumpled (--)@rGO- MnO_2 nanocomposite was much higher which was ascribed to the unique hollow crumpled structure with rod shape pseudocapacitive MnO_2 . However, curves show that with increasing scan rates the rectangular shape is not deformed that may be owing for high porosity of nanostructure for adsorption and desorption electrolyte ions which can be attributed to fast electro-sorption of Na^+ cation and the subsequent quick reversible faradaic process proceeding of MnO_2 from hollow (--)@rGO- MnO_2 nanocomposite[46].

In Fig.5.30(b), the GCD curve of hollow crumpled (--)@rGO- MnO_2 nanocomposite at various current densities are shown. The GCD curves of (--)@rGO- MnO_2 are tainted symmetrical to its corresponding discharge counterpart with a slight curvature at low current density, indicating the materials undergoing certain internal oxidation-reduction[24] and the diffusion of ions from the electrolyte can gain access to almost all available pores of the electrode, leading to a complete insertion reaction which is

responsible for high capacitance which is probably due to the combination of EDLC from rGO and pseudo-capacitance from the redox reaction of MnO_2 .

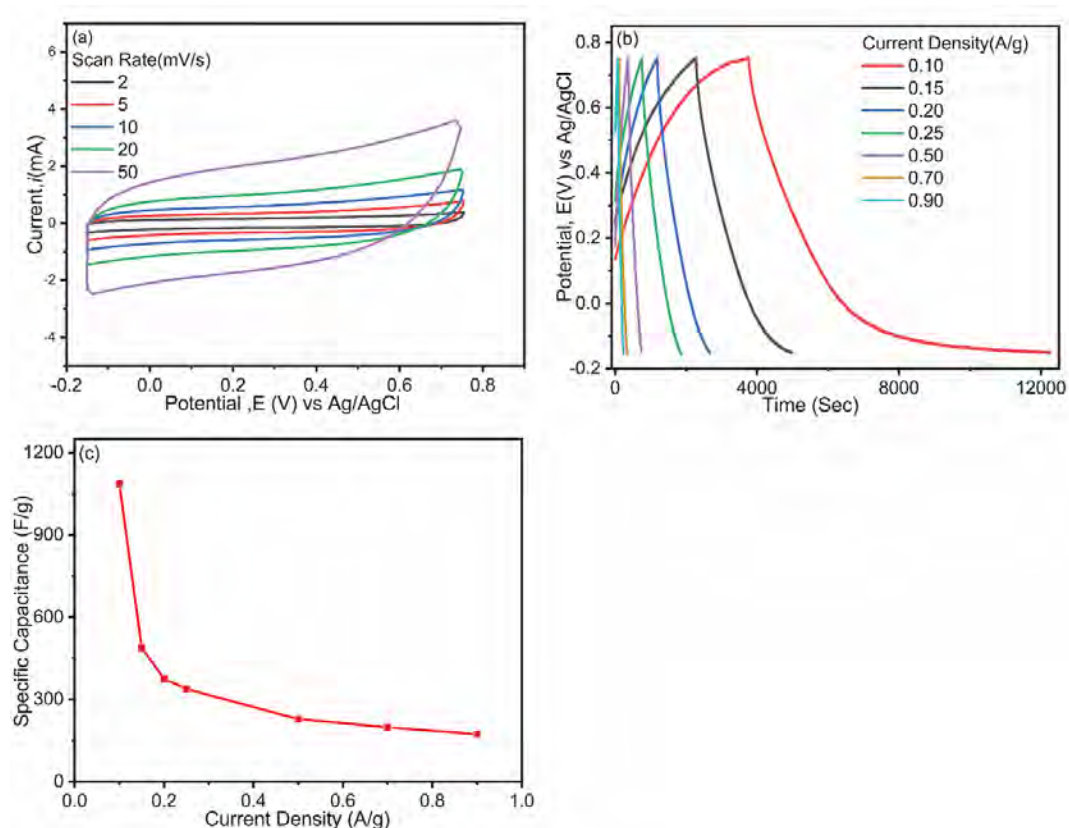


Figure 5.30: (a) Cyclic voltammograms of rGO-MnO_2 at various scan rates within -0.15 V to 0.75 V (b) Galvanostatic charge-discharge curves at different current densities (0.10, 0.15, 0.20, 0.25, 0.50, 0.70, and 0.90 A/g) and (c) specific capacitance as a function of current density for rGO-MnO_2 .

The highest specific capacitance value was found from the GCD curve of hollow crumpled rGO-MnO_2 nanocomposite 1086 F/g at current density 0.1 A/g. The calculated specific capacitances are 1086, 488, 375, 338, 228, 198 and 173 F/g at different current densities (0.1, 0.15, 0.2, 0.25, 0.5, 0.7, and 0.9 A/g), shown in Fig 5.30(c). The improved electrochemical performance of rGO-MnO_2 electrode may be attributed to the unique spongy and hollow crumpled structure of graphene with combination of faradic redox between MnO_2 and Na_2SO_4 electrolyte according to Eq. 5.1. As the effective surface area can be reduced by horizontal aggregation of graphene to current collector which is hindered for electrons and ion transport that influence the electrochemical properties. By exclusion of Fe_3O_4 template from core the

graphene can maintain their spongy and hollow crumpled structure with more aged and accessible surface area. Crumpling structure of rGO having more disordered microstructure which leads to pocket-like void space. Crumple graphene don't tightly pack due to uneven size distribution and orientations with smaller uniformly distributed inside and between and large segregated voids less dense which should be more favorable for ionic flow and electron transport for enhancing the electrochemical properties of supercapacitors [73]. The nanorods and needle shape MnO_2 on spongy and hollow crumpled graphene retain after being processed to fabricate supercapacitor electrodes compared with MnO_2 on planar graphene sheets. As the hollow crumpled ($--$)@rGO- MnO_2 nanocomposite can significantly reduce large stacks of rGO and makes more available surface area accessible for electrolyte ion adsorption plays an important role in enhancing the electron transfer rate which facilitates electrolyte to access to the electrochemical sites and provides short diffusion path lengths for adsorbing ions with improved electrical conductivity [46].

5.6 Comparative investigation for iron oxide-based nanomaterials on electrochemical performances

5.6.1 CV and GCD analysis

To compare the inconsistency of electrochemical performance of ($--$)@rGO- MnO_2 due to inclusion and exclusion of core Fe_3O_4 nanoparticles with that of the Fe_3O_4 @rGO- MnO_2 and rGO- MnO_2 electrodes, CV and GCD was performed in 0.5 M Na_2SO_4 within a potential range of -0.15 to 0.75 V vs Ag/AgCl. The nature of the CV curve of hollow ($--$)@rGO- MnO_2 nanocomposite actual rectangular which indicates excellent capacitive behavior of over Fe_3O_4 @rGO- MnO_2 and rGO- MnO_2 nanocomposite, which is probably due to the combination of EDLC from hollow crumple rGO and pseudocapacitance from the redox reaction of MnO_2 nanorods (shown in Fig. 5.31). Larger rectangular area than that of Fe_3O_4 @rGO- MnO_2 but less than rGO- MnO_2 nanocomposite, implying that the ($--$)@rGO- MnO_2 nanocomposite possesses higher capacitance may be for dual charge storage mechanism. Core-shell Fe_3O_4 @rGO- MnO_2 nanocomposite shows symmetric quasi-rectangular shape along the axis without obvious redox peaks even with the introduction of Fe_3O_4 NPs.

The GCD measurements of rGO-MnO_2 , $\text{Fe}_3\text{O}_4@\text{rGO-MnO}_2$, and $(-)\text{@rGO-MnO}_2$ nanocomposite were carried out at current density 0.1 A/g, as shown in Fig. 5.31(b). The GCD curves of $(-)\text{@rGO-MnO}_2$ are tainted symmetrical than that of $\text{Fe}_3\text{O}_4@\text{rGO-MnO}_2$ and rGO-MnO_2 to its corresponding discharge counterpart with a curvature at 0.1 A/g current density, indicating the materials undergoing certain internal oxidation-reduction [24] and the diffusion of ions from the electrolyte can gain access to almost all available pores of the electrode, leading to a complete insertion reaction to all pores of electrode materials which is responsible improve the charge-discharge time ratio which is probably due to the combination of double-layer capacitance from rGO and pseudo-capacitance from the redox reaction of MnO_2 . The comparative CV and GCD curves of $(-)\text{@rGO-MnO}_2$, $\text{Fe}_3\text{O}_4@\text{rGO-MnO}_2$, and rGO-MnO_2 nanocomposite at scan rate 5 mV/s and 0.1 A/g are showed in Fig. 5.31(a) and (b).

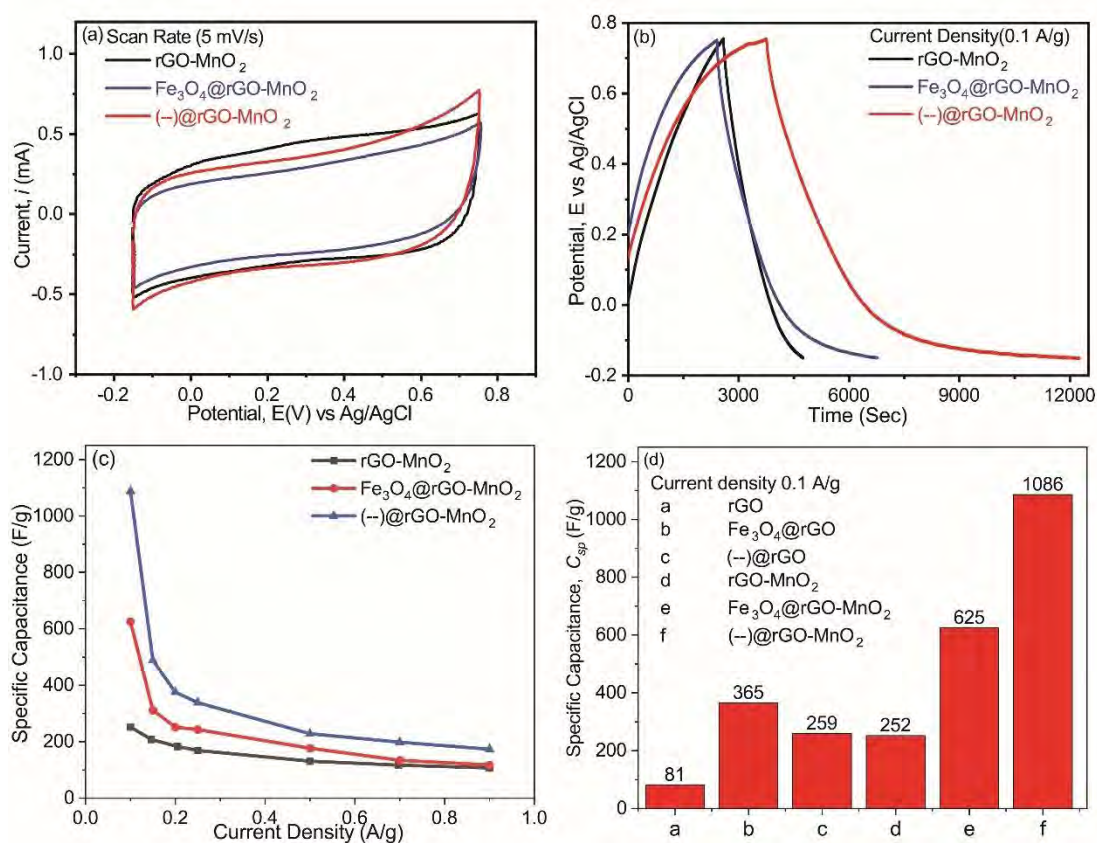


Figure 5.31: Comparative (a) CV (b) GCD curves and (c and d) specific capacitances with current densities of rGO-MnO_2 , $\text{Fe}_3\text{O}_4@\text{rGO-MnO}_2$, and $(-)\text{@rGO-MnO}_2$ nanocomposite.

The calculated C_{sp} are shown in Fig. 5.31(c) at different current densities 0.1, 0.15, 0.2, 0.25, 0.5, 0.7 and 0.9 A/g. The highest C_{sp} are calculated to be, 252, 625 and 1086 F/g at 0.1 A/g rGO-MnO₂, Fe₃O₄@rGO-MnO₂ and (--)@rGO-MnO₂, respectively. The (--)@rGO-MnO₂ nanocomposite exhibits a much longer charge/discharge time (of about 2 times) than that of the rGO-MnO₂ nanocomposite. The compact structure of the MnO₂ solids on the rGO sheet leads to the poor specific capacitance of rGO-MnO₂ nanocomposite significantly restricts the electron transfer, with a low accessible surface area and less contact of electrolyte ion with active materials due to horizontal alignment of graphene stacks can hinder electron and ions resulting in poor electrochemical performance. The higher specific capacitance of crumpled hollow (--)@rGO-MnO₂ nanocomposite can be attributed to the synergetic effect of high conductivity of spongy hollow rGO and redox process rod-shaped structure of MnO₂ nanocomposite with unique features ahead in by exclusion of Fe₃O₄ template from core the graphene can maintain their spongy and hollow structure after being processed to fabricate supercapacitor electrodes. As compared with MnO₂ on planar graphene sheets, the hollow (--)@rGO-MnO₂ nanocomposite can significantly reduce large stacks of rGO and makes more available surface area accessible for electrolyte ion adsorption plays an important role in enhancing the electron transfer rate which may be made the graphene shells fully wetted by electrolyte which facilitates electrolyte to access to the electrochemical sites and provides short diffusion path lengths for adsorbing ions with improved electrical conductivity. Also, it may be allowing the active electrolyte ions (Na⁺) to intercalate and de-intercalate more easily and sufficiently from the electrolyte [46].

5.6.2 Determination of energy density and power density

The energy density (E) and power density (P) of the prepared materials were calculated from the known highest capacitance value of the sample obtained either from CD curves using the Eq. 3.5 and 3.6, are shown in the Fig. 5.33. Thus, the nanocomposite, (--)@rGO-MnO₂ with the highest capacitance value (1048 F/g), among them as prepared nanomaterials will store greater the amount of energy in a small amount of volume than that of all other prepared nanomaterials showing the good electrochemical properties. The ranking of power density of synthesized materials Ni@rGO-MnO₂(55 W/kg) > (--)@rGO-MnO₂(51 W/kg) > rGO-MnO₂(46 W/kg) and energy density

(--) rGO-MnO_2 (122.28 Wh/kg) > Ni @rGO-MnO_2 (67.26 Wh/kg) > rGO-MnO₂(28.39 Wh/kg) . This indicates that this nanocomposite could be a good electrode candidate for supercapacitors. It may be noted that, a high energy density does not necessarily mean a high-power density. Power density describes the rate at which its energy can be put out (time rate of energy transfer) and is a measure of power output per unit volume.

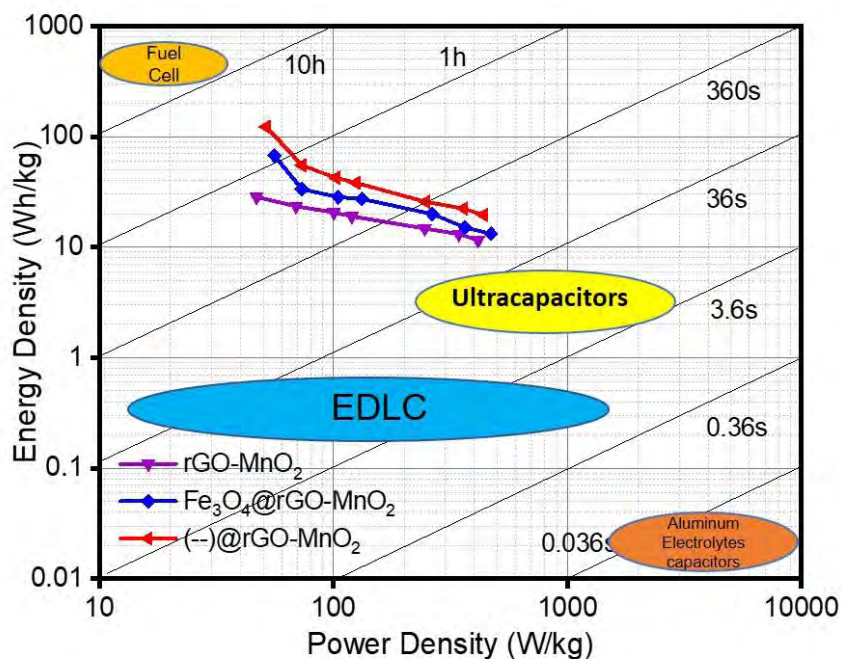


Figure-5.33: A schematic representations of Power density and energy density of synthesized nanomaterials.

If a system has a high-power density, then it can output large amounts of energy based on its volume. Thus, (--) rGO-MnO_2 with the highest energy density (122 Wh/kg) and power density (51 W/kg) will act better in supercapacitors applications. Typically having a high energy density goes along with a low power density. An object with a high energy density, but low power density can perform work for a relatively long period of time (e. g. mobile phone). Generally, a high-power density material discharge energy faster than a low power density material. Since they release their energy quickly, high power density systems can also recharge quickly. This makes a system with a high-power density ideal. Generally, a capacitor has a higher power density than a battery. The energy density of the battery, however, is higher than the energy density of the capacitor.

5.6.3 EIS Analysis

EIS was further conducted from 0.1 to 1 MHz with an amplitude of 10 mV to investigate the electrochemical property of obtained (a) rGO-MnO₂ (b) Fe₃O₄@rGO-MnO₂ and (c) (--)@rGO-MnO₂ electrodes, as shown in Fig. 5.32.

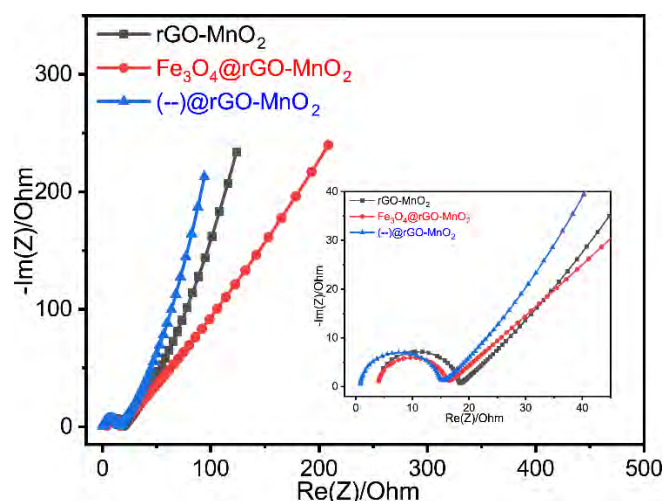


Figure 5.32: Nyquist plots of the (a) rGO-MnO₂ (b) Fe₃O₄@rGO-MnO₂ (c) (--)@rGO-MnO₂.

In the Nyquist plots, there is a semicircle in the high-frequency region and a straight line in the low-frequency region, which are related to the charge transfer resistance (R_{ct}) and the capacitive behavior of the electrode [46,51-52]. The R_{ct} values, which are equal to the diameter of the semicircle [46,51-52,55-56], have the order (--)@rGO-MnO₂ < Fe₃O₄@rGO-MnO₂ < rGO-MnO₂. It is noted that the (--)@rGO-MnO₂ and Fe₃O₄@rGO-MnO₂ shows much the lower R_{ct} (about 10.91 Ω and 11.80 Ω) than that of rGO-MnO₂ (about 14.27 Ω), due to the in situ encapsulated graphene layer into the Fe₃O₄ with well-decorated MnO₂ and in case of well-defined MnO₂ embedded hollow crumpled graphene [(--)@rGO-MnO₂] with porous structure, which permits ultrafast electron transfer reaction kinetics. The straighter line at the low-frequency region for (--)@rGO-MnO₂ tends approximately toward the vertical compared to rGO-MnO₂, further confirming the ideal capacitive behavior of the (--)@rGO-MnO₂ electrode [46,51]. The finite slope of a low-frequency straight line for (--)@rGO-MnO₂ electrode demonstrates a good capacitive behavior without diffusion limitation. represents the diffusive resistance of electrolyte in electrode pores or cation diffusion in the host materials [46,51-52]. The more inclined line at the high-frequency region for rGO-

MnO₂ revealing a decreased resistance and high conductance of the (--)@rGO-MnO₂ after the exclusion of Fe₃O₄ from core and addition of MnO₂ over hollow crumpled graphene has aided the matrix via the inherent pseudocapacitive nature[24,60]. Furthermore, at very high frequencies, the intercept of the real part (Z) may be due to the combination of the ionic resistance of the electrolyte, the intrinsic resistance of the active materials, and the contact resistance between the active materials and the current collector[55, 60], indicating that the three electrodes have same R_s values. The small portion of the curve with a 45° slope corresponds to the warburg resistance (Z_w) and is the result of the frequency dependence of the ion diffusion/transport from the electrolyte to the electrode surface [24,28,46,61]. The semicircle in the high-to-medium-frequency range corresponds to a parallel combination of the charge-transfer resistance (R_{ct}) and the double-layer capacitance [24,47]. The obtained values of R_s, C_{dl}, C_p, R_{ct}, were calculated from the fitting of the experimental impedance spectra and are presented in Table-5.16

Table 5-16: The obtained values of R_s, C_{dl}, C_p, R_{ct} for iron oxide-based nanomaterials

	R _s (Ohm)	R _{ct} (Ohm)	C _{dl} (μF)	C _p (F)
rGO-MnO ₂	3.73	14.27	0.0452	0.0124
Fe ₃ O ₄ @rGO-MnO ₂	3.93	11.80	0.1595	0.0677
(--)@rGO-MnO ₂	3.83	10.91	0.5112	0.0134

The AC impedance equivalent circuit is shown in the Fig. 5.33 . As an equivalent circuit model, the following Randles circuit can be proposed

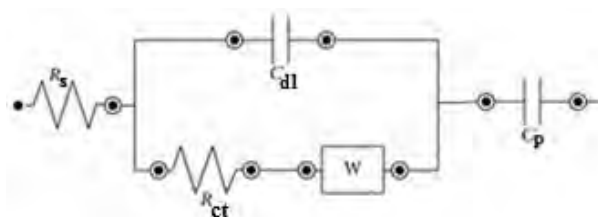


Figure 5.33: Randles circuit representing the equivalent circuit for the nanocomposites under experiment.

5.6.4 Cycle stability analysis of $(\text{--})@r\text{GO-MnO}_2$ from $\text{Fe}_3\text{O}_4@r\text{GO-MnO}_2$

The cycle stability of supercapacitors is important for practical applications. Figure.5.37 shows the cyclic stability of the $(\text{--})@r\text{GO-MnO}_2$ from $\text{Fe}_3\text{O}_4@r\text{GO-MnO}_2$ electrode, which was evaluated using a GCD test between -0.15 and 0.75 V (vs. Ag/AgCl) at the current density of 5 A/g for 1000 cycles. The capacitance only decreased by 3.55% of the initial capacitance after 1000 cycles, as shown in Fig. 5.34(c), demonstrating the excellent electrochemical stability of this material. The cycle stability of the composites may be attributed to the good conductivity of the graphene with a crumpled porous structure and to the compact and definite crystal structure of the manganese dioxide. Thus, the $(\text{--})@r\text{GO-MnO}_2$ shows maximum retention capacity.

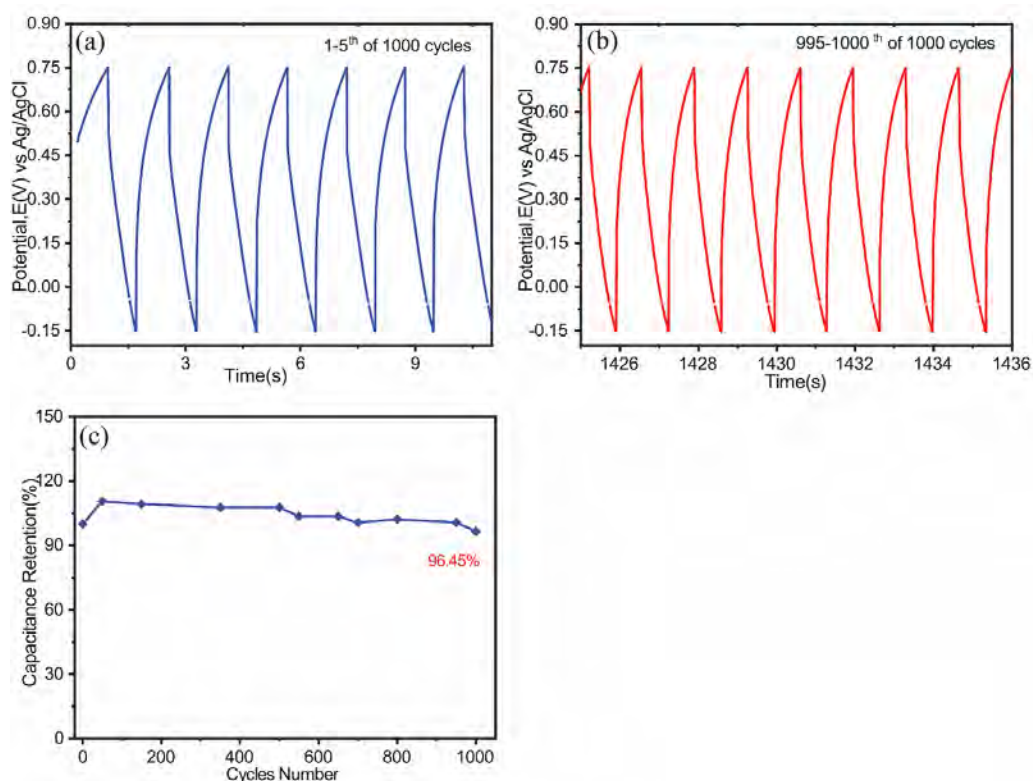


Figure 5.34: The GCD Curve of $(\text{--})@r\text{GO-MnO}_2$ a) first 5 cycles (left) and b) last (right) 5 cycles for 1000 cycles (c) Capacitance retention profile of the $(\text{--})@r\text{GO-MnO}_2$ within -0.15 to 0.75 V at 5 A/g for 1000 cycles.

The preliminary increase in the capacitance can be explained as a result of complete exposure of the active sites of the electrode to the electrolyte after repeated charging-discharging. [24,46,56].

A comparison study of the specific capacitance has been performed between the synthesized hollow crumple (--)@rGO-MnO₂ composite synthesized from Ni@rGO-MnO₂ and Fe₃O₄@rGO-MnO₂ in this study with others rGO-MnO₂ composites reported in the published literatures. Qian *et al.* synthesized graphene/MnO₂ composite by a polymer-assisted chemical reduction method in 2011 exhibited a high specific capacitance of 324 F/g in 1 M Na₂SO₄ electrolyte and also showed excellent long-term cycle stability [50]. Yang *et al.* synthesized reduced graphene nanosheet/urchin-like manganese dioxide (GNS/MnO₂) composite exhibits a maximum specific capacitance of 263 F/g and an excellent cycle life with a capacity retention of about 99% after 500 cycles. Zhang *et al.* reported in 2011 synthesized graphene/manganese dioxide (MnO₂) composite papers (GMCP) with the specific capacitance of the GMCP with the MnO₂ weight ratio of 24% (GMCP-24) reaches 256 F/g at a current density of 0.5 A/g and also showed good cycle stability [62]. Peng *et al.* reported a facile method of hybrid nanostructure of quasi-2D ultrathin MnO₂/graphene nanosheets, exhibiting high specific capacitances of 267 F/g at current density of 0.2 A/g and 208 F/g at 10 A/g and excellent rate capability and cycling stability with capacitance retention of 92% after 7000 charge/discharge cycles[63]. Ye *et al.* reported a facile method to prepare MnO₂/reduced graphene oxide (rGO) composites in 2013 and examined their applications as electrodes in flexible solid-state supercapacitors. The MnO₂/rGO composite electrodes exhibited a good electrochemical performance with an area capacitance of 14 F/cm² at 2 mV/s and excellent stability [64]. Huang *et al.* in 2015 reported a MnO₂/graphene nanocomposite synthesized through a water-reflux condenser system that shows the specific capacitance as high as 350 F/g at 1 A/g, which was almost two times higher than that of MnO₂ (163 F/g). Furthermore, the composite exhibited excellent long cycle life along with ~ 93% specific capacitance retained after 5000 cycle tests [65]. Wen *et al.* proposed a facile method to prepare the MnO₂-graphene composite in 2015 with a sandwich structure retained a capacity of 752 mAh/g at a current density of 100 mA/g after 65 cycles [65]. Sun *et al.* reported in 2015 a green, simple, low-cost approach for the synthesis of 3D porous MnO₂/rGO/Ni composite foam via a solution chemical method with higher capacitance of 479 F/g at 1 A/g, good rate capability of 313 F/g at 10 A/g and the capacitance retention of 83.5% of its initial value after 1000 cycles [66]. Zhou *et al.* reported 2016 a method of MnO₂/GNS hybrid synthesis by one-pot electrochemical co-deposition with boosts the capacitive behaviors and cycle stability of MnO₂, in particular, the MnO₂/GNS hybrid shows a

high specific capacitance of 413 F/g at A/g [67]. Liua et al. reported a novel and efficient approach in 2017 to fabricate reduced graphene oxide (RGO)/MnO_x@carbon hollow nanospheres (HCNs) nanohybrids as a supercapacitor electrode exhibits a high specific capacitance (355 and 270 F/g in a three-electrode and two-electrode system at 1.0 A/g, respectively) in 6 M KOH electrolyte. Besides, the electrode shows a high rate charge-discharge capability (20 A/g), and good electrochemical stability (88% capacitance retention after 5000 cycles at 0.5 A/g) [68]. Bokhari et al. reported a hydrothermal pathway to synthesized hybrid electrode rGO–CNC–MnO₂ exhibited an excellent specific capacitance of 397.7 F/g at the current density of 0.2 A/g [69]. Lin et al. reported a facile and one-pot synthetic route for constructed of well-organized epsilon-MnO₂ hollow spheres/reduced graphene oxide (MnO₂HS/RGO) composites exhibited a specific capacitance of 471 F/g at 0.8 A/g and high capacitance of 272 F/g at 3 A/g (92% retention) even after 1000 cycles. Ghasemi. S et.al. reported a facile sonochemical method to MnO₂/GO exhibits high specific capacitance (Cs) of 375 F/g at the current density of 1 A/g and good cycle stability (93% capacitance retention after 500 cycles at a scan rate of 200 mV/s) [70]. According to Samdani et al. rGO-MnO₂ composite synthesized from direct redox process of between MnCl₂ and KMnO₄ on reduced graphene oxide (rGO) shows a high specific capacitance of 366 F/g at a scan rate of 10 mV/s [71]. Yibin et al reported in 2016 that the manganese dioxide/reduced graphene oxide (MnO₂/RGO) double-shelled hollow microsphere with low charge transfer resistance of 0.3006 ohm and total electrochemical impedance of 2.37 ohm caused a high specific capacitance of 450 F/g at 0.2 A/g. The capacitance retention of 81.7% after 1000 cycles indicated good cycling capability at 5 A/g [49], Sadak et al. reported in 2019 reported a simple and cost-effective green method to produce free-standing, flexible, and highly conductive electrochemically exfoliated graphene paper (GrP) deposited nanoflower like manganese dioxide (MnO₂) electrochemically on GrP with different number of MnO₂ cycles 10 cycles of electrodeposition and exhibited an excellent capacitive performance with a high specific capacitance of 385.2 F/g at 1 mV/s in 0.1 M Na₂SO₄ electrolyte and outstanding capacitance retention after 5000 consecutive cycles [72], demonstrating the as-prepared hollow crumple (--)@rGO-MnO₂ composite has superior supercapacitive properties and is a potential electrode material for supercapacitors.

5.7 References

- [1] Hummers, W. S., and Offeman, R. E., “Preparation of Graphitic Oxide”, *J. Am. Chem. Soc.*, vol. 80(6), pp. 1339, 1958.
- [2] Dreyer, D. R., Park, S., Bielawski, W., and Ruoff, R. S., “The chemistry of graphene oxide”, *Chem. Soc. Rev.*, vol. 39, pp. 228–240 2010.
- [3] Li, B., Cao, H., Shao, J., Qu, M., and Warner, J. H., “Superparamagnetic Fe₃O₄ nanocrystals@graphene composites for energy storage devices”, *J. Mater. Chem.*, vol. 21(13), pp. 5069–5075, 2011.
- [4] Marcano, D.C., Kosynkin, D.V., Berlin, J.M., Sinitskii, A., Sun, Z., Slesarev, A., Alemany, L.B., Lu, W., and Tour, J.M., “Improved synthesis of graphene oxide”, *ACS Nano*, vol. 4(8), pp. 4806–4814, 2010.
- [5] Dimiev, A. M., and Tour, J. M., “Mechanism of graphene oxide formation”, *ACS Nano*, vol. 8(3), pp. 3060–3068, 2014.
- [6] Kang, J.H., Kim, T., Choi, J., Park, J., Kim, Y.S., Chang, M.S., Jung, H., Park, K.T., Yang, S.J., and Park, C.R., “Hidden second oxidation step of hummers method”, *Chem. Mater.*, vol. 28(3), pp. 756–764, 2016.
- [7] Dimiev, A. M., Alemany, L. B., and Tour, J. M., “Graphene oxide. origin of acidity, its instability in water, and a new dynamic structural model”, *ACS Nano*, vol. 7(1), pp. 576–588, 2013.
- [8] Lee, T. E., W, J., Hall, A. S., Kim J. -D., and Mallouk, “A Facile and Template-Free Hydrothermal Synthesis of Mn₃O₄ nanorods on graphene sheets for supercapacitor electrodes with long cycle stability”, pp. 19445, 2012.
- [9] Choi, J.Y., Lee, Y.K., Yoon, S.M., Lee, H.C., Kim, B.K., Kim, J.M., Kim, K.M., and Lee, J.H., “A chemical route to large-scale preparation of spherical and monodisperse Ni powders”, *J. Am. Ceram. Soc.*, vol. 88(11), pp. 3020–3023, 2005.
- [10] Wu, X., Xing, W., Zhang, L., Zhuo, S., Zhou, J., Wang, G., and Qiao, S., “Nickel nanoparticles prepared by hydrazine hydrate reduction and their application in supercapacitor”, *Powder Technol.*, vol. 224, pp. 162–167, 2012.
- [11] Tzitzios, V., Basina, G., Gjoka, M., Alexandrakis, V., Georgakilas, V., Niarchos, D., Boukos, N., and Petridis, D., “Chemical synthesis and characterization of hcp Ni nanoparticles”, *Nanotechnology*, vol. 17(15), pp. 3750–3755, 2006.

- [12] Xie ,Y. and Ji, J., “Synthesis and capacitance performance of MnO₂/RGO double-shelled hollow microsphere”, *J. Mater. Res.*, vol. 31(10) , pp. 1423–1432, 2016.
- [13] Wu, S., Chen, W., and Yan, L., “Fabrication of a 3D MnO₂/graphene hydrogel for high-performance asymmetric supercapacitor”, *J. Mater. Chem. A*, vol. 2(8), pp. 2765–2772, 2014.
- [14] Lodhia, J., Mandarano, G., Ferris, N. J., Eu, P., and Cowell, S. F., “Development and use of iron oxide nanoparticles (part 1): synthesis of iron oxide nanoparticles for MRI”, *Biomed. Imaging Interv. J.*, vol. 6(2), 2010.
- [15] Hariani, P. L., Faizal, M., Ridwan, R., Marsi, M., and Setiabudidaya, D., “Synthesis and properties of Fe₃O₄ nanoparticles by co-precipitation method to removal procion Dye”, *Int. J. Environ. Sci. Dev.*, vol. 4(3) , pp. 336–340, 2013.
- [16] Wei, Y., Han, B., Hu, X., Lin, Y., Wang, X., and Deng, X., “Synthesis of Fe₃O₄ nanoparticles and their magnetic properties”, *Procedia Eng.*, vol. 27(2011), pp. 632–637, 2012.
- [17] Ghasemi, S., and Ahmadi, F., “Effect of surfactant on the electrochemical performance of graphene / iron oxide electrode for supercapacitor”, *J. Power Sources*, vol. 289, pp. 129–137, 2015.
- [18] Saragi, T., Depi, B. L., Butarbutar, S., Permana, B., and Risdiana, “The impact of synthesis temperature on magnetite nanoparticles size synthesized by co-precipitation method”, *J. Phys. Conf. Ser.*, vol. 1013(1), 2018.
- [19] Trusovas, R., Račiukaitis, G., Niaura, G. Barkauskas, J., Valušis, G., and Pauliukaite, V., “Recent advances in laser utilization in the chemical modification of graphene oxide and its applications”, *Adv. Opt. Mater.*, vol. 4(1), pp. 37–65, 2016.
- [20] Shanmugam M., and Jayavel,V, “Synthesize of graphene-tin oxide nanocomposite and its photocatalytic properties for the degradation of organic pollutants under visible light”, *J. Nanosci. Nanotechnol.*, vol. 15(9), pp. 7195–7201, 2015.
- [21] Ghodbane, O., Pascal, J. L., and Favier, F., “Microstructural effects on charge-storage properties in MnO₂-based electrochemical supercapacitors”, *ACS Appl. Mater. Interfaces*, vol. 1(5), pp. 1130–1139, 2009.

- [22] Jiang, H., Dai, Y., Hu, Y., Chen, W., and Li, C., “Nanostructured ternary nanocomposite of rGO/CNTs/MnO₂ for high-rate supercapacitors”, *ACS Sustain. Chem. Eng.*, vol. 2(1), pp. 70–74, 2014.
- [23] Gueon, D., and Moon, J. H., “MnO₂ nanoflake-shelled carbon nanotube particles for high-performance supercapacitors”, *ACS Sustain. Chem. Eng.*, vol. 5(3), pp. 2445–2453, 2017.
- [24] Lei, Z., Shi, F., and Lu, L., “Incorporation of MnO₂-coated carbon nanotubes between graphene sheets as supercapacitor electrode”, *ACS App. Mat. and Inter.*, vol. 4, pp. 1058–1064, 2012.
- [25] Li, L., Hu, Z. A., An, N., Yang, Y. Y., Li, Z. M., and Wu, H. Y., “Facile synthesis of MnO₂/CNTs composite for supercapacitor electrodes with long cycle stability”, *J. Phys. Chem. C*, vol. 118(40), pp. 22865–22872, 2014.
- [26] Mohanraj, K., and Sivakumar, G., “Synthesis of γ -Fe₂O₃, Fe₃O₄ and copper doped Fe₃O₄ nanoparticles by sonochemical method”, *Sains Malaysiana*, vol. 46(10,) pp. 1935–1942, 2017..
- [27] Aliramaji, S., Zamanian, A., and Sohrabijam, Z., “Characterization and synthesis of magnetite nanoparticles by innovative sonochemical method”, *Procedia Mater. Sci.*, vol. 11, pp. 265–269, 2015.
- [28] Lu, L., Xu, S., An, J., and Yan, S., “Electrochemical performance of CNTs/RGO/MnO₂ composite material for supercapacitor”, *Nanomater. Nanotechnol.*, vol. 6, pp. 1–7, 2016.
- [29] Xu, C., Shi, X., Ji, A., Shi, L., Zhou, C., and Cui, Y., “Fabrication and characteristics of reduced graphene oxide produced with different green reductants”, *PLoS One*, vol. 10(12), 2015.
- [30] Kong, D., Le, L. T., Li, Y., Zunino, J. L., and Lee, W., “Temperature-dependent electrical properties of graphene inkjet-printed on flexible materials”, *Langmuir*, vol. 28(37), pp. 13467–13472, 2012.
- [31] Su, X., Wang, G., Li, W., Bai, J., and Wang, H., “A simple method for preparing graphene nano-sheets at low temperature”, *Adv. Powder Technol.*, vol. 24(1), pp. 317–323, 2013.
- [32] Kang, D., Zhang, F., and Zhang, H., “Fabrication of stable aqueous dispersions of graphene using gellan gum as a reducing and stabilizing agent and its nanohybrids”, *Mater. Chem. Phys.*, vol. 149, pp. 129–139, 2015.

- [33] Si, Y., and Samulski, E. T., “Synthesis of water soluble graphene”, *Nano Lett.*, vol. 8(6), pp. 1679–1682, 2008.
- [34] Sadhukhan, S., *et al.*, “Studies on synthesis of reduced graphene oxide (RGO) via green route and its electrical property”, *Mater. Res. Bull.*, vol. 79, pp. 41–51, 2016.
- [35] Abdolhosseinzadeh, S., Asgharzadeh, H., and Kim, H. S., “Fast and fully-scalable synthesis of reduced graphene oxide”, *Sci. Rep.*, vol. 5, pp. 1–7, 2015.
- [36] Yang, X., Makita, Y., Liu, Z. H., Sakane, K., and Ooi, K., “Structural characterization of self-assembled MnO₂ nanosheets from birnessite manganese oxide single crystals”, *Chem. Mater.*, vol. 16(26), pp. 5581–5588, 2004.
- [37] Jaganyi, D., Altaf, M., and Wekesa, I., “Synthesis and characterization of whisker-shaped MnO₂ nanostructure at room temperature”, *Appl. Nanosci.*, vol. 3(4), pp. 329–333, 2013.
- [38] Mohd Zaid, N. A., and Idris, N. H., “Enhanced capacitance of hybrid layered graphene/nickel nanocomposite for supercapacitors”, *Sci. Rep.*, vol. 6, pp. 1–8, 2016.
- [39] Deng, S., and Berry, V., “Wrinkled, rippled and crumpled graphene: An overview of formation mechanism, electronic properties, and applications”, *Mater. Today*, vol. 19(4), pp. 197–212, 2016.
- [40] Zhang, L., Shi, D., Liu, T., Jaroniec, M., and Yu, J., “Nickel-based materials for supercapacitors”, *Materials Today*, vol. 25, pp. 35–65, 2019.
- [41] Yao, J., Pan, Q., Yao, L. S., Duan, and Liu, J., “Mesoporous MnO₂ nanosphere/graphene sheets as electrodes for supercapacitor synthesized by a simple and inexpensive reflux reaction”, *Electrochim. Acta*, vol. 238, pp. 30–35, 2017.
- [42] Shao, Q., Tang, J., Lin, Y., Zhang, F., Yuan, J., Zhang, H., Shinya, N., and Qin, L.C., “Synthesis and characterization of graphene hollow spheres for application in supercapacitors”, *J. Mater. Chem. A*, vol. 1(48), pp. 15423–15428, 2013.
- [43] Akmal, N., Zaid, M., and Idris, N. H., “Enhanced Capacitance of hybrid layered graphene / nickel nanocomposite for supercapacitors”, *Nat. Publ. Gr.*, pp. 1–8, 2016.
- [44] Gupta, R. K., Candler, J., Palchoudhury, S., Ramasamy, K., and Gupta, B. K., “Flexible and high performance supercapacitors based on NiCo₂O₄ for wide temperature range applications”, *Sci. Rep.*, vol. 5, pp. 1–11, 2015.

- [45] Zhang, J., Jiang, J., and Zhao, X. S., “Synthesis and capacitive properties of manganese oxide nanosheets dispersed on functionalized graphene sheets”, *J. Phys. Chem. C*, vol. 115(14), pp. 6448–6454, 2011.
- [46] Liu, Y., Yan, D., Zhuo, R., Li, S., Wu, Z., Wang, J., Ren, P., Yan, P., and Geng, Z., “Design, hydrothermal synthesis and electrochemical properties of porous birnessite-type manganese dioxide nanosheets on graphene as a hybrid material for supercapacitors”, *J. Power Sources*, vol. 242, pp. 78–85, 2013.
- [47] Chen, Z., Li, J., Chen, Y., Zhang, Y., Xu, G., Yang, J., and Feng, Y., “Microwave-hydrothermal preparation of a graphene/hierarchy structure MnO₂ composite for a supercapacitor”, *Particuology*, vol. 15, pp. 27–33, 2014.
- [48] Mohd Zaid, N. A., and Idris, N. H., “Enhanced capacitance of hybrid layered graphene/nickel nanocomposite for supercapacitors”, *Sci. Rep.*, vol. 6, pp. 1–8, 2016.
- [49] Xie, Y., and Ji, J., “Synthesis and capacitance performance of MnO₂/RGO double-shelled hollow microsphere”, *J. Mater. Res.*, vol. 31(10), pp. 1423–1432, 2016.
- [50] Qian, Y., Lu, S., and Gao, F., “Preparation of MnO₂/graphene composite as electrode material for supercapacitors”, *J. Mater. Sci.*, vol. 46(10), pp. 3517–3522, 2011.
- [51] Lei, Z., Chen, Z., and Zhao, X. S., “Growth of polyaniline on hollow carbon spheres for enhancing electrocapitance”, *J. Phys. Chem. C*, vol. 114(46), pp. 19867–19874, 2010.
- [52] Devaraj, S., and Munichandraiah, N., “Electrochemical supercapacitor studies of nanostructured α -MnO₂ synthesized by microemulsion method and the effect of annealing”, *J. Electrochem. Soc.*, vol. 154(2), 2007.
- [53] Yan, J., Fan, Z., Wei, T., Qian, W., Zhang, M., and Wei, F., “Fast and reversible surface redox reaction of graphene-MnO₂ composites as supercapacitor electrodes”, *Carbon.*, vol. 48(13), pp. 3825–3833, 2010.
- [54] Bokhari, S.W., Hao, Y., Siddique, A.H., Ma, Y., Imtiaz, M., Butt, R., Hui, P., Li, Y., and Zhu, S., “Assembly of hybrid electrode rGO–CNC–MnO₂ for a high performance supercapacitor”, *Results Mater.*, vol. 1, pp. 100007, 2019.
- [55] Xu, M., Kong, L., Zhou, W., and Li, H., “Hydrothermal synthesis and pseudocapitance properties of α -MnO₂ hollow spheres and hollow urchins”, *J. Phys. Chem. C*, vol. 111,(51), pp. 19141–19147, 2007.

- [56] Umeshbabu, E., Justin, P., and Rao, G. R., “Tuning the surface morphology and pseudocapacitance of MnO₂ by a facile green method employing organic reducing sugars”, *ACS Appl. Energy Mater.*, vol. 1(8), pp. 3654–3664, 2018.
- [57] Hasan, M.R., Lai, C.W., Hamid, B. A. S., and Basirun, W. J. “Effect of Ce doping on rGO-TiO₂ nanocomposite for high photoelectrocatalytic behavior”, *Int. J. Photoenergy*, vol. 2014, 2014.
- [58] Li, B., Cao, H., Shao, J., Qu, M., and Warner, J. H., “Superparamagnetic Fe₃O₄ nanocrystals@graphene composites for energy storage devices”, *J. Mater. Chem.*, vol. 21(3), pp. 5069–5075, 2011.
- [59] Yuan, L., Lu, X.H., Xiao, X., Zhai, T., Dai, J., Zhang, F., Hu, B., Wang, X., Gong, L., Chen, J., “Flexible solid-state supercapacitors based on carbon nanoparticles/MnO₂ nanorods hybrid structure”, *ACS Nano*, vol. 6(1), pp. 656–661, 2012.
- [60] Bokhari, S.W., Hao, Y., Siddique, A.H., Ma, Y., Imtiaz, M., Butt, R., Hui, P., Li, Y., and Zhu, S, “Assembly of hybrid electrode rGO–CNC–MnO₂ for a high performance supercapacitor”, *Results Mater.*, vol. 1, pp. 100007, 2019.
- [61] Chang, C. W., and Liao, Y. C., “Accelerated Sedimentation Velocity Assessment for Nanowires Stabilized in a Non-Newtonian Fluid”, *Langmuir*, vol. 32(51), pp. 13620–13626, 2016.
- [62] Zhang, Y., Su, M., Ge, L., Ge, S., Yu, J., and Song, X., “Synthesis and characterization of graphene nanosheets attached to spiky MnO₂ nanospheres and its application in ultrasensitive immunoassay”, *Carbon.*, vol. 57, pp. 22–33, 2013.
- [63] Peng, L., Peng, X., Liu, B., Wu, C., Xie, Y., and Yu, G., “Ultrathin two-dimensional MnO₂/graphene hybrid nanostructures for high-performance, flexible planar supercapacitors”, *Nano Lett.*, vol. 13(5), pp. 2151–2157, 2013.
- [64] Ye, K. H., Liu, Z. Q., Xu, C. W., Li, N., Chen, Y. B., and Su, Y. Z., “MnO₂/reduced graphene oxide composite as high-performance electrode for flexible supercapacitors”, *Inorg. Chem. Commun.*, vol. 30, pp. 1–4, 2013.
- [65] Wen, K., Chen, G., Jiang, F., Zhou, X., and Yang, J., “A facile approach for preparing MnO₂-graphene composite as anode material for lithium-ion batteries”, *Int. J. Electrochem. Sci.*, vol. 10(5), pp. 3859–3866, 2014.

- [66] Sun Y., *et al.*, “Facile synthesis of MnO₂/rGO/Ni composite foam with excellent pseudocapacitive behavior for supercapacitors”, *J. Alloys Compd.*, vol. 649, pp. 579–584, 2015.
- [67] Zhou, H., and Zhai, H. J., “Rapid preparation of the hybrid of MnO₂ dispersed on graphene nanosheets with enhanced supercapacitive performance”, *Electrochim. Acta*, vol. 215, pp. 339–345, 2016.
- [68] Liu, M., Shi, M., Lu, W., Zhu, D., Li, L., and Gan, L., “Core–shell reduced graphene oxide/MnO_x@carbon hollow nanospheres for high performance supercapacitor electrodes”, *Chem. Eng. J.*, vol. 313, pp. 518–526, 2017.
- [69] Jiang, H., Dai, Y., Hu, Y., Chen, W., and Li, C., “Nanostructured ternary nanocomposite of rGO/CNTs/MnO₂ for high-rate supercapacitors”, *ACS Sustain. Chem. Eng.*, vol. 2(1), pp. 70–74, 2014.
- [70] Ghasemi, S., Hosseini, S. R., and Boore-talari, O., “Sonochemical assisted synthesis MnO₂/RGO nanohybrid as effective electrode material for supercapacitor”, *Ultrason. Sonochem.*, vol. 40, pp. 675–685, 2018.
- [71] Samdani, J., Samdani, K., Kim, N. H., and Lee, J. H., “A new protocol for the distribution of MnO₂ nanoparticles on rGO sheets and the resulting electrochemical performance”, *Appl. Surf. Sci.*, vol. 399, pp. 95–105, 2017.
- [72] Sadak, O., Wang, W., Guan, J., Sundramoorthy, A. K., and Gunasekaran, S., “MnO₂ nanoflowers deposited on graphene paper as electrode materials for supercapacitors”, *ACS Appl. Nano Mater.*, vol. 2(7), pp. 4386-4394, 2019.
- [73] Luo, J., Jang, H. D. and Huang, J., “Effect of sheet morphology on the scalability of graphene-based ultracapacitors”, *ACS Nano*, vol. 7, pp. 1464–1471, 2013.

Chapter-6

Conclusions

6 Conclusions

The nanocomposite, rGO-MnO₂, core-shell Ni@rGO-MnO₂, hollow porous (--)@rGO-MnO₂ from Ni@rGO-MnO₂, core-shell Fe₃O₄@rGO-MnO₂ and hollow crumple (--)@rGO-MnO₂ from Fe₃O₄@rGO-MnO₂ have been successfully synthesized by a simple chemical route.

The crystalline structural analysis of the materials by XRD shows that the birnessite type lattice structure of both MnO₂, hexagonal structure of graphene and cubic Fe₃O₄. The calculation of particle size from the high-intensity XRD peak using the Scherrer equation and from the FESEM image of the materials showed that all the prepared materials were formed in nano-dimensions. The nanocomposites, manganese oxides and graphene showed the presence of relevant functional groups and Mn-O bond vibrations in their corresponding FTIR spectrum.

The cyclic voltammograms of all materials are close to the symmetric rectangular shape and exhibit mirror-image characteristics. The results demonstrate the excellent reversibility and ideal capacitive behavior. All these materials showed reversible charge-discharge processes in GCD studies with a curvature on their discharging counterpart of the prepared materials for porous and hollow crumpled materials. Inclusion of Ni and Fe₃O₄ NPs in the core of rGO-MnO₂ influence the electrochemical properties of rGO-MnO₂, as well as better electrochemical performance, is observed by the exclusion of Ni and Fe₃O₄ NPs from the core of rGO-MnO₂. It may be noted that hollow porous (--)@rGO-MnO₂ synthesized from Ni@rGO-MnO₂ shows specific capacitance 688 F/g at 0.1 A/g current density and capacitance retention 97.2% at 5 A/g current density after 1000 cycles indicating utmost cycle stability and with superior energy density 77 Wh/kg and power density 63 W/kg than Ni@rGO-MnO₂ and rGO-MnO₂.

It is also noticeable that porous and hollow crumpled (Fe_3O_4 @rGO)- MnO_2 synthesized from Fe_3O_4 @rGO- MnO_2 shows specific capacitance 1086 F/g at 0.1 A/g current density and capacitance retention 96.45% at 5 A/g current density after 1000 cycles indicating utmost cycle stability and with superior energy density 124 Wh/kg and power density 55 W/kg than Fe_3O_4 @rGO- MnO_2 and rGO- MnO_2 electrodes fabricated from this materials exhibit such high electrochemical performance probably due to the highly conductive network, porous and hollow morphologies and synergistic link between manganese oxides and graphene. This better electrochemical performance indicates that these nanomaterials can be used as a very promising candidate as electrode materials for cost-effective high-performance electrochemical capacitors in supercapacitor devices, although further work should be carried out to upscale such compound without compromising the performance.